

Investigations of Liquid-Solid Phase Transition of Solvated Ions in Supersaturated Solutions

Dissertation for Doctor Degree of Nature Science (Dr. rer. nat.)

Fachbereich Biologie, Chemie, Pharmazie der Freie Universität Berlin

Yan Zhang

(from Beijing, China)



Berlin, May 2012

Germany

The following project was carried out within the research group of Prof. Dr. Eckart Rühl from September 2008 to December 2011 at the Institute of Chemistry and Biochemistry of Freie Universität Berlin.

1st Reviewer: **Prof. Dr. E. Rühl**

2nd Reviewer: **Prof. Dr. H. Baumgärtel**

Date of Defence: **27. 07. 2012**

Acknowledgement

I would like to thank sincerely all the members of the group (AG Rühl) and collaborators from other institutes, for their constant support and useful suggestions. Without any doubt, I can say that I got very kind help from everyone of you during these last few years. In particular, I thank enormously my supervisor, Mr. Prof. Dr. E. Rühl, who has supervised my promotion from the start to the end; without his help and guidance, this thesis would simply have not been possible. I am very grateful for all your support, quixotic effort to help solving all the problems I faced, and concern for the final success of my research. I want to thank as well my colleague Mr. Dr. B. Wassermann with whom I have shared a lot of hard work in the lab and spent a very good working time. Our cooperation and discussions made the whole tough scientific work much more enjoyable. I also want to thank him for contributing in part of the theoretical simulations of this work.

Many thanks also to Mr. Prof. Dr. A. Erko from BESSY II (Helmholtz Center Berlin, Germany) who provided generous technical support for using synchrotron radiation of hard X-ray in BESSY.

I also would like to thank people in Physikalisch-Technische Bundesanstalt (PTB), especially Mr. Dr. M. Müller and Mr. Dr. B. Beckhoff, for offering invaluable assistance in our experiments.

I also give my special thanks to my husband, Mr. Dr. J. Carrasco. He agreed to contribute to some of the theoretical simulations for this work in his private time. Moreover, we discussed much of the science of this thesis in “family meetings”.

Last but not least, I want to sincerely thank my parents in Beijing, China. Thanks for loving me since I was a small kid, and supporting all of my decisions

along these years, including giving up my job in Beijing and coming to Germany. I am very proud of having such lovely parents.

Contents

Chapter 1 Introduction

1.1 Homogeneous Nucleation in Single Levitated Droplets	2
1.2 Charge Effects on Homogeneous Nucleation	7
1.3 Organization of This Thesis	8

Chapter 2 Theoretical Background

2.1 Optical Levitation	10
2.2 Thermodynamic Equilibrium of Aqueous Solution Droplet	12
2.3 Homogeneous Nucleation Theory	16
2.4 Theory of Supersaturated Electrolyte Solutions	20
2.5 Discrete Dipole Approximation	23
2.6 X-ray Absorption	26
2.7 Density Functional Theory	29
2.7.1 Basics of Quantum Chemistry	29
2.7.2 The Kohn-Sham Theory	31
2.8 Core-Level Electron Energy Loss Spectra Calculations	33
2.8.1 CASTEP	33
2.8.2 CPMD	33

Chapter 3 Experimental Details

3.1 Optical Levitation of Single Droplet	35
3.2 XANES Spectroscopy on Single Levitated Droplets	37
3.2.1 Experimental Details of Optical Levitation in Combination with Hard X-rays	37
3.2.2 Preliminary Adjustment	40
3.3 Experimental Setup for XANES Studies using Soft X-Rays	42
3.4 Electrodynamical Levitation Trap	44
3.5 Determination of the Microparticle Charge	46

3.6 Experimental Procedure of Efflorescence Determination	48
3.7 Combination of Optical Levitation and Electrodynamic Levitation	49
3.8 Aqueous Salt Solutions and Solid Samples	50
Chapter 4 Results and Discussion	
4.1 Phase Diagrams of Electrolyte Solutions	52
4.1.1 Phase Diagram of NaBr	52
4.1.2 Phase Diagrams of CaBr ₂ and ZnBr ₂	58
4.2 XANES Studies of Cluster Formation in Homogeneous Nucleation of Single Levitated Microdroplets	61
4.2.1 XANES Studies of Aqueous NaBr Solutions and Solid NaBr	63
4.2.2 Theoretical Simulation of the Br K-edge in NaBr Nanoclusters	67
4.2.3 XANES Studies of CaBr ₂ and its Dilute Solution and Solids	72
4.2.4 Simulations of diluted and supersaturated CaBr ₂ solutions	75
4.2.5 XANES Studies of ZnBr ₂ Droplets and its Dilute Solution and the Solid	80
4.3 Near-Edge Structure of Supersaturated KBr Droplets	82
4.4 Charge Effects on the Nucleation Process of Single Levitated Droplets	86
4.4.1 Efflorescence Measurements of Single Neutral / Charged Droplets	86
4.4.2 Charge Effects on the Efflorescence of Single Levitated Droplets	90
4.5 Simulations of Scattering Patterns in Crystallizing Droplets	99
Chapter 5 Conclusions and Outlook	
5.1 Conclusions	107
5.2 Outlook	110
Summary (English)	111
Zusammenfassung (Deutsch)	113
References	115

Chapter 1

Introduction

Nucleation is one of the most important processes in nature and people's daily life [ZHANG 2009]. One of the most common examples is the rain or the snow which are formed via the condensation or freezing of water [LIU 2004]. Many hard tissues, such as bones and teeth, consist of well organized and assembled aggregates of biomineral nanocrystallites [JIANG 2004]. Many nucleation theories, which intend to interpret the mechanism of nucleation, are proposed and supported by different arguments [KASHCHIEV 2000, LAAKSONEN 1995, RUCKENSTEIN 2005]. However, nucleation process still remains poorly understood.

This thesis is devoted to the study of homogeneous nucleation of supersaturated solutions and related processes. One of the main goals of this study is to shed light on the description of homogeneous nucleation mechanisms involving the formation and growth of solute clusters in solution, as a result of local concentration fluctuation in highly supersaturated microdroplets. For this purpose, we have used two experimental techniques: optical levitation and X-ray absorption spectroscopy (XAS). By combining these we have been able to monitor the entire nucleation process, according to changes in local electronic structure of selected ionic species. An additional important task of this work is to study charge effects on the nucleation process. In order to do this, we have compared the humidity-dependence of crystallization time of both neutral and charged droplets.

Trying to understand the nucleation process in both neutral and charged droplets have been intensively investigated from chemical, physical, and theoretical points of view. In this chapter, we are going to overview some important earlier and preliminary work related to the field.

1.1 Homogeneous Nucleation in Single Levitated Droplets

Crystallization from liquid to solid is an important processes occurring in nature, as well as in chemical, pharmaceutical, and food industries. The reason of this process being so attractive is that a single step of crystallization accomplishes both phase separation and purification which is crucial for almost all the products related to fine chemicals.

In crystallization from solution, nucleation which is defined as the initial stage of the process leading to the formation of a new phase, which can be either solid or liquid, from a metastable parent phase, i.e. a supersaturated vapor or a solution, plays a decisive role in determining the crystal structure, size distribution, and their physical and/or chemical properties [DEMO 1993]. For example, in industry more than 90% of pharmaceutical products have to be produced in a certain crystal shape via crystallization in order to assure their bioavailability and stability [ERDEMIR 2009]. Therefore, an improved understanding of the fundamental nucleation mechanisms is a key factor to control the crystallization process [ERDEMIR 2009]. There have been different methods described in the literature, which serve for controlling the nucleation process [CHAYEN 2001, CHAYEN 2006, DIAO 2011]. For example, polymer microgels have been used, which are able to tune their microstructure in order to vary systematically the degree of nanaoscopic confinement in solution [DIAO 2011].

From the fundamental point of view, nucleation processes can be classified into homogeneous nucleation and heterogeneous nucleation, depending on whether impurities, i.e. crystallization nuclei, are present in solution as a preferential site of nucleation. In this work, we only consider homogeneous nucleation in which nucleation proceeds via a stochastic event in a pure liquid or in a homogeneous solution, where no foreign substances are present. Heterogeneous nucleation, which occurs either at suitable impurities or at surfaces of the reaction container, is not included.

Classical nucleation theory (CNT) (introduced in Section 2.3) is the most simple theory for describing the nucleation process where it is postulated that solute clusters, which is the requirement for initializing homogeneous nucleation, can only be formed in supersaturated solution, as a result of local concentration fluctuations [VOLMER 1939]. Supporting indirect evidence for the existence of solute clusters has been

reported decades ago. One of the first relevant publications in this field has been published by Khamskii in 1969 [KHAMSKII 1969]. They observed a continuous increase of light transmission through supersaturated solutions before the onset of crystallization. It was suggested that this finding is attributed to the aggregation of solvated ions. In the same year, Mullin and Leci [MULLIN 1969] reported that isothermal vertical columns of supersaturated aqueous citric acid solutions have a higher concentration near the bottom than near the top. They suggested that these concentration gradients, which do not exist in saturated and undersaturated solutions, are due to the formation of clusters which are moved from the top of the columns to the bottom by the gravitational force. Later, similar results were published for other solutes, such as sucrose [ALLEN 1972], citric acid, sodium nitrate [LARSON 1986], and glycine [LO 1989].

However, the mechanism of homogeneous nucleation on a microscopic level has still facets to be explored. From the classical point of view, critical clusters are eventually formed by attachment of single moieties, where collisions between clusters are neglected [ZETTLEMOYER 1969]. Nevertheless, with the development of modern experimental techniques, increasing evidence during the last decades showed that the nucleation process is more complicated than the classically thought and the interactions between clusters play an important role in the nucleation process. For example, results from Raman spectroscopy showed the presence of clusters in aqueous NaNO_3 solution [RUSLI 1989] and it was suggested that in saturated solution solute clusters are further growing by coalescence. Later, cluster formation in aqueous of NaCl and $(\text{NH}_4)_2\text{SO}_4$ solutions were also observed by dynamic light scattering [GEORGALIS 2000].

All these studies suggest that microclusters are formed even in unsaturated aqueous solutions. Therefore, nowadays one of the main concerns in understanding nucleation mechanisms is related to the properties of these “prenucleation” clusters regarding formation of a new solid phase in solution. Prenucleation clusters of glycine have been observed during crystallization by a combination of NMR, as well as X-rays and neutron scattering methods [HUGHES 2007]. Moreover, recent evidence points to the existence of stable ionic prenucleation clusters in unsaturated solutions of calcium carbonate, demonstrating that clusters aggregation of an amorphous solid could

evolves into a particular polymorph depending on the pH value of the solution [GEBAUER 2008].

All these reported nucleation processes are difficult to explain based on a purely classical mechanism. It has been generally assumed that some of them involve both classical and nonclassical pathways during nucleation. This assumption is currently confirmed by the first direct observation of individual nucleation trajectories in real time, which are successfully probed by means of transmission electron microscopy in nanometer resolution [ZHENG 2009]. Both classical and nonclassical nucleation mechanisms exist simultaneously when suspending platinum nanoparticles in a wide range of size distribution. This evolves into a monodisperse suspension of single nanocrystals [HASSAN 2011]. It has also been identified that at early stages of crystal growth, nanoparticles evolve predominantly via crystallographically specific oriented attachment (OA) from which single crystals are formed upon coalescence [HUANG 2003, NIEDERBERGER 2006].

The main drawback of CNT arises from the assumption that macroscopic properties of molecules can be applied to microscopic activities. This means that CNT cannot give a precise description of surface tension and saturated vapor pressure of clusters consisting of only several tens of molecules. Therefore, in addition to experimental evidence for the observation of solute clusters, a series of newly developed theoretical simulations regarding the process of crystal growth have also been reported [MATSUMOTO 2002]. Specifically, Ginde and Myerson performed calculations on the average cluster size in binary supersaturated solutions and they suggested that this property ranges from 2 to 100 molecules. Moreover, it was shown that the degree of association was determined by solution temperature, time, degree of supersaturation, as well as the thermal history of the solution [GINDE 1992]. Demo and Kožíšek proposed an improved kinetic model for homogeneous nucleation under isothermal conditions [DEMO 1993], which is capable to determine the distribution function of newly formed clusters together with other important properties of the solution, such as the nucleation rate, integrated flux, etc. Based on this, Maksimov predicted that there are two (weak and strong) nucleation regimes. These are determined by a metastability parameter M of the considered system which is able to modify significantly the nucleation barrier topography [MAKSIMOV 2002].

Lately, the growing patterns of urea clusters in different solvents (water, methanol) were simulated at the micrometer scale, and it was demonstrated that urea clusters growing in water have needle-like morphology characteristics while in methanol solution clusters forming polar morphology [PIANA 2005]. Currently, a microscopic formation mechanism of nanoscale NaCl crystals was simulated by molecular dynamics and it was demonstrated that cluster aggregation and coalescence are observed continuously in pre- and post-nucleation stages [HASSAN 2011]. This work also suggested that the hydration process of clusters might play an important role in stabilizing small clusters and, therefore, hydration of the incipient nucleus is an important factor for crystallization process in aqueous solution. It has been found out that the association of ions in solution occurs when the hydration shell around the ion is lost which is promoted by the tendency of preserving the hydrogen-bonded network of the solvent [HAWLICKA 2003]. Therefore, clustering and nucleation of ions in aqueous media is the result of the competition between hydration of ions and their association. The structure of the aqueous solvent is affected by the composition of solutes [HAWLICKA 2003, MARCUS 2009].

Although in last decades progress has been made in modeling and controlling the mechanisms of homogeneous nucleation, microscopic insight of each stage of nucleation still remains not fully known from both experimental and theoretical viewpoints. The difficulties of experimentally tracking the complete nucleation process and giving an accurate description arise mostly from the small size and the transient occurrence of the critical nucleus. It has been reported [SCHUTH 2001] that normally these nuclei contain about 100 to 1000 atoms which is difficult to access for most of the modern experimental techniques if they occur in high dilution. Theoretical simulation of nucleation from supersaturated solution to a solid is equally challenging. This is because the nucleation process is usually studied in thermodynamic equilibrium conditions, which means that long simulation times and multiple trajectories are required. Additionally, modeling of electrolyte solutions involves a complex medium with at least three kinds of species (water, cations, and anions), resulting in a high computational effort and costs, even for current state-of-the-art supercomputers.

The goal of this work is to derive a complete picture of homogeneous nucleation in supersaturated solutions through a combination of experimental measurements and

theoretical simulation. Single levitated droplets are studied by means of optical levitation, where the solute is contained with a high degree of supersaturation. This is a metastable state, where solute nuclei are formed as the preferential sites of further nucleation. Under thermodynamic conditions, microscopic clusters might evolve through single atom attachment or/and cluster aggregation. We can then follow this dynamic crystallization process by probing the electronic structure of selected atoms in solution providing valuable information of the nucleation process.

X-ray absorption near edge structure (XANES) is a sensitive probe to follow changes in local electronic structure at short range around the absorbing atom. We combine optical levitation with the use of synchrotron radiation to take XANES spectra of single levitated droplets of different binary solvent-electrolyte systems to study self-association of ions and clustering in supersaturated solutions. Such increase of solute concentration is expected to promote aggregation of clusters. Repeating measurements were carried out at different solute concentrations which are controlled by varying the relative humidity in the environment of the levitated droplets. Distinct changes in energy position of absorption-edges are observed. This carries important information regarding the evolution process of subcritical clusters as a function of solute concentration. Model calculations on different model structures are performed. These allow us to derive insights into the electronic structure of solute clusters giving rise to distinct spectral features in the near-edge regime. Using this information we explore systematic trends of changes in near-edge structure as a function of solute concentration.

To this end, we have studied a series of aqueous solutions containing the following salts: calcium bromide (CaBr_2), zinc bromide (ZnBr_2), and sodium bromide (NaBr). We have generated single droplet by a piezo injector. The droplets are levitated by an intense cw-laser beam. XANES spectra are taken at the absorption energies of the Br K-edge and at the Zn K-edge at different humidity condition, i.e., solute concentration. Moreover, in order to derive a complete picture of phase transitions from liquid to solid, XANES spectra of dilute solutions and pure solid crystals of each sample material were also measured for a comparison with their corresponding supersaturated droplets.

1.2 Charge Effects on Homogeneous Nucleation

Droplets possessing a net charge have received continuous attention in recent years [HADDRELL 2004, BOGAN 2005]. Both experimental and theoretical evidence has shown that the net charge on a droplet could result in significant variations in the physical [WEON 2008] and chemical properties [BAKHOUM 2005] of the droplet. Additionally, it was also reported [TABAZADEH 2002] that surface charges could affect the nucleation process in supersaturated solutions which is an important phenomenon for atmospherical, environmental, and biological studies [ARNOLD 1980, MIYATA 2005].

Therefore, it is not surprising that numerous studies have been carried out in order to understand the effects of droplet net charges so that an improved description of cluster formation and crystal growth in these solutions can be given [ZHANG 2010]. Most of this evidence points to the fact that the presence of net charges promotes the formation of critical clusters in supersaturated solution, i.e., promoting the nucleation process of the droplet [GAMERO-CASTAÑO 2002]. Bakhoun *et al.* have reported electrodynamic levitation trap (EDLT) studies on the promotion of NaCl precipitation as a function of the net charge on the droplet surface [BAKHOUM 2005]. This phenomenon is called *ion-induced nucleation* which was first quantitatively investigated by Wilson *et al.* [WILSON 1899]. Bogan *et al.* [BOGAN 2005] also provided evidence for the occurrence of co-crystallization of α -cyano-4-hydroxycinnamic acid with one or more peptides which was achieved by controlling the magnitude of the net charge in a trapped droplet. In fact, ion-induced nucleation can be considered as a special kind of heterogeneous nucleation, in which bare ions (or electrical charges) act as condensation embryos and the strong ion-dipole interaction between these and the vapor phase molecules reduces the nucleation barrier, i.e., the supersaturation requirement, leading to the promotion of nucleation [GAMERO-CASTAÑO 2002].

A series studies also suggested that in EDLT, solute nucleation in supersaturated solution can also be affected by external electric [TANG 2005] and magnetic fields [MICHELETTO 2005, SABAN 2005]. The influence of an electric field on nucleation kinetics was first investigated by Shubnikov *et al.* and Kozlovskii *et al.* [SHUBNIKOV 1961, KOZLOVSKII 1962], followed by several other works supporting the stimulating

effect of external electric fields on the nucleation rates of supersaturated solutions [PILLAI 1981, SABAN 2002].

Although substantial research has been devoted to charged droplets in the last century, condensed phase chemistry in such droplets is still not well characterized [MYLAND 2002, BOGAN2005, BAKHOUM 2005], and sometimes even conflicting results were derived from different works. For example, Krämer et al. [KRÄMER 1999] measured the nucleation rate of water droplets carrying different electrical charges in EDLT where no promoting effect of electrical charges on the nucleation rate of droplets was observed. Numerous follow-up studies regarding characterization of physical properties of levitated droplets were carried out which were based on this conclusion. One of these is for example work by Hamza et al. [HAMZA 2004], who studied the temperature-dependence of the efflorescence humidity of supersaturated KCl solution droplets by measuring their crystallization time. In this work, the promoting effect of electrical charges on the nucleation process, which might result in different efflorescence humidity, was not considered.

More scientific work is required in order to clarify the nucleation mechanism of charged droplet solutions. In this thesis we have tackled this issue by studying the charge effects on the nucleation process of supersaturated solution by comparing the crystallization time of neutral and charged microdroplets which are levitated in an optical levitation trap (OLT) and EDLT, respectively. Solutions of potassium chloride (KCl) and sodium chloride (NaCl) were used. Systematic studies of the humidity dependence of the crystallization time were performed using aqueous solution droplets carrying different electric charges (including neutral ones) in order to derive reliable results on the influence of electrical charges to the homogeneous nucleation process.

1.3 Organization of This Thesis

This thesis consists of three parts which are the theoretical background (Chapter 2), a detailed description of the experimental setups (Chapter 3), and the results and their discussion (Chapter 4). The theories which have been applied for the analysis of the experimental data and theoretical simulations are introduced in the Section covering

the theoretical background. Readers who are interested in, for example, the basics of XANES spectroscopy find a brief summary on this issue in this chapter. Details of the experimental setup and operating parameters are given in Chapter 3. In Chapter 4, we present the most important experimental results, the discussion, including results from model simulations. XANES spectra taken from optically levitated droplets are one of the most important results of this work. Phase diagrams of the sample solutions used in this work are constructed in order to assign the spectroscopic results properly. Charge effects on homogeneous nucleation occurring in supersaturated solutions are discussed subsequently. Finally, a series of simulations of elastic scattering patterns is carried out in order to get information of cluster formation in supersaturated solution droplets.

Chapter 2

Theoretical Background

2.1 Optical Levitation

Optical levitation in which a single droplet of an aqueous solution is levitated by the force of a focused laser beam is one of the most important techniques which are applied in this work. In order to understand the physical reasons behind this experimental approach, we are going to introduce related theories involving net forces exerting on levitated droplets and describe in detail how the stable levitation is achieved by the applying forces on a small object in this Section.

According to the well known Einstein equation ($E = mc^2$) and Planck equation ($E = h\nu$), the momentum of the photon P_{photon} (kg m s⁻¹) can be described as [MUND 2003]:

$$P_{photon} = mc = \frac{E}{c} = \frac{h\nu}{c} = \frac{h}{\lambda} \quad (2.1)$$

where m is the equivalent mass of photon (kg), c is the speed of light (m/s), E is the photon energy (J), ν is the frequency of the radiation (s⁻¹), λ is the wavelength of light in vacuum, and h is the Planck constant.

Therefore, it can be realized from Eq. (2.1) that an intense vertically oriented laser beam may levitate an object of certain mass by the photon momentum, in the case that the gravity of the object is equal to the upward scattering force of the laser beam. However, stable levitation is hardly accomplished with only the compensating force of gravity in vertical direction because in this case the levitated particle can easily fall down from the laser beam. This can be understood when it compares with the similar issue in electrodynamic levitation trap (EDLT) [PAUL 1958, TANG 1991, SUDHOLZ 1999]. In order to achieve stable levitation in EDLT, not only a DC voltage which is used to balance the droplet gravity is needed, but also an AC voltage which generates restoring forces for keeping the droplets at the desired position is essential for this technique. Similarly, in optical levitation laser beam also exerts restoring forces on

the levitated objects. These forces in optical levitation have been realized in the early experiments of this technique. For example, in 1970 Ashkin used a focused laser beam to accelerate latex spheres suspending in water [ASHKIN 1970] and he observed that there was not only a force in the direction of the laser axis accelerating the particle along the beam, but also existed other force components pulling the particle into the beam center, where is the high intensity region of the laser beam to prevent the particle from leaving its position. This force component is so called the “restoring force” in optical levitation which is important for stable levitation with a laser beam.

The net forces that laser exert on a small sphere in optical levitation is shown in Fig. 2.1. The laser beam used for levitation has an intensity profile with a Gaussian distribution and thus the highest intensity is found in the center of the beam. It is necessary to mildly focus the laser beam in order to achieve sufficient intensity for compensating the gravity of particles. As a result, the beam intensity, i.e. laser force, decreases with the increasing height above the focal point in vertical direction. Therefore, if there is particle falling into the laser beam, the gravity of the particle can be balanced by the upward light force F_{ax} at a certain distance from the waist.

The restoring forces which keep the particle in the center of the beam are provided by the so called “*radial force*” F_{rad} in the horizontal direction pointing to the high intensity region of the Gaussian beam. As shown in Fig. 2.1, we assume that the levitated particle has a higher index of refraction than the medium, and a pair of light rays **a** and **b** shine symmetrically on the particle at about its center. The light ray **a** is closer to the beam center, so that light force is higher than that of ray **b** (see Fig. 2.1). Light ray **a** is assumed to undergo both Fresnel reflection and deflection at the input and output interfaces of the particle [ASHKIN 1970]. Since most of the light hitting on the surfaces is deflected, reflection of the light is neglected in this process. As shown in Fig. 2.1, the resulting pressure force of the deflection of radiation at both input (F_D^i) and output (F_D^o) surface are inward forces pointing into the direction of the beam center. Meanwhile, for the light ray **b** it has quite similar net force construction as ray **a**, where the only difference is that the resulting forces of ray **b** are pointing to the opposite direction (outward). However, because the laser beam employed here has a Gaussian profile in the TEM₀₀-mode, the light ray **a** has a higher intensity, i.e. stronger force, than light ray **b**. Consequently, under the resulting inward forces the levitated particle can always be restored into the high intensity region of the laser

beam until the point where the inward and outward forces are equal to each other, where no radial force component is present.

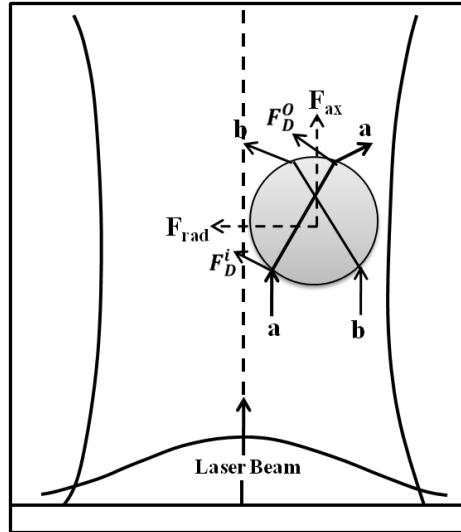


Figure 2.1 Net forces that a focused laser beam exerts on a small spherical particle. The laser beam has a Gaussian profile of intensity. The particle is located off-axis. Two parallel rays **a** (with higher intensity) and **b** (with lower intensity) shine on the particle.

Once a droplet is trapped into a laser beam, it may survive for several hours without falling and can be easily manipulated with high accuracy by varying the laser power or the position of the laser beam. More details about the droplet manipulation can be found in Section 3.2.

It should be noted that it is also possible that the index of refraction of the particles is lower than that of the medium. As a result, for such kind of particles the final apparent radial forces will reverse and the sphere will be always pushed out of the laser beam. To have stable levitation of such a kind of particles, a TEM_{01}^* laser beam mode, which has an intensity minimum on the beam axis [ASHKIN 1980], is needed.

2.2 Thermodynamic Equilibrium of Aqueous Solution Droplet

In this work we study the homogeneous nucleation process in supersaturated salt solutions, where the formation and the growth process of subcritical cluster in single levitated droplets are monitored. For these purposes, XANES spectroscopy is used for

probing the local structure in the supersaturated solution before spontaneous crystallization occurs. Such measurements require long observation times which can be achieved if the investigated droplets are in a thermodynamic equilibrium with their surroundings before nucleation. Therefore, it is important to understand the thermodynamic properties of solutes in supersaturated droplets.

For aqueous droplets a main factor that determines their thermodynamic properties in the atmosphere environment is the partial water vapor pressure over the droplet surface. For example, if the vapor pressure is higher than that of the environment, water molecules will evaporate from the droplet-air interface until it reaches a balance with its surroundings and a vapor pressure equilibrium is established. It has been demonstrated that the water vapor pressure of a liquid droplet depends on the droplet radius and the surface curvature which are related to the size of the droplet. The relation for pure water droplets can be expressed by the Kelvin equation in terms of molar units as following:

$$\ln S = \ln \frac{P_A}{P_A^0} = \frac{4\sigma\bar{v}_l}{RTD_p} \quad (2.2)$$

where P_A is the actual equilibrium partial pressure of the substance A over the curved liquid interface, P_A^0 is the vapor pressure over the flat surface of pure A , the saturation ratio of the liquid S is defined as P_A/P_A^0 , σ is the surface tension, \bar{v}_l is the volume occupied by one molecule in the liquid, R is the universal gas constant, T is the temperature in Kelvin, and D_p is the diameter of the droplet.

According to Eq. (2.2), the change in vapor pressure over a pure water droplet is given in Fig. 2.2 as a function of droplet diameter (dashed line). Obviously, the vapor pressure of droplets is a decreasing function of droplet diameters. This implies that a small decrease in droplet size due to water evaporation, results in a higher water vapor pressure over droplet surface. Therefore, droplet diameter undergoes further decrease till the entire droplet evaporates in a few seconds. This explains why water droplets can be levitated only for short time at ambient conditions.

In fact, liquids or droplets existing in the atmospheric environment are mostly composed of different kinds of aqueous solutions, instead of pure water. Thus, dissolved species have to be considered. In the following, the electrolyte is named B ,

such as KBr or NaBr, which is dissolved in the solvent A, i.e. water. It is assumed that such a droplet with diameter of D_p contains n_B moles solute in n_A moles water.

According to Raoult's law, the partial water pressure over the flat surface of the solution can be described as:

$$P_{A_{sol}}^0 = \gamma_A x_A P_A^0 \quad (2.3)$$

where γ_A is the water activity coefficient of the solution, and x_A is the molar ratio of the solvent which equals to $x_A = n_A / (n_A + n_B)$.

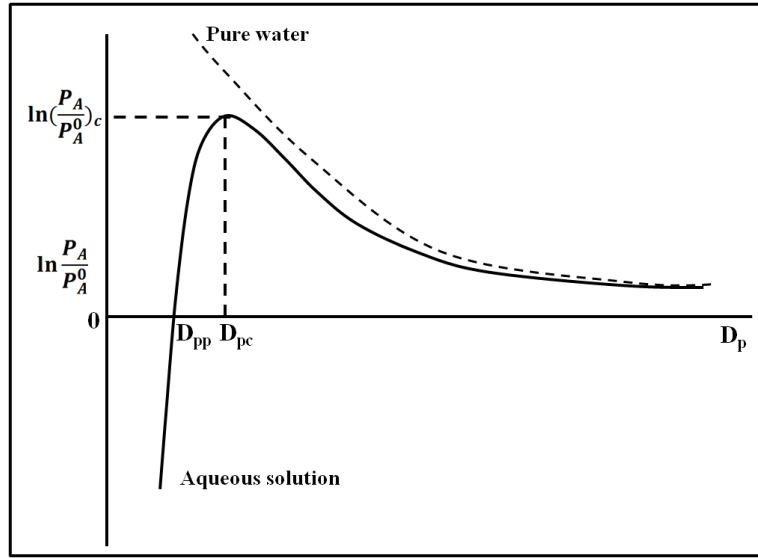


Figure 2.2. Köhler curve describing the ratio of vapor pressure above droplets containing aqueous solutions over that of pure water with flat surface as function of the size of the droplet in diameter. The solid line is for the droplets containing electrolyte solutes and the dashed line corresponds to the droplet of pure water [SEINFELD 1988].

If one substitutes Eq. (2.3) into Eq. (2.2) one can derive the Kelvin equation of aqueous solutions, which is given by:

$$\ln S = \ln \frac{P_A}{P_{A_{sol}}^0} = \ln \frac{P_A}{\gamma_A x_A P_A^0} = \frac{4\sigma \bar{v}_A}{RTD_p} \quad (2.4)$$

where \bar{v}_A is partial molar volume of water in the solution. If we assume the partial molar volume of the solute is \bar{v}_B , then the volume of the droplet can be expressed by:

$$\frac{\pi}{6} D_P^3 = \bar{v}_A n_A + \bar{v}_B n_B \quad (2.5)$$

Substituting this description into the Kelvin equation (Eq. 2.4) one receives:

$$\ln \frac{P_A}{P_A^0} = \frac{4\sigma\bar{v}_A}{RTD_P} + \ln \gamma_A - \ln \left[1 + \frac{n_B \bar{v}_A}{\frac{\pi}{6} D_P^3 - \bar{v}_B n_B} \right] \quad (2.6)$$

If the volume occupied by the solute is neglected, Eq. (2.6) can be simplified as following:

$$\ln \frac{P_A}{P_A^0} = \frac{A}{D_P} - \frac{B}{D_P^3} \quad (2.7)$$

where

$$A = \frac{4\sigma\bar{v}_A}{RT} \quad \text{and} \quad B = \frac{6n_B\bar{v}_A}{\pi}$$

When comparing Eq. (2.2) and Eq. (2.7), one can realize that for a pure water droplet the vapor pressure over the surface is always higher than that over a flat surface which means that the water vapor pressure over the droplet surface is a simple decreasing function of droplet diameter and continuous evaporation of the entire droplet volume could occur. In the case of an aqueous solution containing electrolyte solutes the vapor pressure can be either larger or smaller than P_A^0 depending on the relative magnitude of the solute-effect term B/D_P^3 and the curvature term A/D_P .

The change of the vapor pressure over droplets of aqueous solutions is also shown in Fig. 2.2 with the solid line in term of $\ln P_A/P_A^0$ as a function of the droplet diameter. The value of D_P corresponding to $P_A = P_A^0$ is the *potential diameter* D_{pp} and the maximum value of $\ln P_A/P_A^0$ corresponds to the *critical size* of the diameter D_{pc} . Regardless the type of solutes in the droplet solutions and also their properties, at the critical diameter of the droplet D_{pc} , the vapor pressure can be calculated from the following expression:

$$\frac{P_A}{P_A^0} = 1 + \left(\frac{4A^3}{27B} \right)^{\frac{1}{2}} \quad (2.8)$$

Fig. 2.2 is well known as Köhler curve and each point on this curve representing an equilibrium state that corresponds to a certain droplet diameter and solute concentration. As shown by the solid curve, representing the vapor pressure over the droplet surface of electrolyte solutions, it is an increasing function of droplet size in the region of $D_p < D_{pc}$ and in contrast when $D_p > D_{pc}$ it develops into a decreasing function. This phenomenon can be interpreted as follows: We consider that an aqueous droplet has a certain equilibrium point at $\ln P_A/P_A^0$ in the portion of the curve, where $D_p < D_{pc}$. There always exists a small perturbations caused by permanent gaining and losing of water molecules from the droplet surface [SEINFELD 1988]. Therefore, for example, we assume there are a few of water molecules add to the droplet from the surroundings and result in a small increase of the droplet diameter. According to the Köhler curve, the vapor pressure over the droplet surface will also increase and some water molecules will escape from the surface to the surroundings leading to the previous equilibrium. Therefore, for aqueous droplets there is an equilibrium state, where the droplet may survive for hours before crystallization occurs. However, if droplets are at equilibrium located in the part of the Köhler curve where $D_p > D_{pc}$, the droplet diameter will continuously increase after few water molecules are attached. By contrast, if droplet lose water from the surface in the regime of $D_p > D_{pc}$, its diameter will continuously shrink to smaller size until it comes into the range of $D_p < D_{pc}$ where equilibrium can be easily established.

2.3 Homogeneous Nucleation Theory

Phase transitions are important phenomena in nature. They may involve different kinds of initializing mechanisms. For example, any changes of the experimental condition, such as temperature or pressure. Phase transitions may occur as water evaporates from the liquid surface or melting of solid crystals. Another mechanism inducing formation of a new phase during phase transitions of matter is nucleation process. This process may include either condensation of gas phase molecules, such as water, or crystallization of a melt.

A nucleation process often occurs under assistance of foreign nuclei as preferred sites for the formation of subcritical clusters. This process is called *heterogeneous*

nucleation. In contrast, nucleation occurring without any foreign nuclei is called *homogeneous nucleation*. In this work, we study specifically phase transition process from liquids to solids by homogeneous nucleation in supersaturated electrolyte solutions. A single liquid droplet of supersaturated electrolyte solution is levitated in a closed environment where the relative humidity is fully controlled (see Section 3.2 and 3.4). Because the size-dependent water vapor pressure of the droplet is at equilibrium with its surrounding environment, if we suppose that the size-variation only results from water evaporation and the amount of solute in droplet states the same, then solute concentration is actually controlled by the environmental relative humidity, i.e. partial water vapor pressure, of the droplet. Thus, as mentioned in the previous Section (Section 2.2), each equilibrium state of the droplets corresponds to a specified droplet diameter and solute concentration. Due to the contact free approach for studying levitated droplets, they can reach a high degree of saturation all the way to spontaneous homogeneous nucleation, where the homogeneous nucleation process in the droplets is initialized by local fluctuations of the solute concentration which is permanently occurring in supersaturated solutions.

The next case to consider is that the relative humidity in the surroundings of the droplets is slowly lowered. As a result, water molecules start to evaporate from the droplet surface in order to reach another equilibrium state with the surroundings. Consequently, the solute concentration increases until the saturation point or even beyond. It is well known that supersaturated solutions are metastable, which can be stabilized by phase transitions via solid cluster or nanocrystal formation.

Classical nucleation theory (CNT) is the most widely used theory describing the changes of Gibbs energy during the creation of new phase separation and to quantify the nucleation rate of forming clusters of critical size. This theory originally developed by Volmer and Weber in 1926 [ABRAHAM 1974] for describing condensation process of a vapor into a liquid. They claimed a strong dependence of the nucleation rate on the reversible work of embryo formation. Several shortcomings of this model were identified, where later Becker and Doering and Zeldovich substantially improved this thermodynamic approach to a more quantitative treatment [BECKER 1935, ZELDOVICH, 1942, FRENKEL, 1955]. There are further studies of more recent date on classical nucleation theory [MCDONALD 1962, MCDONALD 1963, ANDRES, 1965, ABRAHAM 1974, FRIEDLANDER 1977, SPRINGER 1978, SEINFELD 1986].

In the classical treatment many approximations are employed. For example, the clusters are considered as droplet model with sharp interface and uniform interior densities; the surface tension is treated as curvature-independent and surface energy does not change at different temperature [FOKIN 2000]; only monomer association is considered for cluster growth. All these approximations simplify the mathematical expression and of course at the same time they limit the quantitative applications of the theory. In spite of its shortcomings that are resulted from these approximations classical nucleation theory is still considered as the most important method and the foundation of most of the modern treatments of nucleation processes [DEBENEDETTI 1996]. It worth mentioning that this treatment can be applied to bubble nucleation in superheated liquids and the precipitation of crystals in supersaturated solutions.

In supersaturated solution the dissolved solute ions in excess of equilibrium concentration may form spontaneously nuclei of a new solid phase through thermal fluctuations and intermolecular interactions. This stage is the initial and decisive step of homogeneous nucleation [SKRIPOV 1974]. It has been found that in homogenous nucleation, because of the dynamic properties of the ions in a disordered aqueous solution, the initial ionic germs are formed due to the temporarily possible association of ions into ordered clusters for short periods and dissociate again into dissolved ions [HAMZA THESIS, MARTIN 2000]. The change in Gibbs' free energy during the creation of embryos as a new solid phase in solution is defined as the sum of a volume term ($V\Delta G_v$) and a surface term ($A\sigma$):

$$\Delta G = A\sigma + V\Delta G_v \quad (2.9)$$

where A is the area of the liquid-solid interface, σ is the interfacial energy which is proportional to A ; V is the volume of the embryo and ΔG_v is the excess free energy of solute per unit volume in the solid phase [TANG 1984, LARSON 1986, COHEN 1987].

Since the solid state is always more stable than liquid, therefore the changes of free energy of phase transition (ΔG_v) is negative and the free energy of the system decreases. However, in order to introduce the solid-liquid interface of the solid embryo it requires certain amount of positive free energy depending on the surface area A . Thus, the total free energy of the system increases when the surface term is dominant at small embryo size. But with the increase of the cluster size the volume term becomes dominant and Gibbs' free energy starts to decrease. Therefore, there is

a maximum value of the free energy that corresponds to the critical size of the clusters where nucleation process occurs spontaneously.

Fig. 2.3 shows the diagram of the free energy change in the entire system as function of cluster size. When clusters are smaller than the critical size, the free energy increase attributed to the creation of the solid-liquid interface of the new solid phase and thus the dissociation process of the new-formed cluster is energetically preferred. However, once the clusters reach a critical size by random interactions between solute ions, the energy released from crystal formation could compensate the energy requirement for the interface creation, so that association of clusters becomes spontaneous and the nucleation process occurs in the entire droplet volume. Therefore, the maximum value of the free energy is in fact the energetic barrier for generation of new phase in the system [KULKARNI 2002].

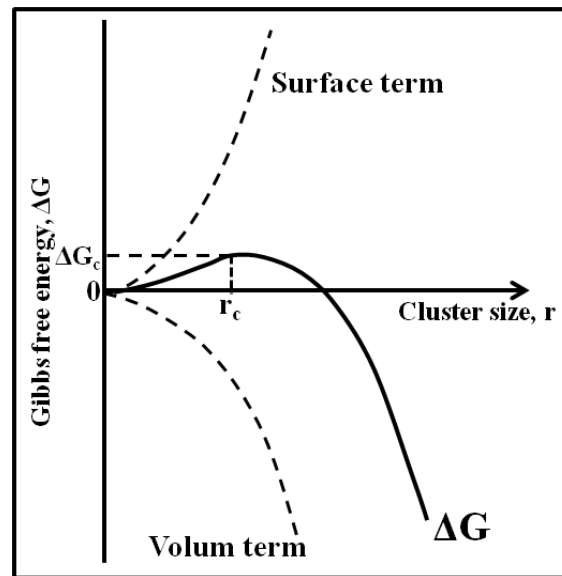


Figure 2.3. Change of the Gibbs free energy during the formation of clusters in supersaturated solution. The two dashed lines show the changes of the surface term and the volume term, respectively; the solid line presents the total change of Gibbs free energy of the entire system during the cluster formation. The maximum of the free energy corresponds to the critical size of clusters where ΔG is 1/3 of the surface energy [ERDEMIR 2009].

The critical size of the clusters can be expressed as follows:

$$r_c = -\frac{2\alpha\sigma}{3\Delta G_v} \quad (2.10)$$

where $\alpha = \sum_i k_i/l$ and k_i, l are geometry constants. It needs to be noted that the negative sign comes from the negative value of ΔG_v which can be described by:

$$\Delta G_v = -\frac{RTv\rho_{cryst}}{M_s} \ln S \quad (2.11)$$

where v is the number of ions produced by dissociation of one mole of electrolyte and R is the gas constant, ρ_{cryst} is the density of the crystalline phase and M_s is the molecular weight of the solute in the supersaturated solution.

Inserting Eq. (2.11) into Eq. (2.10), the critical size of cluster can be calculated from the following equation:

$$r_c = -\frac{2\alpha\sigma M_s}{3RTv\rho_{cryst} \ln S} \quad (2.12)$$

This equation suggests that at certain temperature, the critical size for initializing homogeneous nucleation is proportional to the interfacial energy, and inversely proportional to the saturation ratio S . This means that for clusters which have a larger surface area require bigger critical clusters. For solutions of higher concentration smaller size clusters are sufficient to initialize crystallization.

2.4 Theory of Supersaturated Electrolyte Solutions

It is well known that supersaturated solutions of strong electrolytes are in metastable states, which are characterized by permanent association-dissociation processes of solute molecules and clusters [ZETTEMAYER 1977, GUNTON 1983, MYERSON 1993]. The dissociation process of subcritical clusters is energetically favored until they reach the critical size. For critical clusters they are energetically favorable to grow via coalescence. Subsequently, the metastable supersaturated solution relaxes into a two-phase stable state by creating clusters in the solid phase and this relaxation process from a one-phase metastable state to a two-phase stable state is known as nucleation [IZMAILOV 1995].

The formation of subcritical clusters is initialized by local concentration fluctuation of the solute, where the formalism describing the relaxation process is based on an order parameter $\omega_i(r, t)$ [GUNTON 1983, MYERSON 1993, LANDAU 1986, METIU 1979] which is defined as:

$$\omega_i(r, t) = n_i(r, t) - n_{i,0} \quad (2.13)$$

where $n_i(r, t)$ is time dependent local concentration of i ions, and $n_{i,0}$ is its average concentration. Therefore, the order parameter $\omega_i(r, t)$ corresponds to the concentration fluctuation at the spatial-time location (r, t) .

The nucleation stage of the metastable state relaxation can be described in terms of relaxation of the order parameter $\omega_i(r, t)$ [IZMAILOV 1995]. One of the common approaches describing the relaxation of the order parameter $\omega_i(r, t)$ is Cahn-Hilliard formalism [GUNTON 1983, MYERSON 1993, LANDAU 1986, METIU 1979, CAHN 1958, CAHN 1959], where it is assumed that ω is conserved. In this way, the relaxation of nucleation stage is described as:

$$\frac{\partial \omega_i(r, t)}{\partial t} = \Gamma_i \nabla^2 \frac{\partial F(\omega, \varphi; t)}{\partial \omega_i(r, t)}, \quad i = 1, \dots, s \quad (2.14)$$

where

$$F(\omega, \varphi; t) = \int_V d^3r F(\omega, \varphi; r, t) \quad (2.15)$$

In Eq. (2.14), Γ_i is the ion mobility coefficient of the ion i and $F(\omega, \varphi; t)$ is the time-dependent Helmholtz free-energy functional for the supersaturated electrolyte solution, which is composed of the free energy of order parameter ω subsystem and the ion cloud φ subsystem. The functional $F(\omega, \varphi; t)$ density $F(\omega, \varphi; r, t)$ consists of the following terms:

$$F(\omega, \varphi; r, t) = F(\omega; r, t) + F(\varphi; r, t) + F_{int}(\omega, \varphi; r, t) \quad (2.16)$$

The expressions of the three terms in Eq. (2.16) are explained in the following:

The Helmholtz free-energy density functional $F(\omega; r, t)$ of the metastable ω subsystem is expressed by the Landau expansion:

$$F(\omega; r, t) = \sum_{i=1}^s \left[\frac{B_i [\nabla \omega_i(r, t)]^2}{2 n_{i,0}} + \frac{\mu_i \omega_i^2(r, t)}{2 n_{i,0}} + \frac{\eta_i \omega_i^4(r, t)}{4 n_{i,0}^3} \right] \quad (2.17)$$

where the parameter B_i is proportional to the square of the correlation radii [LANDAU 1986].

$$F(\varphi; r, t) = \frac{1}{2c^2} \left[\frac{\partial \varphi(r, t)}{\partial t} \right]^2 + U(\varphi; r, t),$$

$$\text{where } U(\varphi; r, t) = \frac{1}{2} [\nabla \varphi(r, t)]^2 \quad (2.18)$$

where c is the speed of light in the solution, $U(\varphi; r, t)$ is the potential-energy of φ subsystem.

$$F_{int}(\omega, \varphi; r, t) = -\frac{e}{\varepsilon_0 \varepsilon} \varphi(r, t) \sum_{i=1}^s z_i \omega_i(r, t) \quad (2.19)$$

where ε_0 is the permittivity constant of the vacuum. Eq. (2.19) describes the interaction between the ion-cloud potential $\varphi(r, t)$ and electric charges at the spatial-time point (r, t) .

For the case of binary ($i = 1, 2$) electrolyte solutions which are used for this work, when the solution is supersaturated and the parameters η_1 and η_2 of the ω -subsystem density function Eq. (2.17) satisfy $\eta_1 = \eta_2 = \eta$, where the Gibbs-Duhem relationship has the following form:

$$N \frac{d\mu_{slv}(T, n_0)}{dn_0} = -n_0 \frac{d\mu_{slt}(T, n_0)}{dn_0} \quad (2.20 a)$$

where

$$\frac{d\mu_{slt}(T, n_0)}{dn_0} = \frac{kT}{n_0} + \left[\frac{(|z|e)^3}{16\pi(2kT)^{1/2}(\varepsilon_0 \varepsilon)^2} \right] n_0^{-1/2} - \frac{(|z|e)^8 \eta}{640\pi^3 (kT)^4 (\varepsilon_0 \varepsilon)^7 a} \quad (2.20 b)$$

From this expression one can derive the formulism describing the solvent activity $\lambda_{slv}(T, n_0)$ of the solution:

$$\lambda_{slv}(T, n_0) = \lambda_{slv}(T, 0) \exp \left[-\frac{1}{N} \left[n_0 + \frac{2^{1/2}(|z|e)^3}{48\pi(kT)^{3/2}(\varepsilon_0 \varepsilon)^2} n_0^{3/2} - \frac{(|z|e)^8 \eta}{1280\pi^3 (kT)^5 (\varepsilon_0 \varepsilon)^7 a} n_0^2 \right] \right] \quad (2.21)$$

It is already known [GUNTON 1983, MYERSON 1993, LANDAU 1986, METIU 1979] that at concentrations corresponding to the spinodal line, which is located between the metastable and unstable state, the first derivative of the solute chemical potential is zero:

$$\left. \frac{d\mu_{slt}(T, n_0)}{dn_0} \right|_{n_0=n_{spin}(T)} = 0 \quad (2.22)$$

Inserting Eq. (2.20 b) into Eq. (2.22) results into the following formulism for the spinodal concentration $n_{spin}(T)$:

$$kT + \left[\frac{(|z|e)^3}{16\pi(2kT)^{1/2}(\epsilon_0\epsilon)^2} \right] n_{spin}^{1/2}(T) - \frac{(|z|e)^8\eta}{640\pi^3(kT)^4(\epsilon_0\epsilon)^7 a} n_{spin}(T) = 0 \quad (2.23)$$

It is assumed for a supersaturated solution, that the distance between ions with opposite electric charge may become smaller than $r_{ass} = (|z|e)^2/(2\epsilon_0\epsilon kT)$. Then, they may associate to form Bjerrum pairs, which are electrically neutral. The degree of association defines the probability for an arbitrary ion forming a Bjerrum pair, which is given by the following expression:

$$d(T, n_0) = const \times \sum_{l=1}^{N_c(T, n_0)} e^{-F_l(T, n_0)/kT} \quad (2.24)$$

Here *const* is the normalization constant, $F_l(T, n_0)$ is the Helmholtz free energy of cluster, l is the number of Bjerrum pairs contained in the cluster, and $N_c(T, n_0)$ is the number of the monomers. It implies for a supersaturated solution, that the number of Bjerrum pairs aggregating into clusters is larger than $N_c(T, n_0)$, when the nucleation process occurs. This provides another point of view for the occurrence of nucleation.

2.5 Discrete Dipole Approximation

The discrete-dipole approximation (DDA) is a powerful method for computations of absorption and scattering of targets of arbitrary geometry [DRAINE 1994]. An

oscillating field, such as the electromagnetic wave, can induce a dipole moment at any point of an exposed microparticle [BOHREN 1998], so that a continuum target in DDA is presented by a finite array of polarizable points with a local electric field. Further, there are also dipole-dipole interactions [PURCELL 1973, DRAINE 1988]. Therefore, DDA is also named as coupled dipole approximation [SINGHAM 1986, SINGHAM 1987]. This approximation method along with its recent developments has been reviewed in other papers [DRAINE 1994, BOHREN, 1991].

The scattering problem of a finite array of point dipoles can be exactly solved, so that the only approximation that is needed in DDA is the arrangement of the array of N -point dipoles, which replaces the continuum target. The replacement requires the specification of both the geometry (location r_j) of the dipoles $j = 1, \dots, N$, and the dipole polarizabilities α_j .

DDA is totally flexible regarding the geometry of the target, if it takes into account that the interdipole separation d is smaller than any structural lengths in the target and the wavelength λ . The second criterion can be determined by [DRAINE 1993, DRAINE 1994, DRAINE 2000]:

$$|m|kd < 1 \quad (2.25)$$

where m is the complex refractive index of the target material, $k \equiv 2\pi/\lambda$, and λ is the wavelength in vacuo.

We consider the volume of the target V , and replace it by an array of N dipoles which are located in a cubic lattice with the lattice spacing d , where $V = Nd^3$. The “effective radius” a_{eff} is used to characterize the size of the target, which can be written as:

$$a_{eff} = (3V/4\pi)^{1/3} \quad (2.26)$$

Then Eq. (2.25) can be written as:

$$N > (4\pi/3)|m|^3(ka_{eff})^3 \quad (2.27)$$

Therefore, targets with large value of $|m|$ also require a large number of dipoles for the target replacement. The representation of the dipole array can be generated automatically by software, such as DDSCAT 7.0, or it also allows the manual arrangement from users [DRAINE 2004].

The orientation of the target with arbitrary geometry can be freely changed relatively to the incident radiation in the laboratory frame, as shown in Fig. 2.4. The incident radiation in the laboratory frame propagates in the $\hat{x} = \hat{x}_{LF}$ direction, and $\hat{y} = \hat{y}_{LF}$ is the direction of the real component (at $\hat{x}_{LF} = 0, t = 0$) of the first incident polarization mode. The target orientation in this coordinate system is denoted by the axes \hat{a}_1 and \hat{a}_2 . Specifically, the target axis \hat{a}_1 is defined by the angles Θ and Φ ; this is followed by the determination of \hat{a}_2 axis, according to the angle β which is characterizing the rotation of the target around \hat{a}_1 . This yields for $\beta = 0$, that the \hat{a}_2 axis is located in the \hat{a}_1, \hat{x}_{LF} plane [DRAINE 2004].

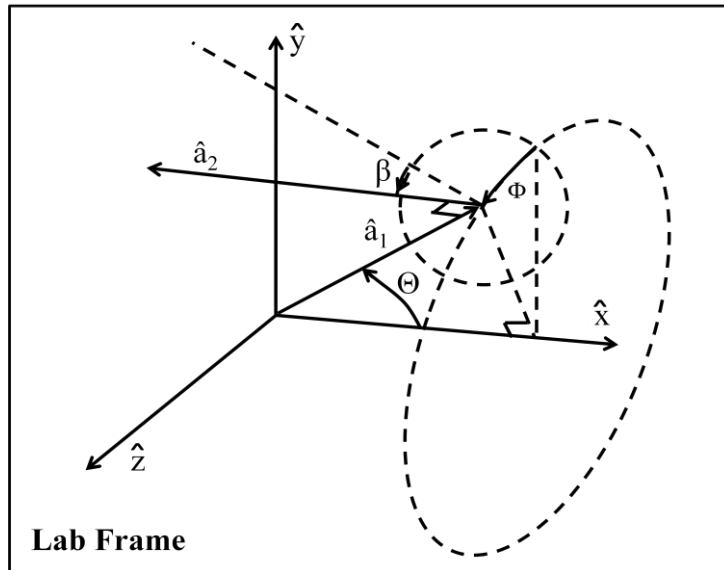


Figure 2.4. Target orientation in the laboratory frame [DRAINE 2004].

For a given oriented target, its electromagnetic scattering problem is determined by the point dipoles ($j=1, \dots, N$) with the polarizabilities α_j , which are located at the position r_j . The polarization of each dipole is then given by:

$$P_j = \alpha_j E_j \quad (2.28)$$

where E_j is the resulting electric field of incident wave and N-1 dipoles at r_j .

$$E_j = E_{inc,j} - \sum_{k \neq j} A_{jk} P_k \quad (2.29)$$

where $-A_{jk}P_k$ is the electric field at r_j that is due to the dipole P_k at r_k , including retardation effects. For a diagonal polarizability $A_{jj} \equiv \alpha_j^{-1}$ the extinction and absorption cross section can be evaluated [DRAINE 1988].

For monochromatic incident waves the self-consistent solution for the oscillating dipole moment P_j may be found. From these the absorption and scattering cross sections are computed [DRAINE 1988]. If DDA solutions are obtained from two independent polarizations of the incident wave, then the complete amplitude scattering matrix can be determined [DRAINE 1988].

2.6 X- Ray Absorption

X-ray absorption spectroscopy (XAS) [STÖHR 1992], including X-ray absorption near-edge structure (XANES) spectroscopy and extended X-ray absorption fine-structure (EXAFS) spectroscopy, is an appealing technique carrying local information around the excited atom. This is due to the fact that the local surroundings of the absorber are sensitive to the chemical state and the local atomic structure of the excited atom and neighboring sites.

Often absorption experiments are not used, rather than yields of electrons or ions which are formed after photoexcitation in the core level regime. Therefore, this experimental technique is based on the photoelectric effect which is known since more than a century. An electron can be removed from a matter when the incident radiation has a higher energy than the binding energy of the electron and the excess energy is mostly transferred into kinetic energy of the emitted electron.

In XAS, the incident X-rays are most often provided by synchrotron radiation, which is a broadly tunable and intense radiation source. Since the binding energy of the core-level electron is element-specific one can investigate a certain selected atom by confining the X-ray energy in a near regime of the absorption edge under study. During an energy-scan across an absorption edge, one can observe a sudden rise in the absorption cross section, which is called ‘absorption edge’. Above this edge the electron is emitted via direct ionization into the continuum, as shown in Fig. 2.5.

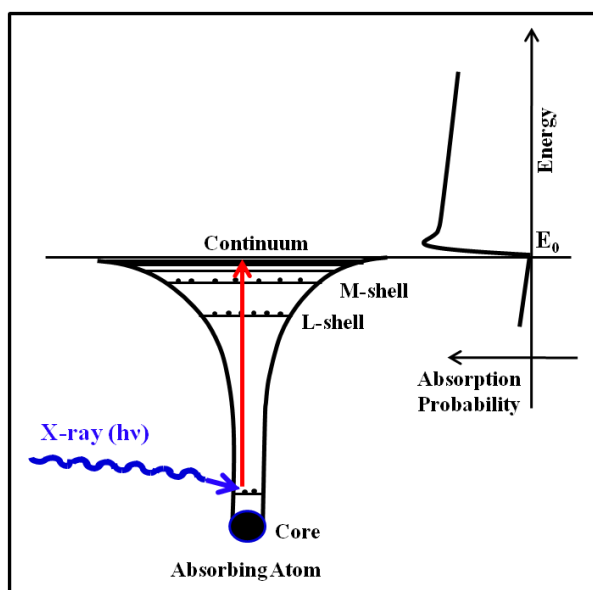


Figure 2.5. Schematic representation of core electron excitation into the continuum and the formation of corresponding absorption edge in an X-ray absorption spectrum (XAS).

The core-electron can be either excited into bound electronic states which are below the ionization energy (IE), or in the continuum regime above the IE, as shown in Fig. 2.6. It should be noted that in the continuum above IE the core-excited system may undergo multi-electron excitations which includes shake-up process or *shape resonances*. Shape resonances occur when the excited electron is trapped by a molecular potential barrier for a short period of time before being able to leave the system. The position of the shape resonance has been correlated with the adsorbate-substrate bond length in an empirical model of “bond length with a ruler” [STÖHR 1992, STÖHR 1984] where bond lengths are simply determined from the energy position of the shape resonance relative to the core ionization energy, where the resonance shifts to lower energy when the bond length increases. Although arguments and debates regarding to this simple model have been discussed for more than 10 years [PIANCASTELLI 1999], it provides a possibly linear relationship between the energy position of shape resonance and molecular bond length [STÖHR 1992].

A “core-hole” is left behind after the excitation of the core electron by an X-ray photon, as shown in Fig. 2.6 (a). Because of the localized nature of the core-hole one is able to extract the local electronic structure around the specific atom in an element-specific way [STÖHR 1992, NILSSON 2004]. Following the core-hole creation event, the excited atom is in a metastable state which spontaneously decays within a few

femtoseconds by releasing the excess energy. There are two possible mechanisms for the relaxation of core-excited atoms which are shown in Fig. 2.6. (b) and (c). The first possible way (Fig. 2.6. (b)) is via X-ray fluorescence emission, where an electron from a higher energy level fills the deeper core-hole followed by emission of an X-ray photon of well-defined energy. This de-excitation process also obeys dipole selection rules which mean that an electron transition can only occur between $\Delta l = \pm 1$ states. This implies in the case of core-hole (K-shell) de-excitation, only electrons in valance states with local p-character have a non-zero transition probability [NILSSON 2004].

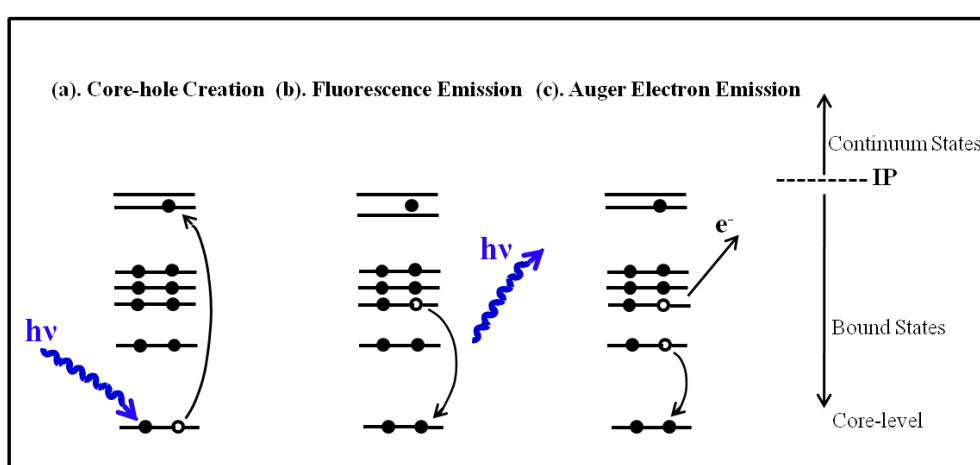


Figure 2.6. Illustration of electron-excitation and relaxation process. (a) is the creation of core-hole by absorbing an X-ray photon. Relaxation of this excited system can occur via fluorescence emission (b) or Auger electron emission (c).

The second process of core-hole decay is called *Auger effect*. In this process the energy that is released during the core-hole relaxation is used for the emission of another outer-shell electron and creates another vacancy so that the final product is doubly charged (see Fig. 2.6 (c)). The second ejected electron is therefore called an *Auger electron* [IUPAC 1997]. Further, double and multiple Auger processes are known to occur, leading to multiply charged products [CARLSON 1965, CARLSON 1966].

It should be noted that normally in the hard X-ray regime ($E > 2$ keV), the emission of X-ray fluorescence has a higher probability for high Z -elements [STÖHR 1992]. On the other hand, in the energy regime of soft X-rays Auger electron emission is dominant for low Z -elements. Both, the emitted photons (X-ray fluorescence) and

ejected electrons (Auger electron) produced during the core-hole decay can be detected to gain specific information of the system under study. It is important to note that the emitted X-ray fluorescence has a considerably longer mean free path (~ 10 μm) than Auger electrons. Therefore, X-ray fluorescence can be used to probe the bulk of a material. In contrast, Auger electrons have very short mean free path and “escape depths”, therefore, this process is inherently surface sensitive.

In this work the fluorescence yield is measured as function of the incident X-ray photon energy. Due to the dipole selection rules mentioned above, the detected energy range is set near the K_α transition of a selected atom. Thus, one is able to avoid detection of scattered light from the incident X-rays.

2.7 Density Functional Theory

In recent years, computational chemistry has become one of the fundamental tools which are applied to various fields, including chemistry and biology. It offers valuable information for reliable predictions or interpretation of reaction mechanisms [SIEGBAHN 2003, BLOMBERG 2001] and enzyme function [HIMO 2003], assisting the analysis of experimental data from different techniques. For example, the theoretical simulation of core-level spectra, as described in the previous Section provides specific information on chemical bonding [NILSSON 2004]. In this work we extend this approach for studying of local structure of excited atom in aqueous solutions containing electrolytes and clusters occurring in supersaturated solutions. Various time-dependent configurations are calculated in order to follow the evolution of solute cluster formation in supersaturated solutions and to compare these with the corresponding dilute solutions as well as the corresponding crystals.

2.7.1 Basics of Quantum Chemistry

The mathematical foundation of theoretical computations on energy levels or other properties of atoms and molecules by quantum chemistry is represented by the time-independent Schrödinger equation [BALL 1999]:

$$\hat{H}\psi = E\psi \quad (2.30)$$

where \hat{H} is the full Hamiltonian of the physical system describing the interactions of the nuclei and electrons as well as their kinetic terms, and ψ is the wavefunction of the system. The energy of the system E is determined by the value of Hamiltonian and can be expressed by:

$$E = \frac{\langle \psi | \hat{H} | \psi \rangle}{\langle \psi | \psi \rangle} \quad (2.31)$$

Due to numerous electronic interactions in molecular systems, the full Hamiltonian becomes complicated and the corresponding Schrödinger equation is almost impossible to be solved precisely. Therefore, proper approximations for the simplification of simulations are required.

One of the basic simplifications is the Born-Oppenheimer approximation [BORN 1927] where the position of the nuclei is considered to be fixed because of their large mass compared to that of electrons. This means that the electrons have a separated motion and the Schrödinger equation is solved for a “fixed” nuclear system.

However, the calculation of the electronic Schrödinger equation for many-body systems is still costly and further simplifications are necessary. The Hartree-Fock (HF) method is one of the most commonly used methods for calculating the molecular ground-state energy [HARTREE 1928, FOCK 1930] and it considers that each electron is moving under the force of an average field which is generated by the other electrons. This means that the correlation between electrons is neglected and each electron is associated with a single-electron wavefunction depending on the spatial coordinates and the spin of the particle.

Naturally, beyond the Hartree-Fock approximation further theoretical techniques are based on variational principle or perturbation theory [BARTLETT 1994]. These have been developed for determining the difference between the Hartree-Fock energy and the exact value which is also defined as the *correlation energy*. Although some of the methods give good agreements with the real value, high cost of computation still limits their applications in reality.

2.7.2 The Kohn-Sham Theory

Like Hartree-Fock method, many classical methods for the determination of electronic configurations are based on complicated wavefunction of many-body systems. The high cost of computations makes them not appealing. Historically, Density Functional Theory (DFT) was developed with the idea of using the electronic density, instead of a many-body wavefunction to portray the electronic interactions of a given system. This provides an important and unknown aspect of nature and allows one to have an alternative approach for studying electronic configurations. The reason for the simplicity of DFT is: Each electron has 3 coordinates x, y, z , the wavefunction of N electrons in a many-body system has $3N$ degrees of freedom. However, the electronic density $\rho(r)$ of the system can be easily described by a function with 3 degree of coordinates, which simplifies the whole calculation task tremendously.

DFT was initially proposed through Thomas-Fermi model in the 1920s [THOMAS 1927, FERMI 1927], and became popular after publication of the two Hohenberg-Kohn theorems [HOHENBERG 1964]. The first Hohenberg-Kohn theorem states that with the absence of magnetic field, the ground state energy of a given system can be expressed by only the function of the electronic density $\rho(r)$. In other words, the electronic energy of the ground state can be obtained by varying $\rho(r)$. The second Hohenberg-Kohn theorem demonstrates that the minimized energy of a system as the functional of electron density $\rho(r)$ is also the unique ground state energy of the system.

The Hohenberg-Kohn theorems indicate the correspondence between the ground state energy and the electron density $\rho(r)$, rather than their exact relation. Further applications of DFT in a wide scientific area are accomplished by implementation of the Kohn-Sham DFT formalism where to find the minimized energy functional by adjusting $\rho(r)$ of an N electrons system [KOHN 1965]. In this formalism, the electronic energy is presented as a functional of the electronic density $\rho(r)$ and is separated into:

$$E[\rho] = T_e[\rho] + U_{ext}[\rho] + U_{ee}[\rho] \quad (2.32)$$

where T_e is the kinetic energy of non-interacting electrons with the same density of the real system, U_{ext} is the external potential of the positive nuclei felt by the electrons and U_{ee} is the energy of interactions between electrons.

The external potential is known as the form of:

$$U_{ext}[\rho] = \int \rho(r) \sum_{\alpha} \frac{-Z_{\alpha}}{|R_{\alpha} - r|} dr = \int \rho(r) \hat{U}_{ext}(r) dr \quad (2.33)$$

where Z and R are the nuclear charge and coordinates, respectively.

The interacting energy among electrons $U_{ee}[\rho]$ is the sum of the pure Coulomb interaction and the exchange and correlation contribution.

$$U_{ee}[\rho] = \int \rho(r) U_{cl}(r) dr + E_{xc}[\rho] \quad (2.34)$$

where $U_{cl}(r)$ is in form as:

$$\hat{U}_{cl}(r) = \int \frac{\rho(r')}{|r' - r|} dr' \quad (2.35)$$

Inserting Eq. (2.33), (2.34) and (2.35) into Eq. (2.32), the Kohn-Sham formalism can be written as follows:

$$E[\rho] = T_e[\rho] + \int [\hat{U}_{ext}(r) + U_{cl}(r)] \rho(r) dr + E_{xc}[\rho] \quad (2.36)$$

Unfortunately, the accurate expression of the term for the kinetic energy $T_e[\rho]$ between interacting electrons is not known, and therefore the solution of this problem is to replace $T_e[\rho]$ by the kinetic energy of non-interacting electrons $T_0[\rho]$. The correction for the difference between $T_0[\rho]$ and $T_e[\rho]$ is introduced by the classical Coulomb potential. Moreover, there is also no straightforward method to derive the accurate value of exchange-correlation energy $E_{xc}[\rho]$. The most simple standard approximation to $E_{xc}[\rho]$ is done by the local density approach (LDA), where $E_{xc}[\rho]$ is determined by only the local density at \mathbf{r} . LDA give good agreement with experiments to bulk materials, but it exhibits shortcomings for materials of rapidly varying density. An improved method to LDA is called generalized gradient approximation (GGA) functional where the dependence of the gradient of the density on \mathbf{r} is considered. Since the inhomogeneity of the electron density is taken account, GGA functionals, such as Becke [BECKE 1988], PW 86 [PERDEW 1986], and BLYP [LEE 1988], produce accurately comparable results to high-level *ab initio* methods but with much less computational cost. [HANDY 2000].

2.8 Core-Level Electron Energy Loss Spectra Calculations

Electron energy loss spectra (EELS) is an important core-level spectroscopy technique in which the energy loss of an electron beam propagating through a sample is measured via an electron spectrometer [EGERTON 1996]. These spectra are essentially identical with XAS, in which the reduction of an X-ray beam is measured [JORISSEN 2010]. This Section briefly summarizes the ab initio quantum-mechanical simulation packages used to compute core-level EELS: Cambridge Serial Total Energy Package (CASTEP) [CLARK 2005, ACCELRYN 2008] and Car-Parrinello Molecular Dynamics (CPMD) [CAR 1985, HUTTER 2001]. These two programs are plane-wave pseudopotential codes to solve the one-electron Kohn-Sham equations within the methodology of density functional theory (DFT). The wavefunctions of valence electrons are expanded in a plane-wave basis set by using periodic boundary conditions and Bloch's theorem.

2.8.1 CASTEP

Core-level EELS requires all-electron wave functions inside the core region together with the inclusion of core-hole effects and, therefore, core orbitals have to be considered explicitly in the pseudopotential methods used in CASTEP; hence a special formalism is required [PICKARD 1997, PICKARD THESIS, REZ 1999] which involves a projector augmented wave (PAW) reconstruction of the wavefunction inside the core region and an on-the-fly generation of excited ultrasoft pseudopotentials to account for the core-hole effect [GAO 2008]. This implementation has shown good agreement for simulating K-edge spectra for a variety of different materials [GAO 2008, MILMAN 2010, AGUIAR 2010, SEABOURNE 2008].

2.8.2 CPMD

The Car-Parrinello Molecular Dynamics (CPMD) [CAR 1985, HUTTER 2001] is a method that performs ab-initio (first principles) molecular dynamics (MD) using a plane wave basis set and periodic boundary conditions and density functional theory.

The idea behind the Car-Parrinello method is to explicitly introduce the electronic degrees of freedom as (fictitious) dynamical variables and employ by an extended

Lagrangian coupling the motion for both ions and electrons in the system. Standard CPMD simulations calculate only the evolution of the occupied Kohn-Sham states. For the computation of X-ray absorption spectra (XAS), it is also necessary to determine the unoccupied levels. This could be done by using the Kohn-Sham potential obtained from the optimized wave functions of occupied orbitals. Applying the potential into a Lanczos diagonalization [FILIPPONE 2001] one can derive a number of unoccupied states. More details of this method are introduced in reference [CAVALLERI 2004].

Chapter 3

Experimental Details

The experimental setups on trapped single microparticles used in this work, including optical levitation combined with synchrotron radiation and electrodynamic levitation, are non-commercial developments, and therefore, will be described in greater detail in this Chapter. Synchrotron radiation [BATHOW 1966, HORST 2004, INTE 4, FOLLATH 2004] and droplet generator (piezo-injector) [TURKMEN THESIS] have been fully described somewhere else, and therefore, are not introduced in this work.

3.1 Optical Levitation of Single Droplet

The optical levitation setup used in this work is shown in Fig. 3.1. Microdroplets are stored in a levitation cell ($2 \times 2 \times 7$ cm) which is made of Plexiglas to isolate the droplets from the environment, so that the humidity can be controlled. A home-made piezo-injector [TURKMEN THESIS] is mounted on top of the levitation cell, which is used to generate microdroplets of aqueous solutions with diameters of typically 30 μm . A cw-laser beam ($\lambda = 532$ nm) (diode-pumped laser (5 W, Verdi, Coherent)) is vertically fed into the levitation cell from the bottom. Usually, in order to have sufficient laser power to compensate for the gravitational force of the microdroplets ejected into the trap, a focusing lens with $f = 80$ mm is mounted below the levitation cell, as shown in Fig. 3.1. Therefore, the intensity of the laser beam has a decreasing gradient above the beam waist, and single droplets can be levitated at a certain point inside the beam where the light force is equal to the droplet gravity. One can then vary the power of the laser beam and adjust the equilibrium position, i.e. the position of the trapped droplet in the trap chamber. The experiments indicate that at 2.0 W of laser power the microdroplets are held about 5 mm above the focal point.

Once the droplets are levitated, Mie scattering patterns are recorded in order to determine the droplet diameter and index of refraction by using known methods, such as the Fourier transform of the scattering patterns or just counting the stripes on a CCD-camera [STEINER 1999, BERGE 1999, MUND 2003]. In this work, mostly we

determined the diameter of the levitated droplet by a rough estimate directly from the number of the stripes in the image of Mie scattering (as shown in Fig. 3.2) according to $x = 180^\circ n_{fringes} / \Delta\theta$ [MUND 2003]. The accuracy of this approach for estimation the particle size is of the order of 15%.

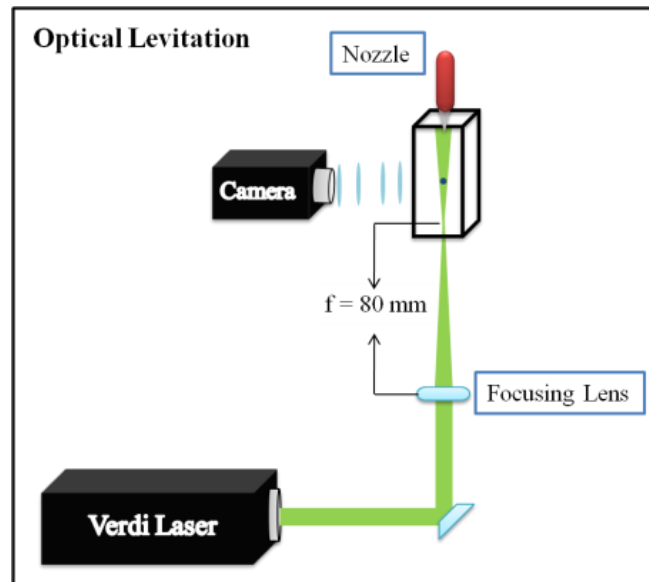


Figure 3.1. Experimental setup for optical levitation. A cw-laser beam is focused by a lens with $f = 80 \text{ mm}$. Droplets are generated by a piezo nozzle and they are introduced into the laser beam in the center of the levitation cell. A CCD-camera is used to view the position and the scattering pattern of the levitated droplet.

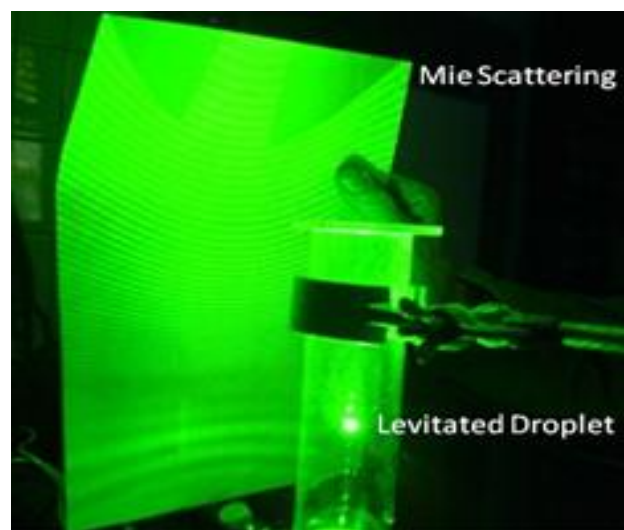


Figure 3.2. Photograph of a single levitated droplet by optical levitation and its Mie scattering pattern.

The levitation of droplets in a focused laser beam is stable once the droplet is trapped in the laser beam. Subsequently, it can be slowly moved into three-dimensions by moving the laser beam. This will be discussed in more detail in Section 3.2.1. The position of the levitated droplet can be viewed and adjusted by the help of a CCD-camera mounted at an angle of 90° relative to the laser beam. A lens system is mounted in front of the CCD-camera in order to magnify the droplet. Further details of the optical system are shown in Fig. 3.3. The magnification of this optical system is experimentally determined by using a copper mesh of $60\text{ }\mu\text{m}$ mesh constant which is defined as the distance between the centers of two adjacent wires. The mesh constant on the CCD-camera chip is amplified to 3.67 mm , which implies that the magnification of the lens system is 61.2.

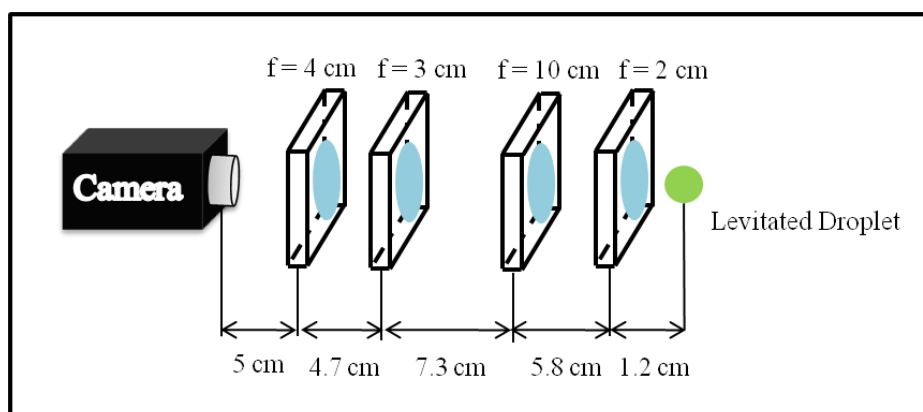


Figure 3.3. The magnification system in front of the CCD-camera, which is composed of several focusing lenses as indicated.

3.2 XANES Spectroscopy on Single Levitated Droplets

3.2.1 Experimental Details of Optical Levitation in Combination with Hard X-rays

XANES spectra of single levitated microdroplets were successfully measured for the first time by a combination of optical levitation and tunable X-rays from the synchrotron radiation facility BESSY II at Helmholtz Zentrum Berlin (Germany). The experiments were performed at KMC-2 beamline, covering the energy regime between 4 and 15 keV. A sketch of the experimental setup is shown in Fig. 3.4.

Synchrotron radiation is introduced into the levitation cell from behind (see Fig. 3.4). It is noted that in order to enhance the signal intensity, a capillary lens is used to focus

the X-rays on an area of $120 \times 120 \mu\text{m}^2$ containing $10^8 - 10^9$ photons. The X-ray fluorescence signal emitted from the levitated droplet is detected by a Si-PIN photodiode (Pacific silicon sensor series 7, PR 200-7-CER-2 PIN). According to the dipole selection rules (see Section 2.5), the fluorescence emitted after X-ray absorption basically results from K_α radiation. Because mostly K_α transition lines of an absorber occur at lower energy than its K-edge, scattered X-rays from the droplet are excluded from the signal.

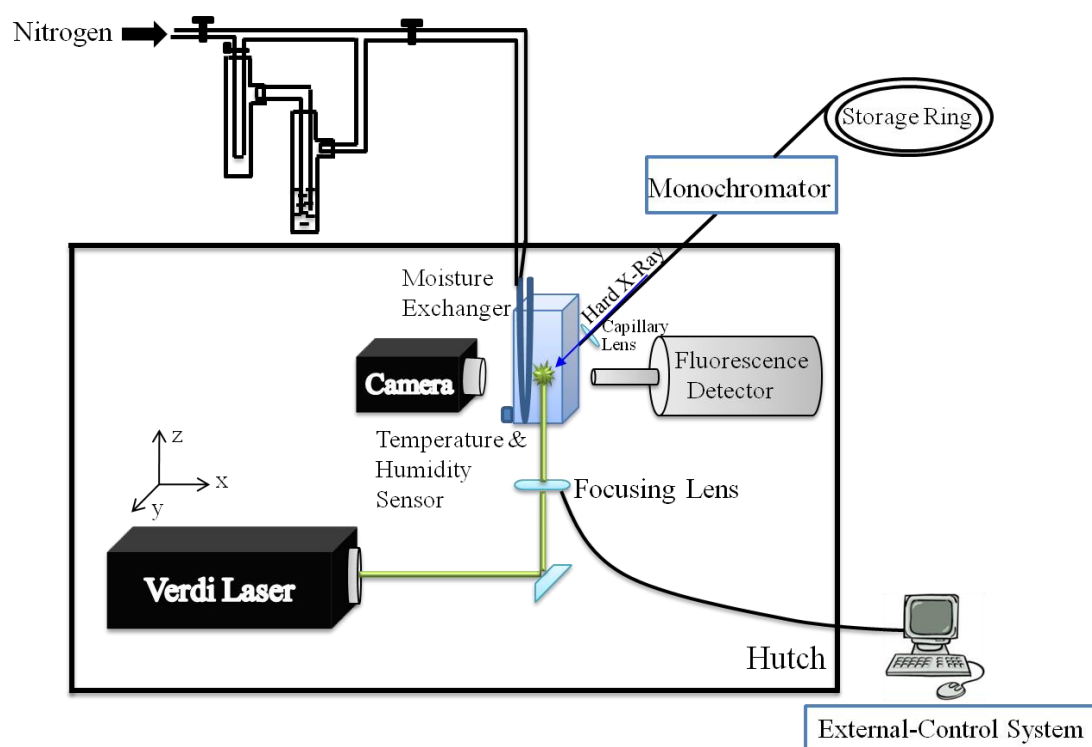


Figure 3.4 Experimental setup of optical levitation. The experiments are carried out at the BESSY II storage ring.

The humidity conditions inside the levitation cell are controlled by a moisture exchanger (Perma Pure METM-Series) which is connected to a gas flow system. As shown in Fig. 3.4, the flow system is composed of two containers, where one is empty, which is used for safety reasons in order to avoid a backflow of water in case of a gas pressure difference. The other one contains water which increases the moisture of the flowing gas. The moisture exchanger is made of a Nafion membrane to transfer water to or from a gas flow until the humidity inside and outside the tube reaches an equilibrium. Dry nitrogen is used as a carrier gas, which partially passes

through the water gas and get humidified. A desired humidity is therefore achieved by adjusting the flow ratio of the wet gas. It is noted that the relative humidity is a temperature-dependent quantity. Therefore, it can be affected by several factors, such as the heat from the levitating laser and those droplets that are injected into the levitation cell without getting caught may also results in additional changes of the humidity. Therefore, stabilization of humidity has to be carefully monitored during the experiments.

Due to the hazards of the hard X-rays the entire experimental setup, except the gas flow system, is mounted inside a closed hutch. Since any evaporation or condensation of water on the droplet surface could affect the position of the levitated droplet in the trap, it is important to be able to adjust the position of the droplet from outside the hutch. This is accomplished by mounting an optical system which guides the path of the levitating laser beam on a PI microstep motor stage (MercuryTM – PI), remotely controlled from outside the hutch.

Fig. 3.5 shows the optical system which is constructed on three motors which allow movements into x, y, and z direction, respectively. *Mirror 1* is fixed to *Motor 2*, which is allowed to move in the x-direction along the rail of *Motor 1*. Another motor (*Motor 3*) is built together with the fixed *Mirror 2* on the rail of *Motor 2*. This provides the movement in y-direction. Finally, the focusing lens is built on the rail of *Motor 3* along the z-direction. This construction allows the laser beam to move levitated droplets in x-direction by *Motor 1*, y-direction by *Motor 2* and z-direction by *Motor 3*. It is noted that the movement of levitated droplets in z-direction is accomplished by moving the focal point of the lens, which varies the beam intensity relative to the beam of synchrotron radiation.

Motorized versions of the M-405 DG linear positioning stage series (PI, Physical Instruments) have a maximum range of 50 mm with the designed resolution of 0.025 μm . The lowest achievable velocities reach down to 10 $\mu\text{m/s}$, as used to manipulate the laser beam with the levitated particles. The motors were driven by MercuryTM DC motor controllers (C-863 type). The experimental control was done with LabVIEW in order to integrate the control software into the main experimental data acquisition program. The serial RSC-232 communication is also used for the LabView programs driving the cw-laser (Coherent, Verdi), and the humidifier uses a USB port. A RSC-232 serial communication port COM was used for data transfer.

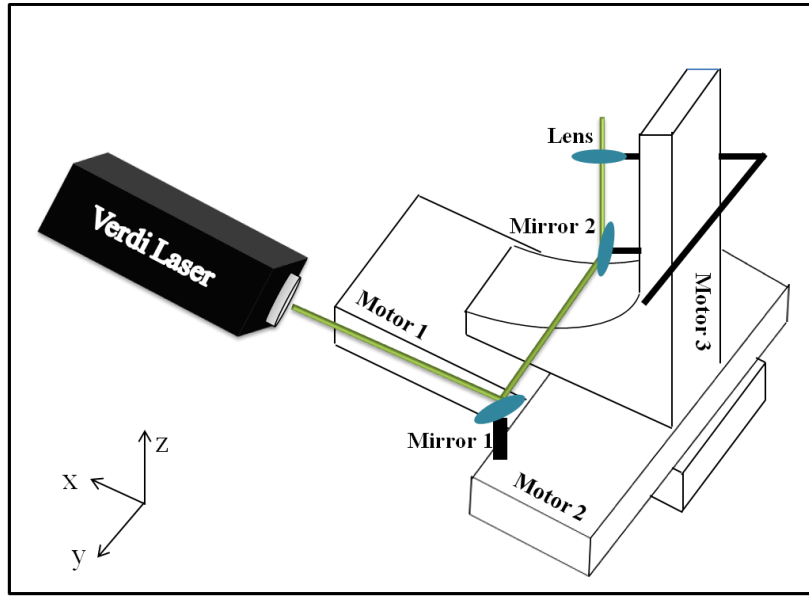


Figure 3.5 Optical system constructed on PI microstep motors, which allow the laser beam carrying the levitated droplet to move in three dimensions. *Mirror 1* and *Mirror 2* are reflecting mirrors; the *lens* is used to focus the vertical laser beam, which is reflected by mirror 2. The three motors can be moved in x, y, z directions, respectively.

3.2.2 Preliminary Adjustment

The critical step for the experiments of this work is to bring the levitated droplet into the monochromatic synchrotron radiation beam by transferring the levitation laser beam with the 3 motors described in the previous Section. An efficient way to achieve this is to use a thin wire of 100 μm diameter in order to simulate the position of the levitated droplet. The center of the synchrotron beam is assigned according to the absorption signal of the wire.

As shown in Fig. 3.6, the thin wire which is mounted on the same motor (*Motor 3*) as the focusing lens is aligned along the laser beam. Perfect alignment is reached, when the focused laser beam hits exactly the wire tip. Most microdropets are suspended between the tip of the wire and the focusing lens, which are separated by 80-85 mm. Then, the thin wire and the laser beam are moved simultaneously to cross the synchrotron radiation beam. X-ray absorption spectra arising from the thin wire tip are then used to assign the central position of the X-ray beam. Due to the fact that the intensity of the synchrotron radiation beam presents a Gaussian distribution, the absorption signal reaches its maximum value when the thin wire is placed into the

middle of the beam, as depicted in Fig. 3.7 (a) and (b). Finally, we lift the wire in the z direction until the absorption signal equals half of the maximum intensity, as shown in Fig. 3.7 (c). The wire tip is then assigned as the center of the synchrotron radiation, and its position is monitored by the CCD-camera. Thus, when the image of a levitated microdroplet appears at the same position as that of the wire tip, one can ensure the droplet is in the synchrotron radiation beam.

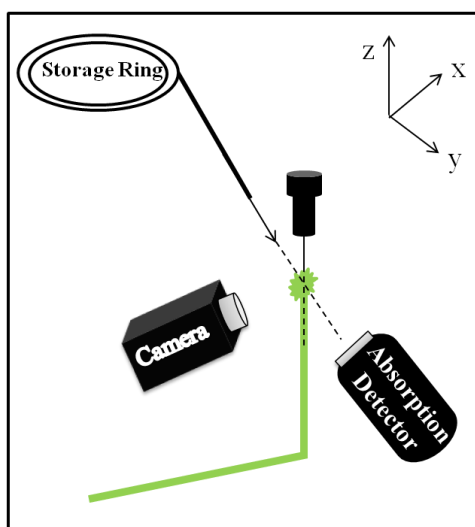


Figure 3.6 Schematic representation of the preliminary adjustment of the laser beam (in z direction) when crossing with the synchrotron radiation (in y direction). A thin wire is used as simulate the microdroplet in order to align the laser beam in z direction. X-ray absorption spectra are recorded by an absorption detector along the y axis. A CCD-camera, which is mounted at 90 °scattering angle relative to the X-ray beam, is used to view the wire position via a monitor outside the hutch.

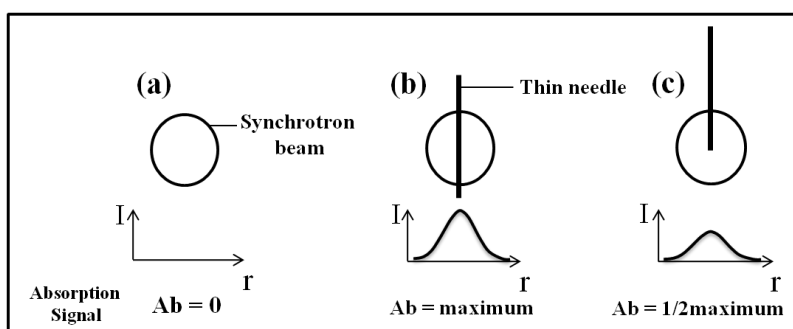


Figure 3.7 Determination of the center of the X-ray beam according to the intensity of the absorption spectra. (a) zero absorption ($Ab = 0$) when the thin wire is completely out of the beam; (b) maximum absorption ($Ab = \text{maximum}$) when the wire passes through the entire X-ray beam from the middle; (c) half maximum absorption ($Ab = 1/2 \text{ maximum}$) when the wire tip is at the center of the X-ray beam.

It is noted that after such preliminary adjustment, the laser beam is crossed by the synchrotron radiation with an accuracy of $<5 \mu\text{m}$. Levitated microdroplets can be brought into the X-ray beam by moving them along the z direction. This can be accomplished either by moving the focusing lens with *Motor 3* or by varying the intensity of the laser beam.

3.3 Experimental Setup for XANES Studies using Soft X-Rays

XANES spectra of single optically levitated droplets were studied in the energy regime of soft X-rays, as well. However, the mass attenuation coefficients (μ/ρ) of soft X-rays in liquid solutions are larger than that of hard X-rays, (see Table 3.1) [HUBBELL 2007]. In the case of single levitated microdroplets, hard X-rays are able to penetrate the entire droplet. In contrast, soft X-rays can only excite molecules about $3 \mu\text{m}$ from the surface, and therefore, fluorescence emitted by irradiation of soft X-rays is considerably weaker than that of hard X-rays. The recording of XANES spectra at such weak signals failed, and therefore, an alternative method to generate bigger droplets is used, as explained in the following.

Table 3.1. The mass attenuation coefficients (μ/ρ) for soft and hard X-rays in liquid water. These values are nearly the same for aqueous solutions used in this work [HUBBELL 2007, SINGH 1998].

	Soft X-rays ($E_{\text{Photon}} = 1 \text{ keV}$)	Hard X-rays ($E_{\text{Photon}} = 10 \text{ keV}$)
μ/ρ of water	$4 \times 10^3 \text{ cm}^2/\text{g}$	$5 \text{ cm}^2/\text{g}$

Fig. 3.8 shows the experimental setup for recording XANES spectra using soft X-rays. A pipette is used for generating single droplets of larger diameter ($d = 1.5\text{-}2 \text{ mm}$). Electrolyte solutions filled into a pipette tip are slowly pushed out to form a single droplet which still has contact with the solution inside the tip. Therefore, for those droplets it is difficult to reach high supersaturation and it is almost impossible to crystallize them. However, continuous evaporation of water from droplet surface results in a concentration gradient throughout the entire droplet volume, and solute

clusters may form on the liquid-air interface, where the droplet solution has higher concentration than in the pipette reservoir.

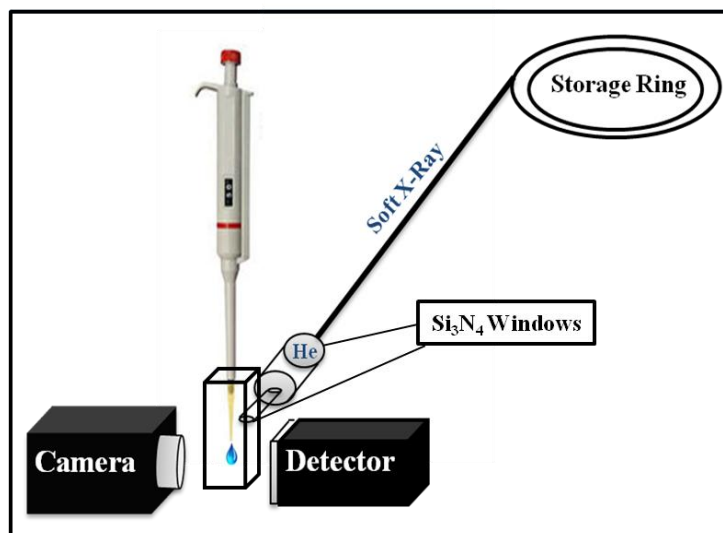


Figure 3.8 Experimental setup of XANES spectroscopy using soft X-rays. A single droplet with a diameter of 1.5 - 2 mm is suspended on a pipette tip. The droplet is stored in a closed container filled with helium gas to avoid absorption of fluorescence radiation in air. The X-ray beam is introduced by a steel tube (see text for further details).

The soft X-rays were provided by a plane grating monochromator beamline in Physikalisch-Technische Bundesanstalt (PTB) Berlin, which provides tunable undulator radiation in the photon energy range from 78 eV to 1860 eV. The radiation is guided into a closed levitation cell by a steel tube, which has two Si₃N₄ windows at the ends (see Fig. 3.9). Because one of the Si₃N₄ windows is directly connected to the beamline, it is necessary to minimize the size of the window in order to reduce the pressure difference between the ultra-high vacuum (about 10⁻⁸ mbar) inside the beamline and the atmospheric pressure inside the steel tube. In the present case, both windows are 150 µm in diameter. Si₃N₄ is selected as the window material, since its transmission for soft X-rays is sufficiently high. It has been calculated that the transmission of soft X-rays through the Si₃N₄ window of 100 nm thicknesses is about 93% at energy regime of Na K-edge (1070-1110 eV) [INTE5]. Therefore, about 86% of the beam intensity could pass through the two Si₃N₄ windows. Another reduction of beam intensity is caused by the strong absorption cross section of the X-rays in air. When the entire volume of the steel tube between the Si₃N₄ windows (80 mm long, 6

mm diameter) is filled by air, the transmission of soft X-rays is almost zero. To solve this problem, the steel tube is filled by helium, so that the transmission increases to about 95%. Therefore, about 82% of total intensity of the monochromatic synchrotron radiation, corresponding to 10^{11} - 10^{12} photon/sec on an area of $150 \times 300 \mu\text{m}^2$, reaches the sample depending on the band width of the photons.

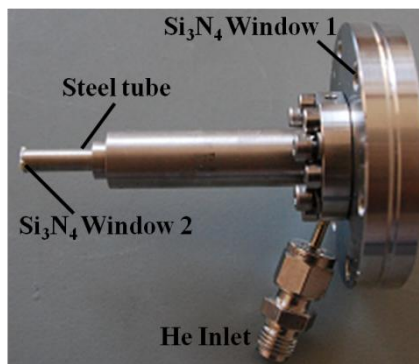


Figure 3.9 Photograph of the steel tube guiding the soft X-rays into the levitation cell, where the levitated droplets are stored. Two Si₃N₄ windows are used in both sides of the tube (see text for further details).

The fluorescence signal is detected by a SDD detector from Bruker (QUAD version of Xflash) at 90 °scattering angle. The detector is mounted as close as possible to the levitation cell, which is also filled by helium to avoid losing the fluorescence signal.

It is worth mentioning that the adjustment of the position of the levitated droplet is similar to that used for hard X-ray studies (see Section 3.2.2). The only difference is that it is not necessary to carry out the experiments inside a hutch. This avoids remote control of the adjustments and is much easier and more convenient.

3.4 Electrodynamic Levitation Trap

The essential part of electrodynamic levitation trap (EDLT) is composed of a top and a bottom cap electrode and a ring electrode in the middle (see Fig. 3.10). A dc-voltage between 0 and 300 V can be applied on the cap electrodes to stabilize the levitated droplet for compensating the gravitation force. Often, this voltage is set to 0 V. An ac-

voltage of typically 2-6 kV with a frequency of 0.07-2 kHz is applied to the central ring electrode.

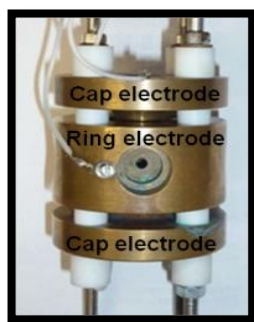


Figure 3.10 Photograph of a Paul trap. An ac-voltage is applied on the central ring electrode, and a dc-voltage is applied to the two cap electrodes located at the top and bottom of the trap.

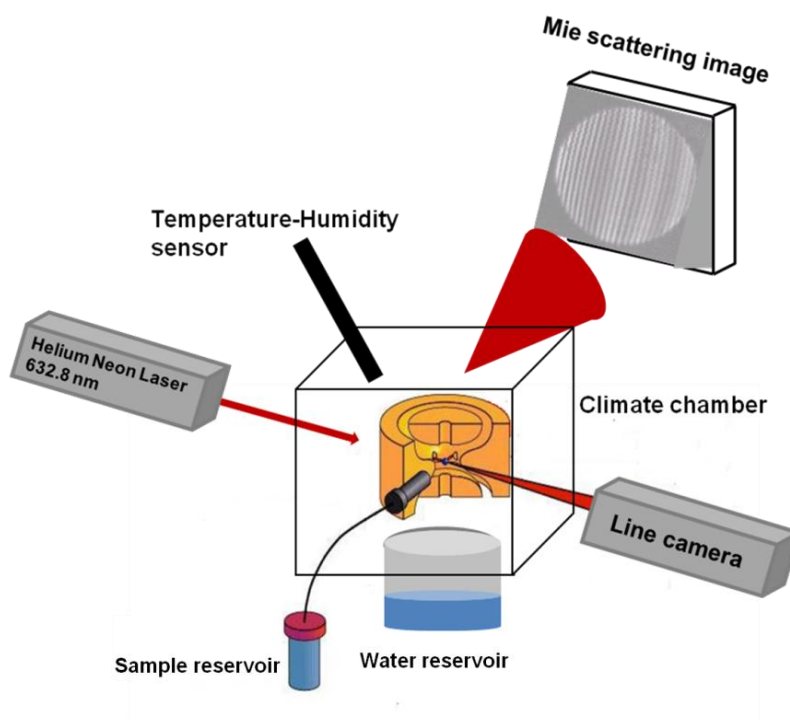


Figure 3.11 Schematic diagram of the experimental setup of the electrodynamic trap (EDLT).

The EDLT is located in a closed climate chamber, which allows us to exclude the disturbance from environment and to stabilize the humidity and temperature of the surroundings of the levitated droplet. The humidity in the climate chamber is controlled by a combination of a water reservoir and the drying agent phosphorous pentoxide (P_2O_5). They both are connected to the climate chamber through a variable

leak. By adjusting the width of the slits for both water bath and drying agent, the desired humidity can be reached and stabilized for several hours within $\pm 0.5\%$. The relative humidity is measured by a calibrated sensor (Temperature/Humidity Sensor P570, Dostmann Electronic) with an accuracy of 0.5%.

Liquid microdroplets are generated either by a piezo nozzle (Microdrop MD-E-201H) or the home-made nozzles for optical levitation. Microdroplets are directly injected into the electromagnetic field from the ring electrode and become electrically charged instantaneously [BERGE 1999]. Charged droplets are levitated in the center of the trap, where a helium-neon laser ($\lambda = 632.8$ nm) passes through. The elastically scattered light is collected by a CCD-camera at around 90° scattering angle. This allows us to observe the phase transitions of levitated particles from liquid to solid state and vice versa, corresponding to the efflorescence and deliquescence processes, respectively. When the injected droplet stays liquid, the scattered light shows the typical Mie scattering pattern [BOHREN 1983, BERGE 1999], which consists of a sequence of dark and bright stripes, which are recorded by a CCD-camera. Vanishing of these patterns and the occurrence of a irregular speckle pattern indicates the formation of solid particles [BERGE 1999]. Evaporation of water from the droplet or phase transitions change the charge-to-mass ratio so that the levitated droplet leaves the center position of the trap or even gets lost, if the ac-voltage is constant. This is avoided by using a CCD line camera (NANODIM) which provides a feed-back signal for adjusting the ac-voltage, so that the position of the droplet is kept constant. This CCD-camera detects the scattered light from the droplet in forward direction near 10° . More information of the setup applied in this work has been described in previous works [STEINER 1999, BERGER 1999, SUDHOLZ 1999, HAMAZA 2004].

3.5. Determination of the Microparticle Charge

As shown in Fig. 3.12, the net charge of single droplets flying through the electromagnetic field in the EDLT is measured by a metal electrode, which is connected to an electrometer (Keithley, model 6514). The distance between the ring electrode of the Paul trap and the electrode is about 30 mm. The magnitude of the net charge on a single droplet is measured as a function of the ac potential applied to the ring electrode, where the magnitude of the ac-voltage is proportional to the net charge

on the droplets. At each amplitude of the ac potential, the charge on a single droplet is repeatedly measured for 400 droplets generated at a frequency of 100 Hz in the piezo injector.

During injection, the droplets receive only a low net charge, which corresponds to a range of approximately $-(170 \pm 17)$ to $-(260 \pm 26)$ fC. Note that only negative excess charges were investigated in this work. The magnitude of charges is further enhanced by inserting an electrode directly into the sample vial, where a high voltage of the order of 2-3 kV is applied. As a result, the droplets are charged with the same polarity of the high voltage when they are injected into the trap. The droplets charged by this method can reach net charge of more than -2000 fC, which can also be measured by the collector electrode in absence of the electromagnetic field of the EDLT.

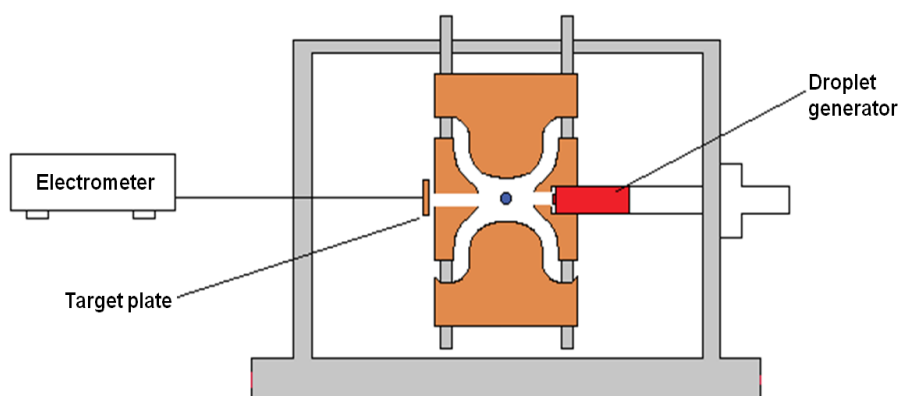


Figure 3.12 Schematic representation of the setup used to determine the particle charge in the EDLT by using a metal electrode (target plate) connected to an electrometer.

The averaged results measured using both charging methods are shown in Fig. 3.13 as a function of ac-voltage applied to the ring electrode or the voltage applied to the electrode in the sample solution, respectively. The green dots (low charge amplitude regime) correspond to the droplets charged by the ac voltage of the Paul trap. The red squares correspond to the droplets charged by an inserted electrode in the sample solutions. As shown in Fig. 3.13, droplets charged by this method have a broad distribution of charge amplitude within a range of $-(280 \pm 28)$ to $-(2200 \pm 300)$ fC.

Both charging methods are used in this work depending on the properties of the sample solutions. Further discussions regarding to this issue can be found in Chapter 4.

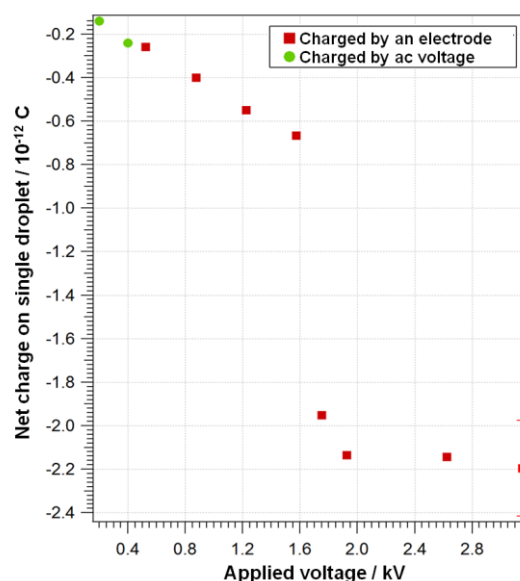


Figure 3.13 Net charges on single droplets generated by injection into an ac-field or an electrode inserted in sample solutions.

3.6 Experimental Procedure of Efflorescence Determination

In this work, the efflorescence points of single levitated droplets are measured with both optical levitation and EDLT. In EDLT only charged droplets can be levitated, but as mentioned above, this method can be used with a relatively small amount of charges on the droplets (up to $-(260 \pm 26)$ fC). In order to increase the excess charges on the droplets, we used optical levitation in order to trap droplets charged directly by electrode in the solution. Further, the efflorescence point of neutral droplets can only be measured by means of optical levitation.

The efflorescence point corresponds to the humidity, where spontaneous nucleation occurs. Therefore, the experiments are carried out where the humidity in the trap is systematically changed. The experiments start at low humidity, which is gradually increased. The increase in relative humidity leads to longer crystallization times. The experiments are terminated at $t = 600$ s, which corresponds to a stable droplet with respect to nucleation. It has been demonstrated before that the crystallization time significantly increases at a certain value of relative humidity depending on the solute and temperature [HAMZA 2004]. This relative humidity at which the sudden increase of the crystallization time takes place is defined as the “critical humidity of crystallization”, corresponding to the “efflorescence point” of the solution.

3.7 Combination of Optical Levitation and Electrodynamic Levitation

In order to study the charge effects on the nucleation process of single levitated droplets, the efflorescence point of each droplet solution are measured with both the optical levitation trap (for neutral or charged droplets) and the electrodynamic trap (for slightly charged droplets). To exclude possible sources of systematic errors, for example due to different humidity sensors, we combine the optical levitation and electrodynamic trap into the same setup, as shown in Fig. 3.14. This setup has also the advantage compared to the optical trap that the humidity can be kept constant over longer time periods due to the larger volume of the chamber, which buffers small changes in humidity.

This implies that an optical levitation setup is built into the climate chamber of the EDLT. A focusing lens is mounted below the cap electrode at the bottom of the climate chamber and the cw-laser beam is also introduced into the EDLT from the bottom. Single droplets are injected into the trap from the top (see Fig. 3.14). In optical trapping the droplets are charged by an electrode in the sample solution. The number of charges on the droplets is controlled by the voltage applied to the charging electrode in the solution, as shown in Fig. 3.13.

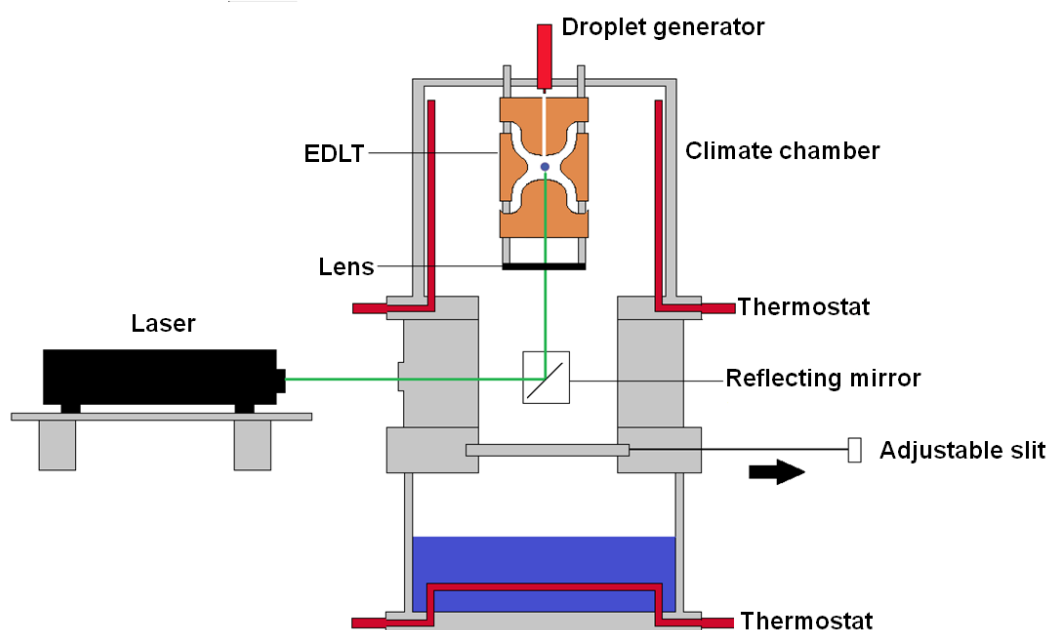


Figure 3.14 Combination of optical levitation and EDLT in the same experimental setup.

3.8 Aqueous Salt Solutions and Solid Samples

The studies of cluster formation in highly concentrated solutions are carried out by optically and electrostatically levitated droplets containing electrolyte solutions. The initial samples of aqueous solutions for droplet generation are prepared salts with purity >98% purchased from Alfa Aesar (see Table 3.2). Distilled water is used as a solvent after further purification with 0.2 μm filter. The preparation of the aqueous solutions is done by using a little less than is needed to reach the saturation point of the salt (see Table 3.2). This yields easily supersaturated solution droplets by evaporation of the solvent after trapping without blocking the droplet generator.

Table 3.2. Solutions and solid sample used in this work

	CaBr₂	ZnBr₂	NaBr	NaCl	NaF	KBr
Salt purity (Alfa Aesar)	99.5%	98%	99+ %	99.9%	99%	99.9%
Initial solute concentration (mol/L)	5.40	1.78	5.50	1.90	6.30	3.36
Efflorescence point	<5% [C2]	<5% [C2]	25-28% [C2]	45% [Czicz 1997]	n/a	56 \pm 1% [Wise 2005]
Saturation ratio at the efflorescence point	2.0	1.1	1.93	n/a	n/a	n/a

If one is only interested in homogeneous nucleation, one has to get rid of all possible impurities from the solutions contributing to heterogeneous nucleation before filling these into the droplet generator. For this purpose, we use filters of 0.2 μm to get rid of such impurities.

Each salt solution has different properties, such as viscosity, solubility in water, efflorescence point, and deliquescence point etc. Therefore, according to these properties, we chose two or three the most suitable sample solutions for each experimental purpose. For example, NaBr and CaBr₂ are used to take XANES spectra in the energy regime of Br K-edge. ZnBr₂ has a low solubility in water at ambient conditions. This sample was used to measure XANES spectra at Zn K-edge (see Section 4.2.5). KBr has an efflorescence point of 60 \pm 1% relative humidity which is easily accessible for present experimental setups. Thus, it is used for comparison of

XANES spectra pre- and post-crystallization. Finally, solutions of NaF and NaCl and NaBr are studied in the energy regime of the Na K-edge (soft X-rays). It is noted that all the solutions used in the experiments have to be freshly prepared.

Besides aqueous solutions we also studied the corresponding dilute solutions and solid pellets of the salts studied in this work. The initial concentrations of each sample solutions are given in Table. 3.2.

Chapter 4

Results and Discussion

4.1 Phase Diagrams of Electrolyte Solutions

The main goal of this work is to study phase transition processes in supersaturated solutions of electrolytes via homogeneous nucleation. Supersaturated solutions are metastable and, therefore, the association-dissociation processes of subcritical solute clusters permanently take place in solution until homogeneous nucleation occurs spontaneously (see Section 2.3). At a certain temperature, the critical size of clusters initializing homogeneous nucleation is influenced by solute concentration, which can be controlled by the relative humidity (Section 2.3). The phase diagram of the solute is of central importance for performing experiments on single microdroplets in the supersaturation regime. Therefore, in this work we have constructed phase diagrams of electrolyte solutions as a function of the temperature and relative humidity in order to gain insight into the basic understanding of cluster formation and dynamics during nucleation. We derive in the following from literature data and thermodynamic considerations the phase diagrams of the solutes studied in this work.

4.1.1 Phase Diagram of NaBr

Fig. 4.1 shows the calculated correlation between the relative humidity and the solute concentration, n_0 , of sodium bromide (NaBr) droplets. The calculation was done based on the assumption that in the equilibrium the chemical potential of the droplet solution $\mu_{slv}^L(T, n_0)$ and that of the surrounding vapor phase $\mu_{slv}^G(T, n_0)$ are equal. This means that the corresponding activities $\lambda_{slv}^L(T, n_0)$ and $\lambda_{slv}^G(T, n_0)$ are also equal to each other. Moreover, when the solvent vapor is treated as an ideal gas, one obtains the following equation [GUGGENHEIM 1967]:

$$\frac{\lambda_{slv}^L(T, n_0)}{\lambda_{slv}^L(T, 0)} = \frac{\lambda_{slv}^G(T, n_0)}{\lambda_{slv}^G(T, 0)} = \frac{P(T, n_0)}{P(T, 0)} = \frac{P(T, n_0)}{P_{sat}(T)} = R.H.(T, n_0) \quad (4.1)$$

where $P(T, n_0)$ is the temperature-dependent vapor pressure, $R.H.(T, n_0)$ is the relative humidity, and n_0 is the solute concentration given in number density. Combining this equation with Eq. 2.20 (a) and Eq. 2.21, as introduced in Section 2.4, $R.H.(T, n_0)$ can be expressed as follows:

$$R.H.(T, n_0) = e^{-(M_W/1000)n_0\psi(T, n_0)} \quad (4.2)$$

where $\psi(T, n_0)$ is the solvent osmotic coefficient, which can be calculated by the following formula:

$$\psi(T, n_0) = 1 + c_1(T)n_0^{1/2} - c_2(T)n_0 \quad (4.3)$$

The temperature-dependent coefficients $c_1(T)$, and $c_2(T)$ of NaBr can be found in Table 1 of reference [IZMAILOV 1995]. Inserting Eq. (4.3) into Eq. (4.2) one can readily obtain the exponential relation between $R.H.$ and n_0 , as depicted in Fig. 4.1.

Obviously, $R.H.$ decreases when increasing n_0 (see Fig. 4.1). This is a consequence of the fact that at low humidity the partial vapor pressure of an aqueous droplet is higher than that of its environment. Therefore, this results in further water evaporation from the droplet surface. If the amount of solute in the droplet solution is considered to be constant, its concentration will increase when decreasing $R.H.$.

According to the literature, the efflorescence point of NaBr solution is about 25% - 30% [LORENA 2008, COHEN 1987, WISE 2005]. The red dashed line in Fig. 4.1 indicates the average value (28%) of this value range. The solute concentration corresponding to this efflorescence point is about $n_0=18$ molal. Fig. 4.1 can be also used to calculate the corresponding $R.H.$ at which the solute concentration is at its saturation point, as indicated by the blue dashed line. A NaBr saturated solution (about 9 molal) corresponds to a $R.H.$ of 55%. Thus, the relative humidity window of a supersaturated NaBr solution is determined to range from about 25% to 55%. This range determines the $R.H.$ range at which the present experiments are performed. When the $R.H.$ is higher than 55%, droplet solutions are unsaturated and stay in the liquid state; but when the $R.H.$ is lower than 25%, droplets solidify immediately, i.e. efflorescence occurs in less than a few seconds.

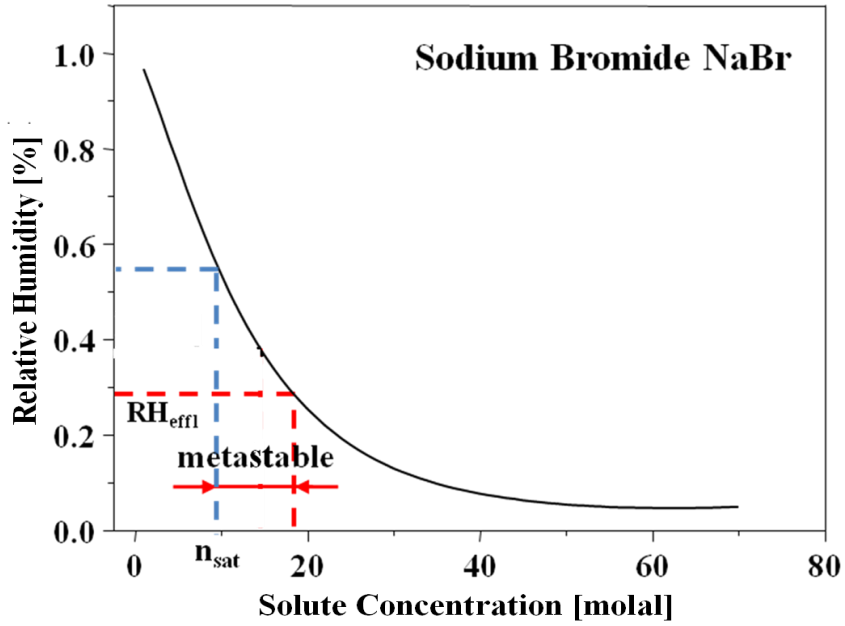


Fig 4.1. Dependence of the relative humidity above a NaBr droplet on the solute concentration n_0 . The typical droplet diameter is about 20-25 μm . The blue dashed-line indicates the saturation point and the red dashed-line stand for the solution at the efflorescence point [IZMAILOV 1995].

With the information given above one can readily construct the phase diagram of NaBr, as shown in Fig. 4.2. NaBr has four thermodynamically stable phases, which are: (i) ice, (ii) aqueous solution, (iii) sodium bromide dihydrate ($\text{NaBr} \cdot 2 \text{H}_2\text{O}$), and (iv) anhydrous cubic crystals. The coexistence line between the aqueous ice and the liquid phase is constructed which are based on literature data and are calculated from the ice vapor pressure [HUTHWELKER 2010]. The coexistence line of the sodium bromide dihydrate $\text{NaBr} \cdot 2 \text{H}_2\text{O}$ and an aqueous solution is calculated from the vapor pressure above a saturated NaBr solution [WEXLER 2010], according to the formula $R.H. = A \exp(B/T)$. The values of the constants A and B can be found in the literature [WEXLER 2010]. Finally, the coexistence line between pure, solid NaBr and the dihydrate $\text{NaBr} \cdot 2 \text{H}_2\text{O}$ is calculated according to the formula given by Halling [HALLING 1992].

Based on Fig. 4.1, the supersaturated regime corresponds to a humidity range between 25% and 55% (region within the red dashed lines in Fig. 4.2). The experimental conditions are defined to be located within the red square shown in Fig. 4.2. However, in order to ensure that the investigated solutions are supersaturated, all the experiments studying the cluster formation in droplet solutions are performed in a

humidity range of 30-50% (gray area in Fig. 4.2). According to the phase diagram, under these pre-defined conditions, one can only produce from supersaturated solutions $\text{NaBr} \cdot 2 \text{H}_2\text{O}$ or pure NaBr solid crystals. This means that supersaturated solutions of NaBr can crystallize either into hydrates or dehydrated solids, depending on the humidity conditions at which cluster formation and subsequent crystallization occurs.

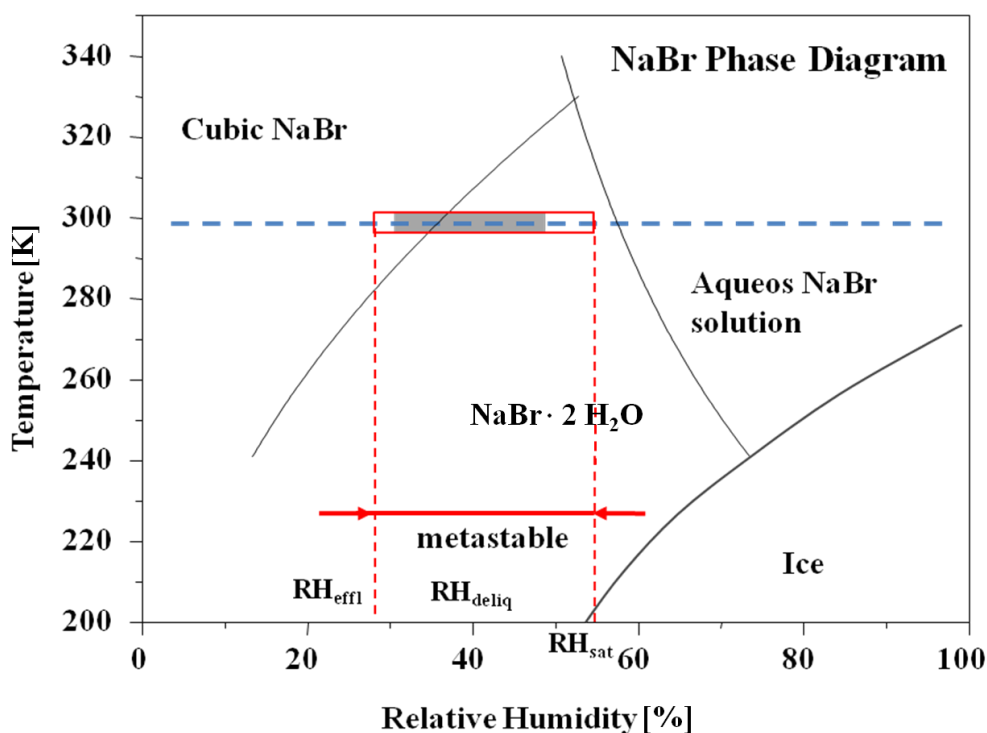


Figure 4.2. Phase diagram of NaBr as a function of the temperature and the relative humidity. NaBr has four stable phases: $\text{NaBr} \cdot 2 \text{H}_2\text{O}$, cubic NaBr (dehydrated solid), aqueous NaBr solution, and ice. The metastable regime for our studies is indicated by a red box, which is limited by the relative humidity of efflorescence and the saturated point at the temperature where the present studies were performed ($298 \pm 2 \text{ K}$). The blue dashed line indicates standard temperature ($T = 298 \text{ K}$). All experiments were carried out considering a relative humidity ranging from 30% to 50%, as indicated by the gray area (see text for further details) [HUTHWELKER 2010, WEXLER 2010].

From an atomistic point of view, in supersaturated solutions positively and negatively charged ions are attracted by electric forces by forming ion-pairs (Bjerrum pairs) which could further aggregate to form solute clusters. Thus, each Bjerrum pair can be considered as an elementary building unit of a crystal formed from supersaturated solution. From a classical point of view (see Section 2.3), only clusters reaching a

critical size can initialize crystallization processes and form solid crystals through the entire droplet volume. Therefore, if we consider that solute clusters are constituted of Bjerrum pairs, the number of Bjerrum pairs contained in critical clusters can be defined as the “critical number size $N_c(T, n_0)$ ” at a certain temperature. Suitable estimations of $N_c(T, n_0)$ provide another important parameter for describing homogeneous nucleation processes.

The estimation of the critical number size $N_c(T, n_0)$ can be carried out using Eq. 2.24 which was introduced in Section 2.4. Unfortunately, it is not possible to derive a finite value of n_c using this equation and to determine the exact value of $N_c(T, n_0)$. Alternatively, one can calculate the upper, $N_{c,max}(T, n_0)$, and the lower, $N_{c,min}(T, n_0)$, limits of the critical size [IZMAILOV 1995] at a certain temperature and solute concentration. In order to derive such estimate, two constraints on $N_c(T, n_0)$ are introduced:

$$N_c(T, n_{sat}(T)) = \infty$$

$$N_c(T, n_{spin}(T)) = 1$$

The meaning of these constraints is that for solutions at the exact concentration of saturation, $n_{sat}(T)$, critical clusters require an infinite number of Bjerrum pairs to start crystallization. For supersaturated solutions of spinodal concentration, $n_{spin}(T)$, only a single Bjerrum pair is sufficient to initialize a phase separation by nucleation. This means that a single Bjerrum pairs is sufficient to form infinite critical clusters [IZMAILOV 1995, CAHN 1958, UNGER 1984]. By considering these two constraints, the upper and lower limits can be calculated by the following equations:

$$N_{c,min}(T, n_0) = \frac{1}{\ln\left[\frac{n_0}{n_{sat}(T)}\right]} \ln\left[1 - \frac{n_{spin}(T)}{d(T, n_{spin}(T))} \frac{d(T, n_0)}{n_0} \left[1 - \frac{n_0}{n_{sat}(T)}\right]\right] \quad (4.4)$$

$$N_{c,max}(T, n_0) = \frac{1}{\ln[\xi(T)n_0]} \ln\left[1 - \frac{n_{spin}(T)}{d(T, n_{spin}(T))} \frac{d(T, n_0)}{n_0} [1 - \xi(T)n_0]\right] \quad (4.5)$$

where

$$\xi(T) = \frac{1}{n_{sat}(T)} - \frac{1}{n_{spin}(T)} \frac{d(T, n_{spin}(T))}{d(T, n_{sat}(T))} \quad (4.6)$$

$n_{sat}(T)$ can be easily calculated from the solubility of solutes in water, n_0 is the average concentration in the droplet solution, and $n_{spin}(T)$ is tabulated in the literature [Izmailov 1995].

Fig. 4.3 shows the calculated curves of the estimated upper, $N_{c,max}(300\text{ K}, n_0)$, and lower, $N_{c,min}(300\text{ K}, n_0)$, limits of the critical number size in NaBr clusters, $N_c(300\text{ K}, n_0)$, as a function of the solute concentration at ambient conditions. Both $N_{c,min}(300\text{ K}, n_0)$ and $N_{c,max}(300\text{ K}, n_0)$ are decreasing functions of n_0 . This is consistent with the formulism for calculating the critical diameter of solute clusters (see Eq. 2.12). In fact, the number size of critical clusters always decreases with increasing solute concentration, regardless the type of solutions. This is one of the reasons why crystallization is easier to achieve in concentrated solutions. Moreover, the number size difference between $N_{c,max}(300\text{ K}, n_0)$ and $N_{c,min}(300\text{ K}, n_0)$ also decreases with solute concentration. As shown in Fig. 4.3, the area between the two calculated curves becomes smaller with increasing n_0 . This indicates that the size distribution of critical clusters are smaller at higher solute concentration n_0 . Therefore, the accuracy of the calculation of $N_c(300\text{ K}, n_0)$ also increases with n_0 .

Note, that in Fig. 4.3 we give the number size of critical clusters as a function of solute concentration, n_0 , and, therefore, the supersaturated regime of NaBr solution should be also defined according to the solute concentration. The concentration corresponding to the efflorescence point, n_{effl} , of the NaBr solution can be obtained from Fig. 4.1. The calculated value ($n_{effl} = 18$ molal) together with the concentration at the saturation point ($n_{sat} = 7.8$) is indicated by red dotted lines in Fig. 4.3. The corresponding values of n_{effl} on both $N_{c,max}(300\text{ K}, n_0)$ and $N_{c,min}(300\text{ K}, n_0)$ curves are $N_{c,max} \approx 2.5$ and $N_{c,min} \approx 2.3$, respectively. This suggests that when the concentration of a NaBr solution is close to n_{effl} , critical clusters contain at most 5 solute ions. This critical size increases rapidly with the decrease of solute concentration and becomes infinite in the range between n_{sat} and $1.1n_{sat}$. Therefore, in order to study nucleation processes occurring spontaneously in supersaturated NaBr solutions, it is necessary to ensure that the solute concentrations are in the supersaturated regime and the number size of critical clusters is not infinite. However,

even within the supersaturated regime, lower concentrations than n_{effl} correspond to a larger critical number size and less ionic interactions. Therefore, aqueous droplets in this work could survive for hours before crystallization spontaneously occurs and long observation times are possible for such studies.

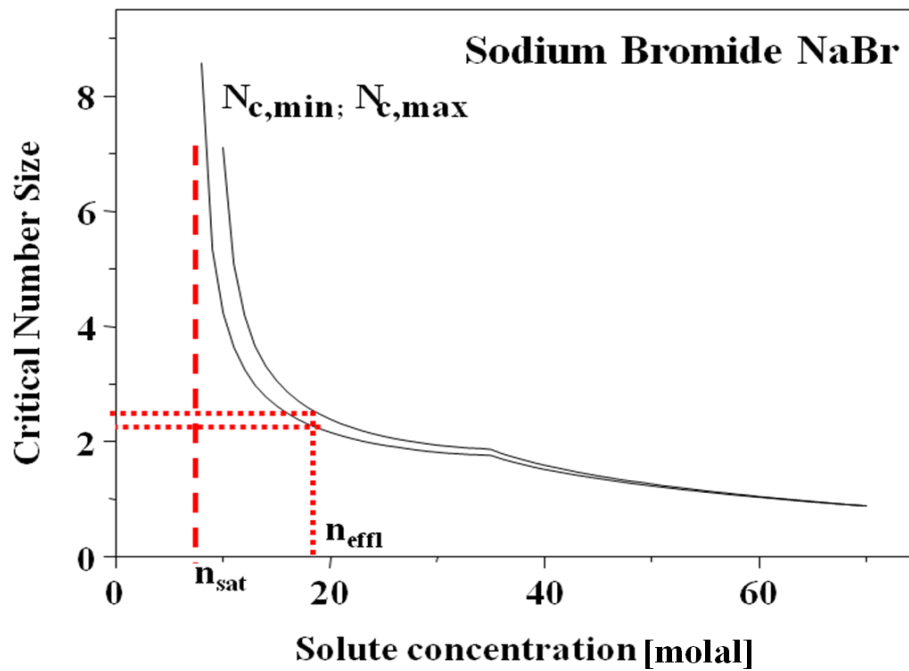


Figure 4.3. The calculated curve of upper, $N_{c,\text{max}}(300, n_0)$, and lower, $N_{c,\text{min}}(300, n_0)$, limits with respect to the number size of critical clusters, $N_c(300, n_0)$, in a NaBr solution as function of solute concentration at a given temperature ($n_0(300)$). The dashed line indicates the number size of critical cluster corresponding to the saturation concentration and the dotted lines show the values of $N_{c,\text{max}}(300, n_0)$ and $N_{c,\text{min}}(300, n_0)$ corresponding to the solute concentration at the efflorescence point [IZMAILOV 1995].

4.1.2 Phase Diagrams of CaBr_2 and ZnBr_2

Together with NaBr we also consider in this work the solutions of calcium bromide (CaBr_2) and zinc bromide (ZnBr_2). Because CaBr_2 and ZnBr_2 solutions have similar properties, but different ones from that of NaBr, we discuss the phase diagrams of these two solute systems together in this Section.

One of the most important properties of these solutes that are different from NaBr is that both CaBr_2 and ZnBr_2 are hygroscopic at ambient conditions. It means that they have a strong affinity for moisture and intend to absorb large amounts of water vapor

from the ambient surroundings. Furthermore, as CaBr_2 and ZnBr_2 dissolve readily in water when they absorb water from surroundings, deliquescence arises readily. CaBr_2 and ZnBr_2 are so hygroscopic that crystallization can only occur at low humidity, i.e. the efflorescence point of these solutions is lower than 5%. Unfortunately, such low humidity is difficult to achieve in the present experiments performed at ambient conditions. Therefore, the XANES spectra of these solutions have to be measured at higher humidity than their efflorescence points (see Section 4.2.3 and 4.2.5), and there is no need to define the humidity regime for supersaturated droplets of CaBr_2 and ZnBr_2 solutions. Nevertheless, their phase diagrams are still necessary to know in order to understand their phase transition properties.

Fig. 4.4 shows the calculated phase diagram of CaBr_2 . There are three stable phases: (i) aqueous solution, (ii) the hydrate ($\text{CaBr}_2 \cdot 6 \text{H}_2\text{O}$), and (iii) the anhydrous solid (CaBr_2). Note that there should be also the stable phase of ice available in the area of high humidity and low temperature. However, due to the lack of literature data, it is not possible to calculate the coexistence line between ice and the liquid phases. In any case, this limitation is of no importance to the present studies since we are only interested in the transition process from the liquid to the solid states. The coexistence line of aqueous solution and hydrated solids ($\text{CaBr}_2 \cdot 6 \text{H}_2\text{O}$) was calculated with the same method used for constructing the phase diagram of NaBr . For the phase coexistence lines between hydrate and anhydrous CaBr_2 clusters, no exact data can be found in the literature and the only available information is that above 35°C anhydrous clusters are formed and below this temperature hydrate solids are dominant [GMELIN]. Therefore, the hydrate-anhydrous coexistence line is considered to be at an absolute temperature of 308 K, regardless of the humidity of the surroundings. As the anhydrous phase appears at low relative humidity and high temperature regime, where no experiments in present work are performed, such a rough approximation of the coexistence line does not cause any errors of the measurements.

The phase diagram shown in Fig. 4.4 is mainly divided into an aqueous solution and the hydrate $\text{CaBr}_2 \cdot 6 \text{H}_2\text{O}$. The room temperature value, as indicated by a blue dashed line, determines the coexistence point between the liquid phase and hydrate crystals $\text{CaBr}_2 \cdot 6 \text{H}_2\text{O}$ and it corresponds to the “critical humidity” at which the phase transition tends to occur. The critical humidity for an aqueous solution of CaBr_2 at room temperature is considered to be at about 16% (see Fig. 4.4). Thus, the

experimentally metastable state of a supersaturated CaBr_2 solution is approximately considered to be found below 16%, as shown in Fig. 4.4. Nevertheless, for experiments making use of optical levitation, it is difficult to successfully levitate aqueous droplets at a relative humidity lower than 30%. This is because the CaBr_2 solution condensates close to the outlet of droplet generator and the ejection of microdroplets is hindered. Therefore, measurements of CaBr_2 droplets had to be carried out at higher humidity.

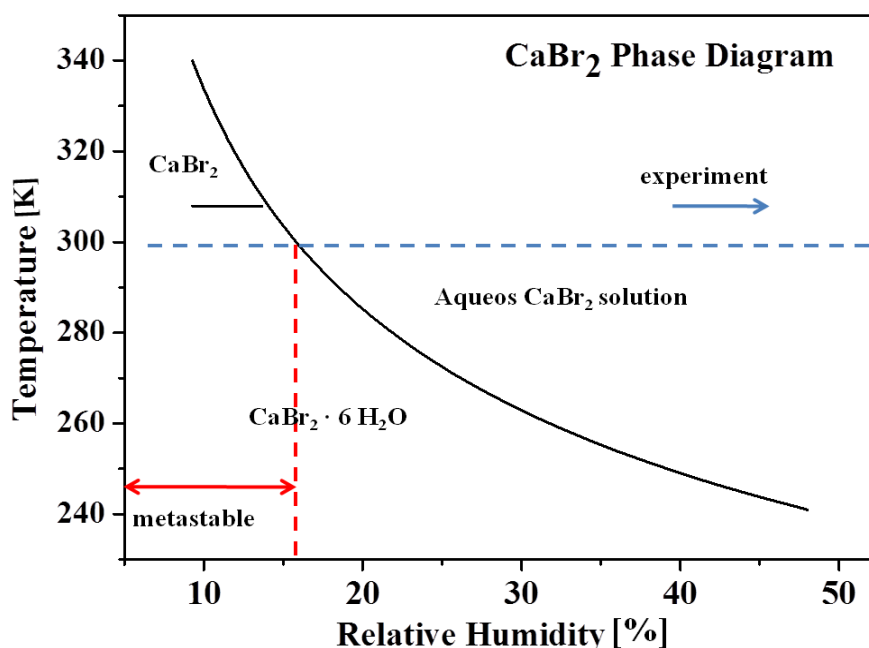


Figure 4.4. Phase diagram of CaBr_2 as function of temperature and relative humidity. The aqueous CaBr_2 solution, hydrate ($\text{CaBr}_2 \cdot 6 \text{H}_2\text{O}$), and CaBr_2 solid correspond to three stable phases. The blue dashed line indicates room temperature where all experiments were performed. The humidity area of the metastable state (supersaturated solution) is defined as the humidity below 16% at room temperature [WEXLER 2010, GMELIN].

All experiments involving solutions of CaBr_2 were carried out in the humidity range from 40% to 65%, as indicated by the blue arrow in Fig. 4.4. For single levitated droplets, such a significant decrease of the environmental humidity results in evaporation of a large fraction of water from the droplets. Consequently, the concentration of CaBr_2 droplets is significantly increased during the levitating time. Further discussions regarding this issue are found in Section 4.2.3.

Zinc bromide (ZnBr_2) has a similar phase diagram as CaBr_2 , as shown in Fig. 4.5. Three stable phases exist: (i) an aqueous solution, (ii) the hydrate $\text{ZnBr}_2 \cdot 2 \text{H}_2\text{O}$, and (iii) solid ZnBr_2 . The blue dashed line in Fig. 4.5 indicates room temperature, where the experiments were performed ($T = 298 \text{ K}$). At room temperature, the critical humidity of ZnBr_2 is found at about $7.8 \pm 0.5\%$. This value is even lower than that of CaBr_2 . Therefore, due to the same reasons outlined above, the experiments studying homogeneous nucleation process of ZnBr_2 solutions have also been performed at higher humidity, as noted by the blue arrow in Fig. 4.5.

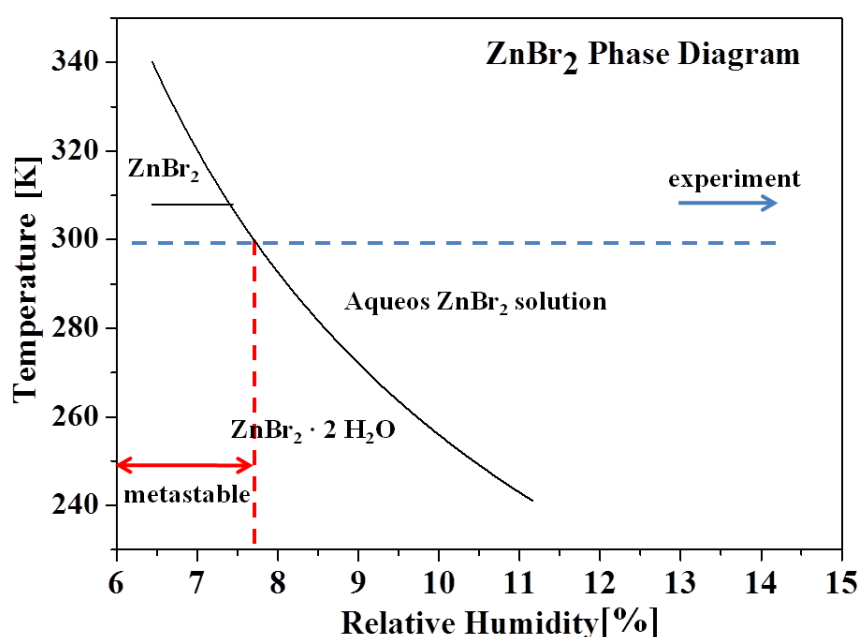


Figure 4.5. Phase diagram of ZnBr_2 as a function of temperature and relative humidity. An aqueous ZnBr_2 solution, the hydrate ($\text{ZnBr}_2 \cdot 2 \text{H}_2\text{O}$), and dry crystals (ZnBr_2) are the stable phases. The blue dashed line indicates room temperature, where the experiments are performed. The humidity regime of metastable supersaturated solutions is found at relative humidities below $7.8\% (\pm 0.5\%)$, as indicated by the dashed red line [WEXLER 2010, GMELIN].

4.2 XANES Studies of Cluster Formation in Homogeneous Nucleation of Single Levitated Microdroplets

One of the main interests of this work is to study homogeneous nucleation in the thermodynamic equilibrium by tracking the evolution of subcritical solute clusters in supersaturated solutions. For this purpose, long observation times are required for

such phase changes of individual droplets. Levitation of single droplets provides the possibility of extending the observation of crystallization times up to several hours by controlling the relative humidity in the droplet surroundings, where the droplets reach a thermodynamic equilibrium with their surroundings. This is due to the avoidance of any contact to a substrate of the levitated droplets which allows one to reach a high degree of saturation before nucleation occurs spontaneously. The experimental setup consists of optically levitated single microdroplets (see Section 3.2) in combination with synchrotron radiation to measure the X-ray absorption near-edge structure (XANES) at a given humidity in the surroundings of the droplets at room temperature. XANES spectra are a powerful and sensitive approach for studying the local electronic structures of the absorbers of interest, such as solvated ions and their local environment. Therefore, any modification of the local structure resulting from cluster formation or growth or critical nuclei can be followed by the observation of spectral changes, such as shifts in near-edge features or the occurrence of EXAFS-structures in the core ionization continua.

Aqueous sample solutions of sodium bromide (NaBr), calcium bromide (CaBr_2), and zinc bromide (ZnBr_2) are used for the experiments. The initial concentration of the sample solutions is chosen to be close to the saturation point, where supersaturation is reached by evaporation of the solvent. It has been demonstrated that the size of droplet significantly shrinks during the first few seconds after levitation, i.e. large amount of water evaporation [HAMZA THESIS]. The solutions of the levitated droplets reach subsequently a thermodynamic equilibrium.

XANES spectra of single levitated droplets of NaBr and CaBr_2 solutions are measured in the energy regimes of the Br K-edge as a function of relative humidity. In addition, droplets of ZnBr_2 solution are also studied in the regime of the Zn K-edge. Since the solute concentration is humidity-dependent, the relative humidity in the trap chamber is decreased in a rate of 1-2% per 10 min. This is of importance to slow down the evolution of cluster formation when the solute concentration increases. Typically, it takes for the clusters under these conditions between 2 and 3 hours to reach the critical size for initializing spontaneous crystallization. In order to follow the entire process of cluster formation and crystal growth before homogeneous nucleation occurs, one can continuously take repeated XANES spectra. Systematic changes in the energy position of the core level absorption edges are expected to be observed

because of the varying changes in cluster formation and their surroundings, which influence efficiently the local electronic structure of the absorbing ions or clusters in solution.

Supersaturated aqueous solutions are an intermediate state between a dilute solution consisting of isolated, hydrated ions and solid crystals. Therefore, XANES spectra of supersaturated droplets are compared with their corresponding thin films containing dilute solutions and solid crystals also taken at ambient conditions. These spectral changes, which are observed mostly as spectral shifts of the absorption-edges, provide valuable information regarding cluster formation, their composition, and their internal structures within the three different states of matter.

In order to assign the experimental XANES spectra taken from different solution systems, a series of first principle calculations are carried out. The combination of experimental and theoretical results turns out to be suitable for understanding the physical processes occurring in supersaturated solutions and explain the concentration dependent changes observed in XANES spectra.

4.2.1 XANES Studies of Aqueous NaBr Solutions and Solid NaBr

Fig. 4.6 shows a series of measurements recorded at Br K-edge, where XANES spectra of supersaturated NaBr solutions together with the dilute thin film solution with concentration of 2.25 mol/L and solid crystal are plotted. As noted in Fig. 4.6, the XANES spectra are using different colors to indicate the specific humidity conditions of each measurement (see inset of Fig. 4.6). For these experiments, the relative humidity is one of the most crucial experimental parameters since it also affects several other parameters directly or indirectly, such as the solute concentration of droplet solutions and the droplet diameter. In optical levitation, the environmental humidity of the levitated droplet (controlled by a moisture-exchanger, see Section 3.2.1) can be varied in a range from 15% to 70%. The measurements on supersaturated droplets are repeated for several times under humidities ranging from 30% to 51%, where the K-absorption edge position occurs in a small energy window of about 2 eV. The humidity conditions at which the XANES spectra were recorded are given in Table 4.1. The Br K-edge of the dilute NaBr solution and that of the solid

appear at nearly the same energy, which is evidently lower than is observed for those of supersaturated solutions.

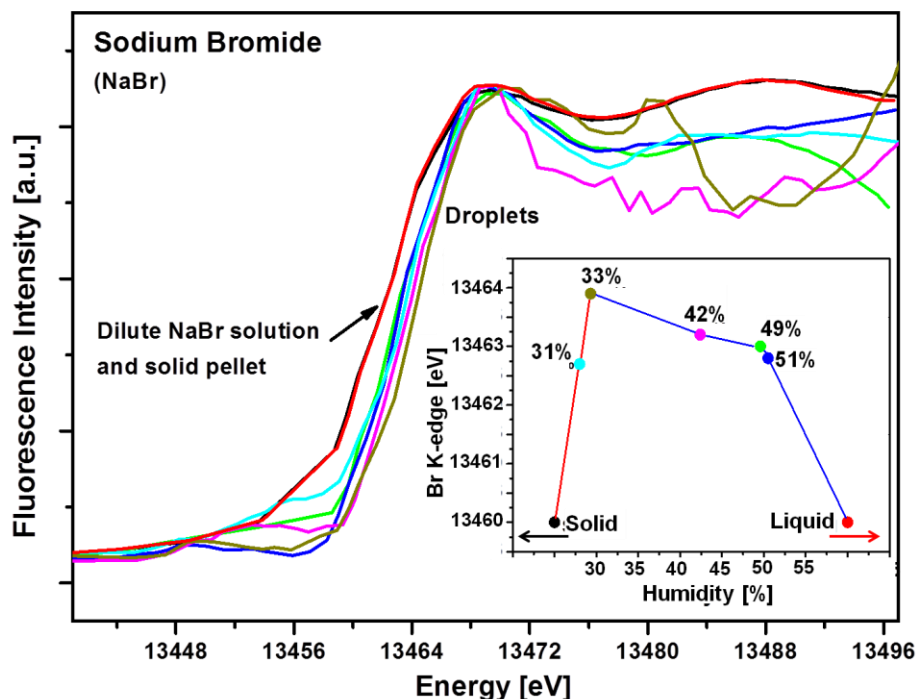


Figure 4.6 (color) XANES spectra in the Br-K-edge regime of single levitated droplets of supersaturated NaBr solutions together with the spectrum of a dilute solution with concentration of 2.75 M (red curve) and a solid pellet (black curve). Each spectrum of different color indicates a measurement at specific humidity condition. The energy positions of the absorption edges are plotted in the inset as function of relative humidity. Each dot in the inset corresponds to a XANES spectrum with the same color, where the K-edge positions are determined. The specific humidity conditions of each color are given in the inset. It is noted that in order to compare the absorption energies of Br K-edges in the solid and liquid states of NaBr, they are positioned at the low humidity regime ($< 30\%$) and high humidity regime ($> 60\%$), respectively, as indicated by the back and the red arrows. See text for further details.

The experimental conditions at room temperature (300 K) are determined according to the phase diagram of NaBr, as shown in Fig. 4.2. The aqueous solution of NaBr becomes supersaturated when the relative humidity in the surroundings of the levitated droplet ranges between 28% and 52%. Within this humidity range, NaBr can form either hydrated or anhydrous solute clusters of variable size by desolvating the initially fully solvated ions. The energy positions of the Br K-edges which are determined by the first derivatives of the edge jump are shown in Table 4.1. Additionally, the absorption energies of Br K-edges are plotted as a function of

relative humidity, as shown in the inset of Fig. 4.6. The results clearly show that with the decrease of *R.H.* (from 51% to 30%), the Br K-edges shift initially to higher energy (blue-shift) and then they move back to lower energy (red-shift). It is evident from these results that the spectral shifts of the K-edge as a function of concentration are small. It is particularly important for these experiments to exclude any possible systematic errors during the measurements. Therefore, repeated measurements have been carried out for more than three times using different levitated droplets containing supersaturated NaBr solution. The resulting spectra of every investigated droplet give the same result of the shift in K-absorption energy as a function of humidity. The error limits for single and repeating studies are determined to be smaller than 0.2 eV.

Table 4.1 Absorption-edge of XANES spectra of single levitated NaBr droplets together with a dilute solution and solid pellet. The dilute solution has concentration of 5.5 M.

Color (in Fig.4.6)	<i>R.H.</i> (%) [$\pm 1\%$]	Saturation Ratio (S)	Br K-edge (eV) [$< \pm 0.2$ eV]
Blue	51	1.22	13462.7
Green	49	1.31	13463.0
Magenta	42	1.47	13463.4
Dark-yellow	33	1.81	13463.9
Cyanogen	31	1.93	13462.7
Red	Liquid	0.77	13459.9
Black	Solid	-----	13459.9

Once a single microdroplet is ejected from the piezo nozzle water molecules start to evaporate from the droplet-air interface in order to adapt to its environment by reaching an equilibrium state with the surroundings, according to their partial water vapor pressure, i.e. relative humidity. This process continues after the droplet is trapped in the focused laser beam. The time period of the droplet required to reach this equilibrium is defined as the *induction time*. It has been found in previous work that the induction time is around 2 to 5 seconds, where the droplet becomes supersaturated [HAMZA THESIS]. This substantial water evaporation during the induction time and the formation of supersaturated solutions within the microdroplet is also observed in this work and is discussed in Section 4.5. In such supersaturated

droplets of electrolyte solutions, both free ions and Bejrrum pairs exist simultaneously [IZMAILOV 1995].

The established equilibrium is changed when the humidity in the levitation chamber is varied. In the described studies the relative humidity of the droplet environment is gradually decreased, which results in further evaporation to reach the equilibrium. Consequently, the droplet size is decreased and the solute concentration is increased. The formation of solute clusters is readily promoted in such highly concentrated solution, since desolvation processes occur. In another word, lower humidity provides an external force for the aggregation of subcritical clusters and promotes the nucleation process. As already described by classical Debye-Hückel theory [RIGBY 1986], screening of electrostatic forces is due to a cloud of oppositely charged counter ions around a given central ion in aqueous solution. This means that the attractive forces between oppositely charged ions involve a multiple interaction between these ions. This may eventually lead to the formation and the evolution of solute clusters in supersaturated solutions. The size of critical clusters for initializing the nucleation process is given in Fig. 4.3. These calculated curves suggest that at the saturation point a NaBr solution requires an infinite number of solute ions to form critical clusters. However, when the solute concentration is close to the efflorescence point of NaBr at room temperature, the critical cluster size decreases to a value of about 2.5 which means about 5 ions are contained in the critical clusters. The small number of ions in critical clusters at high solute concentration is another reason to explain that nucleation occurs readily at high solute concentration. The local electronic structure of the excited atom is progressively modified with the growth of subcritical clusters and these modifications can be determined by energy shift of the absorption edge in XANES spectra. XANES spectra of both dilute solutions and solid pellets of NaBr are also shown in Fig. 4.6, and the Br K-edges of these phases are observed at the same energy position (1459.9 eV).

To achieve a deeper understanding for the energy shifts occurring at the Br absorption edge, further modeling of the experimental EXANES spectra is needed. Therefore, we have employed DFT-simulations in order to model the local electronic structure of the studied system, as will be described in the following Section.

4.2.2 Theoretical Simulation of the Br K-edge in NaBr Nanoclusters

First-principle simulations are carried out using DFT calculations and supercell periodic models which are provided within the Cambridge Serial Total Energy Package (CASTEP) code [CLARK 2005, ACCELRYN 2008]. The Perdew-Burke-Ernzerhof (PBE) exchange-correlation functional [PERDEW 1996, PERDEW 1997] is used and the inner shell electrons are replaced by Vanderbilt ultrasoft pseudopotentials [VANDERBILT 1990]. It is expanded in a basis set of plane-waves up to a cutoff energy of 450 eV together with a Monkhorst-Pack [MONKHORST 1976] grid with $1 \times 1 \times 1$ k-point sampling. In order to obtain the initial geometries of the systems of interest, we performed molecular dynamic (MD) simulations (250 ps at ~ 300 K within the canonical ensemble, NVT) using empirical potentials. The final structures obtained in these MD simulations are then reoptimized with the current computational setup depicted above. The MD simulations are carried out with the broadly used GROMACS (GRoningen MAchine for Chemical Simulations) software [HESS 2008] using the optimized potential for liquid simulation (OPLS) [JORGENSEN 1996, KAMINSKI 2001] force field together with the standard TIP3P (Transferable Intermolecular Potential 3P) for water [JORGENSEN 1983].

The solute models considered consist of non-stoichiometric cubic Na_nBr_m clusters embedded in 58 H_2O molecules in a cubic supercell of 14 Å edge length. The five atomic configurations with the lowest total energy along the empirical molecular dynamic simulation are selected for subsequent DFT reoptimization with a loose convergence threshold of 0.1 eV/Å. This procedure allows us to evaluate different Na_nBr_m clusters solvated by water and average them statistically in order to derive a realistic comparison with the experimental results. Two different cubic sodium bromide nanoclusters are considered (see insets in Fig. 4.7): $\text{Na}_{13}\text{Br}_{14}$ (centered around a Na atom) and $\text{Na}_{14}\text{Br}_{13}$ (centered around a Br atom). When using supercell models, the artificial periodic repetition of charged supercells needs to be compensated, to avoid spurious electrostatic interactions and, therefore, a divergent Coulomb energy. In CASTEP charged supercells are made charge neutral by the addition of a compensating background charge. The $\text{Na}_{13}\text{Br}_{14}$ clusters contain two different types of Br atoms in terms of Na-coordination: 8 *corner* sites (Br_{3c}) and 6 *face* sites (Br_{5c}). The $\text{Na}_{14}\text{Br}_{13}$ clusters contain two other types of Na-coordinated Br atoms: 12 *edge* sites (Br_{4c}) and 1 *bulk* site (Br_{6c}). For each of these types of

nanoclusters we carried out five independent DFT geometries reoptimized calculations starting from the empirical molecular dynamics simulation procedure outlined above. This corresponds to a total of ten different optimized nanocluster geometries containing solvated clusters. Therefore, a total number of 135 Na-coordinated Br sites: 40 Br_{3c}, 60 Br_{4c}, 30 Br_{5c}, and 5 Br_{6c} are obtained from these calculations. Moreover, each of these sites possesses different degrees of water solvation [C1] offering further opportunities of analysis, as will be discussed below.

In EELS (Electron Energy Loss Spectroscopy) and XANES spectroscopy, the spectral shapes are given by the Fermi golden rule. The core electron is excited to an unoccupied, empty state, where at the edge the lowest empty state (allowed by the selection rules) is reached. As such, both techniques essentially probe the empty density of states in the presence of the core hole. EELS also follows dipole selection rules, if only a small angle of forward scattered electrons is detected [HITCHCOCK 1977]. Therefore, it is in general assumed that the spectral shape of XANES and EELS is identical [STAVITSKI 2010]. Since the electronic excitation and relaxation times are expected to be significantly shorter than the atomic relaxation time, we keep the full-core optimized geometries frozen in order to carry out the corresponding core-hole EELS calculations, as implemented in the CASTEP program [PICKARD 1997, PICKARD THESIS, REZ 1999]. We do this by generating an on-the-fly core-excited pseudopotential for one Br atom within a nanocluster, whilst maintaining the rest of atoms in the cluster with fully occupied core levels. We repeat this procedure for all different 135 Br sites. The Br core-hole is created by completely removing the excited electron (full core-hole approximation [HETÉNYI 2004]) from the Br *1s* orbital (K-shell) in the pseudopotential, i.e. we generate a new pseudopotential specifically constructed to describe a *K*-shell hole in a Br atom within the specific chemical environment of the nanocluster [PICKARD, PHD THESIS, C2]. The final core-excited XANES spectrum associated to each Br site is then rescaled relative to the Fermi level. Rescaling relative to the vacuum level is not possible, since such level cannot be calculated in the periodic boundary conditions applied in the calculations: The unit cell is formed by a NaBr nanocluster and water molecules and, therefore, the total local potential cannot be evaluated in a vacuum region where the potential becomes constant (region sufficiently far away from any atom).

The structural models considered here allow us to study four distinctly different Na-coordinated Br_{nc} sites ($n = 3, 4, 5$, and 6). Sites $\text{Br}_{6\text{c}}$ and $\text{Br}_{4\text{c}}$ ($\text{Br}_{5\text{c}}$ and $\text{Br}_{3\text{c}}$) are computed using the $\text{Na}_{14}\text{Br}_{13}$ ($\text{Na}_{13}\text{Br}_{14}$) nanocluster (insets in Fig. 4.7). Additionally, we can explicitly account for solvation effects due to the different number of water molecules forming a water network with hydrogen bonds with a given Br_{nc} surface site, which acts as an acceptor. This is suitably described by the molecular dynamic treatment employed here to generate atomic configurations of each solvated nanocluster, since for a given snapshot each Br_{nc} site is indeed forming a different number of hydrogen bonds with surrounding water molecules. The calculations indicate that $\text{Br}_{3\text{c}}$ sites are able to form up to three hydrogen bonds with close lying water molecules, $\text{Br}_{4\text{c}}$ form up to two hydrogen bonds, and $\text{Br}_{5\text{c}}$ can form up to one hydrogen bond. Finally, $\text{Br}_{6\text{c}}$ sites are fully Na-coordinated and, therefore, they cannot form hydrogen bonds with surrounding water molecules.

In Fig. 4.7 we summarize the calculated EELS spectra corresponding to all four distinct Br_{nc} sites showing a different degree of solvation. The analysis of these data points out two important factors affecting the K-edge energy of a specific Br_{nc} site: (i) the number of hydrogen bonds formed with surrounding water molecules, and (ii) the coordination with sodium sites. Regarding (i), we notice that a gradual shift to lower energy of the Br K-edge occurs when increasing the number of hydrogen bonds for any given Br_{nc} site. The absorption edges of different Br_{nc} sites in the two simulated models are summarized in Table 4.2. This energy shift indicates that highly solvated sites result in lower Br K-edge energies than poorly solvated ones. Therefore, the formation of hydrogen bonds with the solvent has a substantial effect on the corresponding XANES spectra. For example, in the case of $\text{Br}_{3\text{c}}$ sites, a total energy shift of ~ 0.8 eV [C3] is predicted from the model calculations when going from a fully water solvated site to one without any hydrogen bond. Similar observations are made when increasing the coordination with sodium sites. Regarding (ii): This point becomes most important when one focuses on Br_{nc} sites showing no H-bonds. Nevertheless, when comparing fully coordinated sites ($\text{Br}_{6\text{c}}$, $\text{Br}_{5\text{c}} + 1\text{H}_2\text{O}$, $\text{Br}_{4\text{c}} + 2\text{H}_2\text{O}$, and $\text{Br}_{3\text{c}} + 3\text{H}_2\text{O}$) the energy shifts between these sites become rather small (0.2 eV). Overall, these results show that the increase of the coordination of Br sites, either by means of Na atoms within the nanocluster or by water molecules from the solvent, changes the energy position of the K-edge shift to lower energies,

corresponding to a spectral red-shift. The maximum range of these energy shifts is found for NaBr-clusters to be rather narrow and ranges up to 0.8 eV.

Table 4.2 Br K-edges of simulated XANES spectra given in Fig. 4.7. The energy position corresponding to each Br_{nc} site is determined by the maxima intensity of the first derivative of each spectrum.

Br_{nc} Sites	Simulated K-edge	Br_{nc} Sites	Simulated K-edge
$\text{Br}_{6\text{c}}$	2.52	$\text{Br}_{5\text{c}} + 1\text{H}_2\text{O}$	1.30
$\text{Br}_{4\text{c}} + 0\text{H}_2\text{O}$	3.01	$\text{Br}_{3\text{c}} + 0\text{H}_2\text{O}$	1.22
$\text{Br}_{4\text{c}} + 1\text{H}_2\text{O}$	2.83	$\text{Br}_{3\text{c}} + 1\text{H}_2\text{O}$	1.04
$\text{Br}_{4\text{c}} + 2\text{H}_2\text{O}$	2.67	$\text{Br}_{3\text{c}} + 2\text{H}_2\text{O}$	0.97
$\text{Br}_{5\text{c}} + 0\text{H}_2\text{O}$	1.43	$\text{Br}_{3\text{c}} + 3\text{H}_2\text{O}$	0.80

This conclusion of the theoretical simulations provides an explanation for the blue- and red-shift of the Br K-edge which is experimentally observed in supersaturated NaBr droplets, where low absorption energies are observed in dilute solutions and for solids. We assume that in the supersaturated solution the subcritical NaBr clusters present a higher concentration of low-Na-coordinated Br_{nc} sites ($n < 6$) than occurs in large solid particles, where $n = 6$ occurs. Thus, the maximum $(6-n)$ number of water molecules from the solvent will form hydrogen bonds to the not fully coordinated Br sites. Then, with increasing NaBr concentration, the number of hydrogen bonds decreases. The nucleation process is experimentally followed by tracking the Br K-edge energy shifts associated to differently coordinated Br_{nc} sites. Nevertheless, according to the simulated near-edge spectra, one should expect to observe a minor shift of the Br K-edge of 0.0-0.2 eV when monitoring the nucleation process. This is due to the fact that water solvation gives a similar energy shift of the Br K-edge and screens those Br_{nc} sites, which have low-Na-coordination. This leads to the result that near-edge spectra are not fully sensitive to the various superimposed processes contributing to spectral shifts. However, it is important to note that due to the thermal dynamics under ambient conditions the average degree of solvation of NaBr clusters does not probably reach its maximum, since the number of water molecules forming a hydrogen bond with a given Br_{nc} site is expected to be on the average somehow lower than $6-n$. Therefore, experiments should be sensitive to detect small spectral red-shifts at Br K-edge with increasing size of the NaBr clusters.

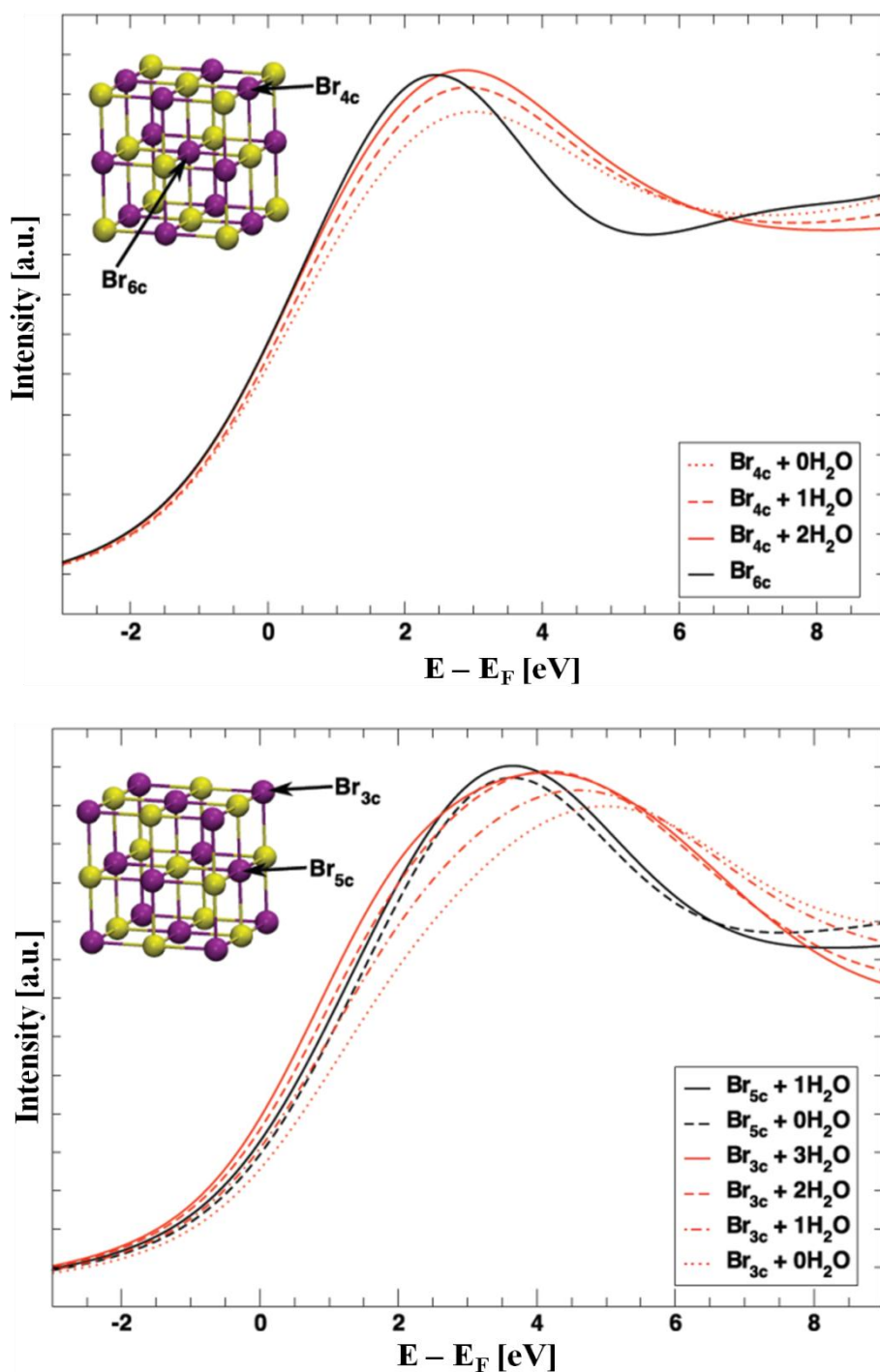


Figure 4.7 Simulated XEANS spectra showing the Br K-edge for Na₁₄Br₁₃ (top) and Na₁₃Br₁₄ (bottom) nanoclusters. Different Na-coordinated Br sites are considered (see insets) as well as different number of water molecules (not shown) forming hydrogen bonds with the indicated bromine atoms. Each XANES spectrum corresponds to the average spectra of equivalent bromine sites and degrees of solvation, as discussed in the text. The insets depict idealized representations of the solvated nanoclusters after geometry optimization. Purple (yellow) spheres correspond to Br (Na) atoms.

Unlike supersaturated solution droplets, in dilute NaBr solutions and solid crystals any given Br_{nc} site is fully coordinated with either water or sodium atoms. According to the model calculations discussed above, this maximum coordination corresponds to the minimum energy of the system.

4.2.3 XANES Studies of CaBr₂ and its Dilute Solution and Solids

Similar measurements to those on NaBr solutions were also carried out on saturated droplets of CaBr₂, its dilute solution, and solids crystals. According to the calculated phase diagram of CaBr₂ shown in Fig. 4.4, the efflorescence point of CaBr₂ at room temperature is below 15% relative humidity. Unfortunately, due to the experimental limitations of the setup, such humidity conditions cannot be reached. Therefore, studies at such low relative humidity are not possible. However, XANES spectra of CaBr₂ were taken in the relative humidity range of 40-64%, which is considerably higher than the efflorescence point (as indicated by a blue arrow in Fig. 4.4). According to the phase diagram is evident that CaBr₂ solutions remain liquid in the accessible humidity regime at ambient conditions. However, this does not imply that such levitated droplets will always stay in the liquid state and crystallization will never occur. This is because heterogeneous nucleation might occur if a suitable crystallization germ is present. Further, according to the classical nucleation theory, homogeneous nucleation is based on the formation of critical clusters through stochastic interactions between solvated ions [VOLMER 1939, BECKER 1935], and therefore, the probability of forming critical clusters in aqueous solution increases with time, and such aqueous droplets might eventually crystallize [NA H.-S., 1994].

Fig. 4.8 shows the Br K-edge XANES spectra of supersaturated CaBr₂ droplets recorded for several relative humidities in the levitation chamber. The corresponding relative humidity at which each near-edge spectrum was taken is indicated next to the spectrum and the energy position of the corresponding absorption edge is given in Table 4.3. The experimental Br K-edges are spread in an energy regime of about 5 eV and appear to have a progressive red-shift when the humidity is decreased from 63.3% to 41%. This spectral shift of Br K-edge to lower energy is quite different from what is observed for NaBr solutions, where a blue- and a red-shift are observed (see Section 4.2.1). This difference between NaBr and CaBr₂ is not surprising taking into

account that CaBr_2 clusters have fluorite-like (Br^- 4-coordinated, tetrahedral) structure, whilst NaBr ones are rock-salt-like (Br^- 6-coordinated, octahedral), and, therefore, the local electronic structure of Br^- is different in these two systems. Moreover, the charge-to-radius ratio of Ca^{2+} (1.6×10^{-2} e/pm) and Na^+ (8.6×10^{-3} e/pm) is different, which plays an important role in the formation of solute clusters [FULTON 2006], and as a result, this can also influence the electronic structure and local environments of Br^- differently in CaBr_2 and NaBr .

Besides the Br K-edges, the other information given in Fig. 4.8 is the first EXAFS wiggle above the absorption edges. With decreasing the relative humidity, the first wiggle of each XANES spectra shifts to higher energy. Similar as the shape resonance, wiggles occurring at higher energy correspond to a shorter distance from the absorbing atoms to their neighbors (see Section 2.6) [STÖHR 1992, STÖHR 1984]. Thus the spectral blue-shift of the K-edge provides strong evidence for the aggregation of solute ions in the supersaturated droplet of CaBr_2 when $R.H.$ decreases.

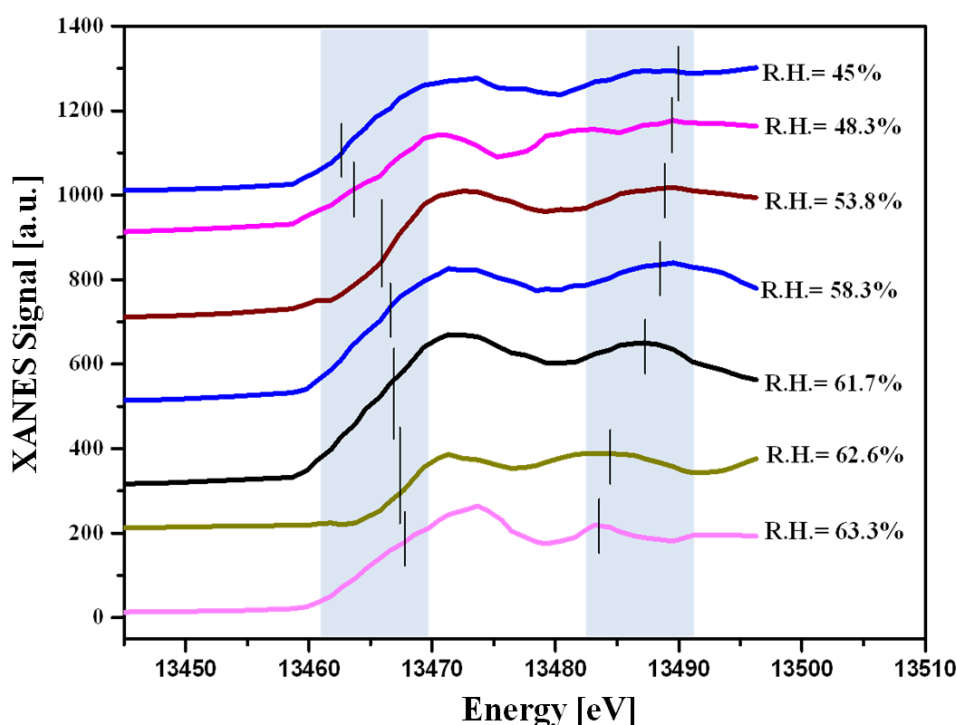


Figure 4.8 Experimental XANES spectra of supersaturated CaBr_2 droplets at different humidities. Each spectrum was taken at a specific humidity condition. Br K-edge shifts to lower energy when relative humidity decreases. In contrast, the first wiggle above the absorption edge occurs at higher energy at lower relative humidity.

Table 4.3 Absorption-edges of XANES spectra of single levitated droplets of supersaturated CaBr₂ solutions.

<i>R. H. (%)</i>	Saturation Ratio (S)	Br K-edge (eV)
63.3	1.0	13467.8
62.6	1.07	13467.4
61.7	1.16	13466.9
58.3	1.45	13466.7
53.8	1.75	13466.0
48.3	1.86	13463.5
45.0	2.0	13462.6

The essential information given in Fig. 4.8 is that with a decrease in relative humidity, bromide ions are getting closer to their surrounding neighbors and as a consequence, the electronic structure near the Br⁻ is systematically modified and the energy of the K-edge constantly shifts to lower energy, corresponding to a spectral red-shift. Based on these findings, XANES spectra of dilute CaBr₂ solutions with concentration of 5.4 M and solid crystals are taken under ambient conditions for a comparison. As shown in Fig. 4.9, these two spectra are located at different absorption energy compared to that of the supersaturated droplets (indicated as ‘droplet’ in Fig. 4.9), i.e. the spectrum of dilute solutions with initial concentration of 2.7 mol/L (indicated as ‘liquid film’ in Fig. 4.9) appears at higher energy whereas the near-edge spectrum of a solid pellet appears at lower energy. The exact values of the absorption edges of these three spectra are 13468.2 eV, 13464.5 eV and 13461.7 eV, respectively from the liquid dilute film to the solid pellet. The error limit of these energy values is estimated to be ± 0.2 eV. This result is quite straightforward, since the Br K-edge shifts as a function of solute concentration to lower energy, when the aqueous droplet transfers from a dilute to a supersaturated solution on the way to crystal formation via homogeneous nucleation.

Concentrated aqueous solutions of calcium halides (CaCl₂ or CaBr₂) with solute concentration up to 5.6 M have been investigated in previous works by means of X-ray diffraction, Extended X-ray Absorption Fine Structure (EXAFS) and XANES [GASPAR 2004, FULTON 2003]. It was demonstrated that either solvent-shared ion pairs (e.g. Ca²⁺-OH₂-Cl⁻) or contact ion pairs (e.g. Ca²⁺-Cl⁻) were formed with an

increase of solute concentration. However, these works mostly focused on the solvation structures of Ca^{2+} . Therefore, a specific discussion regarding CaBr_2 will be based on theoretical calculations simulating the energy shifts near Br K-edge. These calculations have been carried out by using the CPMD code (see Section 2.8.2). It is based on the approach that was developed within the STOBEDEMON code [HERMANN 2002]. More details are described in the following Section.

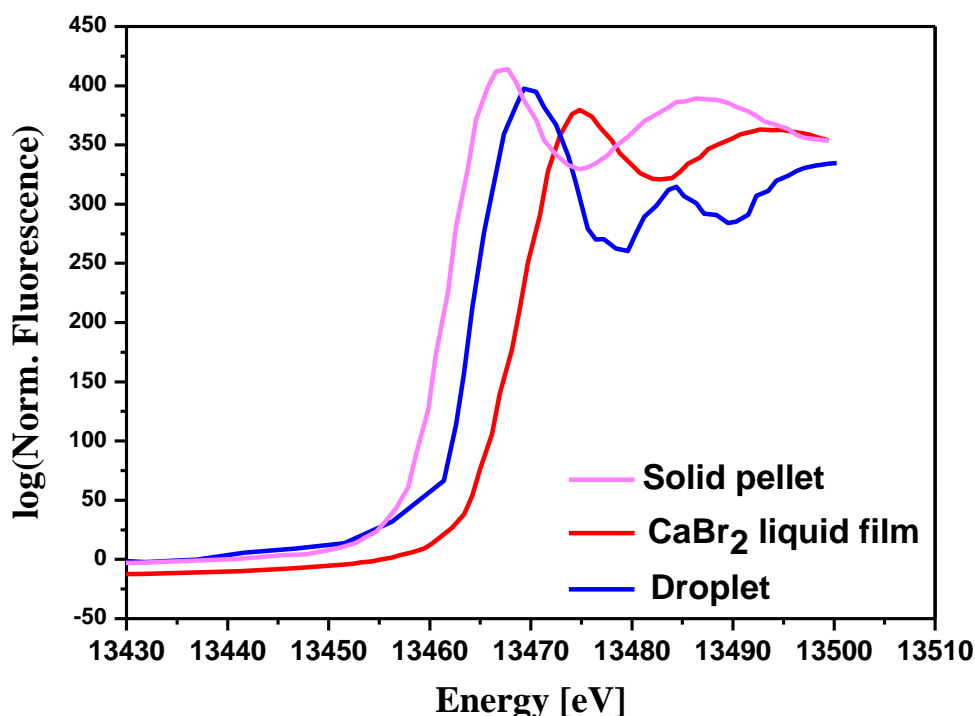


Figure 4.9 (color) Experimental XANES spectra of single levitated droplets of supersaturated CaBr_2 solutions under relative humidity of 56% together with its dilute thin film solution ($c = 5.4 \text{ M}$) and a solid pellet.

4.2.4 Simulations of diluted and supersaturated CaBr_2 solutions

The constant shift of the Br K-edge in CaBr_2 to lower energy with increasing solute concentration is assigned by performing theoretical DFT simulations. Two model structures, i.e. single Br^- ions surrounded by water and a molecular CaBr_2 ion pair (Bjerrum pair) in aqueous solution (Fig. 4.10) are considered. These molecular dynamics simulations made use of the Car-Parinello molecular dynamics (CPMD) formalism, which is implemented in the STOBEDEMON code [HERMANN 2002].

The method used for these spectral simulations follows the approach which was introduced by Cavalleri and coworkers [CAVALLERI 2004].

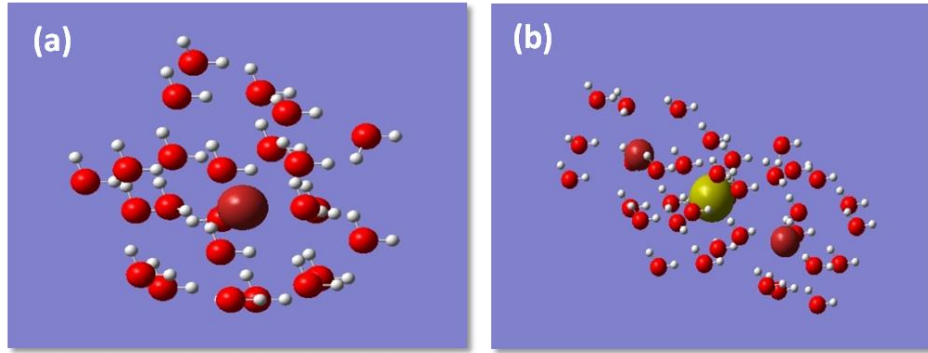


Figure 4.10. Two model structures are considered for the spectral simulations of the XANES spectra of Br^- in CaBr_2 solutions: (a) corresponds to a single Br^- surrounded by water; and (b) represents a monomer ion-pair of CaBr_2 surrounded by water. The yellow sphere corresponds to Ca^{2+} and large red spheres correspond to Br^- . Water is indicated by small red spheres bonded with white spheres.

The intensities I_{if} of the simulated core spectra corresponding to oscillator strengths in X-ray absorption is expressed by the transition moment between the initial and final state, which is separated by the energy difference $\hbar\omega_{if}$:

$$I_{if} = \frac{2}{3} \hbar\omega_{if} |\langle \Phi_i | \mu | \Phi_f \rangle|^2 \quad (4.7)$$

where $\hbar\omega$ is the energy difference between initial and final states, μ is the dipole moment, Φ_i and Φ_f are the wave functions of the initial and the final states, respectively.

The simulations of XANES spectra require the determination of a series of energy levels and their corresponding oscillating strengths. According to the initial and final state rules [NILSSON 1995, U. VON BARTH 1982, GREBENNIKOV 1997], the shape of a XANES spectrum is given by the eigenstates of the final state Hamiltonian including the core-hole. However, the total transition intensities are determined by the number of accessible unoccupied levels in the initial state before the X-ray transition occurs. As graphically presented in Fig. 2.6, the core-hole created during the X-ray absorption localizes on one atomic site, therefore, the XANES spectrum is determined by the

local density of states (DoS) of unoccupied levels of a selected atom before core level excitation, which can be calculated by DFT. In this way, the absorption process can be suitably reduced to a one-particle model.

Standard CPMD simulations only calculate the evolution of the occupied Kohn-Sham states. However, because it is necessary for the simulation of XANES spectra to determine the levels of unoccupied states, Cavalleri et al. suggested to perform firstly a wave function optimization of the occupied orbitals with the ODIIS method [HUTTER 1994]. Then, with the generated Kohn-Sham potential for a subsequent Lanczos diagonalization [FILIPPONE 2001] one can calculate a certain number of unoccupied states. Finally, the matrix elements in Eq. 4.7 are calculated, where the Slater exponent for the final state wave function ϕ_f can be modulated in order to get the best agreement with the experimental results.

The key point of performing theoretical modeling of XANES spectra is to determine the core-hole effects, which means to find the correct balance between the initial and the final state effects. The entire spectrum, including valence, Rydberg, and continuum excitations, can be obtained from application of the Z+1 approximation [STÖHR 1992, SCHWARZ 1975] or the transition-potential approach [TRIGUERO 1998] of DFT, where both the initial and final states are taken from the same wavefunction. In this work, the Z+1 approximation, also known as the full core-hole (FCH) approximation, is applied for the simulation of XANES spectra of solvated species originating from calcium bromide. Basically, in this approach one can use the pseudopotential generated for a given electronic structure containing a fractionally occupied core orbital $1s^1$ or simply using the pseudopotential of the element next to the excited atom (Z+1) in the periodic table [TRIGUERO 1998, TANAKA 1999, HETENYI 2004, TAILLEFUMIER 2002]. We used the program FHI98PP (Fritz-Haber-Institute) to generate the pseudopotentials for both excited and non-excited bromine atoms [FUCHS 1999]. It should be noted that the FCH wavefunction put more emphasis on the final state, so that this approximation produces suitable agreement with the experimental results for those systems in which the final state effects are dominant. This has been shown, for example, in the case of the C K-edge spectrum of fullerenes [NYBERG 1999].

Final calculated curve involving the theoretical scheme given in Eq. 4.7 has explicitly computed transitions placed on each absolute energy scale. In order to make a direct

comparison with experimental data, the computed XANES spectra have to be continued from making association of program output of discrete set of energy levels with a certain oscillator strength and line broadening [CAVALLIERI, 2004]. Such line widths can be simulated in the most simple way by convolving each line in the CPMD output with a Gaussian of the appropriate full width at half maximum (FWHM). Based on the best fit considerations we take on average 5 eV FWHM of Gaussian broadening for energies below the edge and then added about 0.1 eV to this value for each electron volt above the edge. A similar scheme has been used in previous works, for example, in modeling the XANES spectra of water [CAVALLIERI, 2004 AND PH.D THESIS].

The resulting modeled spectra are given in Fig. 4.11 together with experimental results for a comparison. The energy shift (about 3.5 eV) between Br K-edges of single Br^- fully solvated by water and CaBr_2 solvated by water yields almost exactly the same energy difference that has been observed for the experimental spectra of a dilute thin film solution with concentration of 5.4 M and a supersaturated droplet with concentration about 10 M. It is important to point out that the spectral simulations of the two model structures are only used to reproduce the energy positions of the absorption edges, where the shape above the edge is not considered. Such agreement between the model simulations and the experimental results strongly demonstrates that in dilute solutions solvated Br^- is dominant, as expected. However, with the increase of solute concentration, CaBr_2 (aq) ion pairs, or so called “Bjerrum pairs”, which can be considered to be electrically neutral [IZMAILOV 1995] are formed in the supersaturation regime.

Single levitated droplets with concentration of 5.4 M are initially injected into an environment with a relative humidity of 65%. As mentioned above, after injection of the droplet it needs first to reach an equilibrium with the ambient environment by evaporating water into the environment in the trap chamber. From the phase diagram of CaBr_2 it is known that at room temperature a CaBr_2 solution tends to stay liquid at 65% relative humidity. This means the levitated droplet is initially located in the part of the Köhler curve where $D_p > D_{pc}$ (see Fig. 2.2). It is known that in this regime the vapor pressure over droplet surface is an increasing function of droplet diameter. Therefore, when the experimental humidity condition starts to decrease from 65% to 40% during the measurements of XANES spectra, accompanied by an increase in

solute concentration, CaBr_2 droplets move along the Köhler curve in the direction of smaller diameter size. Since the sample solution of CaBr_2 ($M = 5.4 \text{ mol/L}$) is prepared close to the saturation point ($M = 7.1 \text{ mol/L}$), it is not difficult for the droplet solution to become supersaturated, which requires only a minor evaporation of the solvent, corresponding to a slight decrease in droplet diameter. The supersaturated solution is a metastable system which is characterized by the appearance of subcritical solute clusters [IZMAILOV 1995] which are formed by aggregation of Bjerrum pairs undergoing permanent association-dissociation processes with solvated ions in solution. The experimental results show strong evidence that with the aggregation of Bjerrum pair leads in the regime of core-level excitation near the Br-K-edge to a spectral red-shift. This means that the electronic structure of the aggregating species is gently modified as a result of formation of subcritical clusters, where their size varies depending on the conditions of the ambient atmosphere.

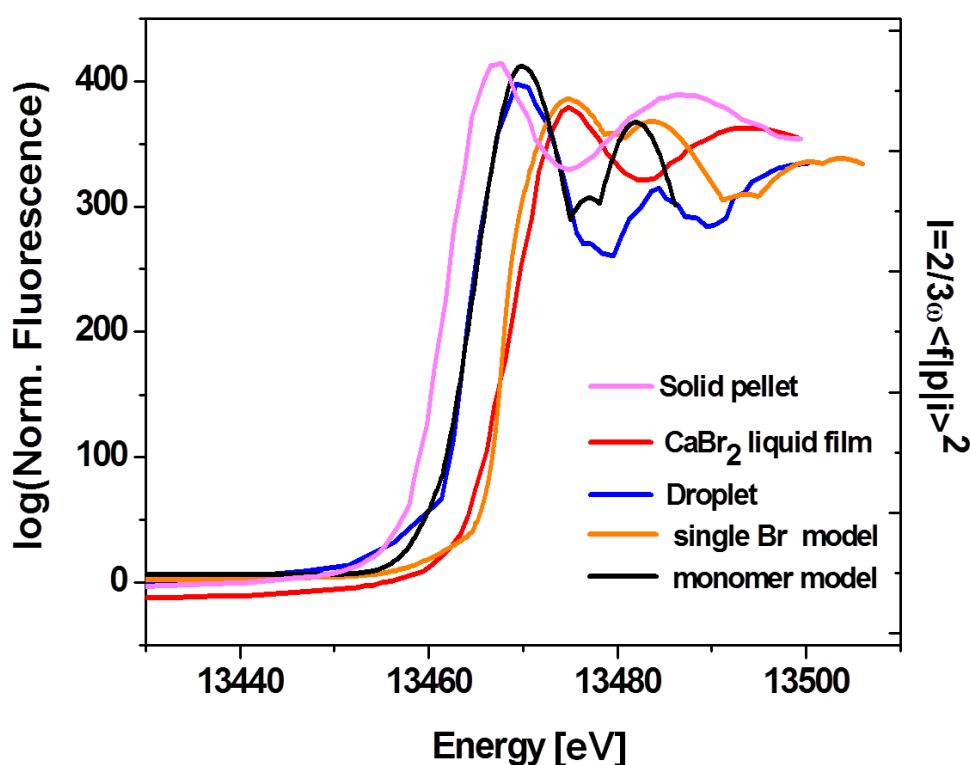


Figure 4.11 (color) Comparison between calculated XANES spectra of two model structures with the experimental curves taken from the dilute thin film solution of CaBr_2 with concentration of 5.4 M and supersaturated droplets with concentration about 10 M.

It is worthwhile to mention that, since the formation of solute clusters is based on the interactions between solvated ions which increase with solute concentration and more concentrated solution requires smaller size of critical clusters, the probability of forming critical clusters to initialize homogeneous nucleation in supersaturated solution increases with time. Since typically the experiments last for several hours, crystallization in supersaturated droplets of CaBr_2 solution might even happen at relative humidities above the efflorescence point. For example, in this work nucleation occurs at humidity about 41% which is by 24% higher than the efflorescence point. However, heterogeneous nucleation cannot be fully excluded.

Due to the thermal conditions there are innumerable solution structures formed before crystallization. But, of course, we are not able to model all these possible structures, which do not allow us to derive an ensemble average of species occurring in the liquid droplet. Instead of that, we can use suitable model structures to gain a qualitative insight into the changes in electronic structure giving rise to spectral shifts and to explore trends in systematic changes in the surroundings of the absorbing solute species. Therefore, for this purpose, we only simulate one spectrum which corresponds to a supersaturated droplet, as shown in Fig. 4.11. The absorption edge of this spectrum corresponds to the average value of all possible spectra occurring in such CaBr_2 droplets (Fig. 4.8). Note that the structures within the solution droplet are time-dependent due to fluctuations, so that the near-edge spectra could be different from each other. In summary, Fig. 4.11 provides clear evidence that high solute concentration corresponds to a red-shifted edge position at the Br-K-edge. Further, the spectral shifts which are fully reproduced by model calculations provide evidence for the formation of Bjerrum pairs in supersaturated solution droplets.

4.2.5 XANES Studies of ZnBr_2 Droplets and its Dilute Solution and the Solid

For highly concentrated solutions of NaBr and CaBr_2 , we only focused on the electronic structure of the anion (Br^-) in order to study the evolution of subcritical clusters. In this Section, we focus our attention on Zn^{2+} cations.

Among all the sample solutions prepared in this work (see Section 3.8), ZnBr_2 is the only suitable solution for performing studies of cations. This is due to the energy position of the Zn K-edge, which is in the energy range of the hard X-ray

monochromator used in this work (experimental details see Section 3.2). Furthermore, ZnBr_2 has a relatively low solubility in water at room temperature (1.98 M). Thus, the XANES spectrum taken at the Br K-edge has a low intensity, which is due to the low concentration of Br^- in the solution. In contrast, the spectra taken at Zn K-edge show a considerably higher intensity. There are several reasons for this finding: (i) the atomic absorption cross section of Zn (10^6 barn / atom) is significantly higher than that of Br (10^5 barn / atom) [SALOMAN 1988]; (ii) the Zn K-edge (9.6 keV) occurs in the center of the energy range (5–14 keV) of the monochromatic X-ray beamline (KMC-2), where the photon flux of the storage ring decreases with increasing energy. This implies that the photon flux is higher at the Zn K-edge than at the Br K-edge (photon flux at energy of Zn K-edge: $8 \cdot 10^9$ photons/s and Br K-edge: 10^9 photons/s).

We compare the Zn K-edges, as observed in XANES spectra of CaBr_2 , from a dilute solution (thin film), supersaturated droplets, to a solid ZnBr_2 pellet. As shown in Fig. 4.12, the experimental results are quite similar to the results obtained from CaBr_2 : The Zn K-edge of the dilute solution is observed at the highest energy, whereas that of solid crystals shows the lowest absorption energy. XANES spectra taken from levitated droplets are observed between these bracketing conditions of the dilute solution and solid crystals. The energy shift of Zn K-edges between supersaturated droplets and the dilute solution is of the order of 4 eV, whereas the shift between the droplets and solid crystals is about 3 eV (see Fig. 4.12).

These energy shifts at the Zn K-edge are rationalized in the same way as has been outlined above for CaBr_2 . This demonstrates that with the increase in ZnBr_2 concentration the core electron absorption of Zn^{2+} shifts to lower energy. This provides convincing evidence that ion pairs or Bjerrum pairs are also formed in supersaturated aqueous droplets of ZnBr_2 with a solute concentration of 2.0 M.

The consistent results obtained from the solutions of CaBr_2 and ZnBr_2 reveal information that the electronic structures of both cations and anions in highly concentrated electrolyte solutions shift to lower energy during the nucleation process from the liquid to the solid state. Specifically, since the absorption energy in solid crystals is lower than that in liquid, one expects that there will be a systematic red-shift of the absorption energy with increasing concentration of the supersaturated solution. This expectation is in full accordance with the experimental results shown in Fig. 4.8.

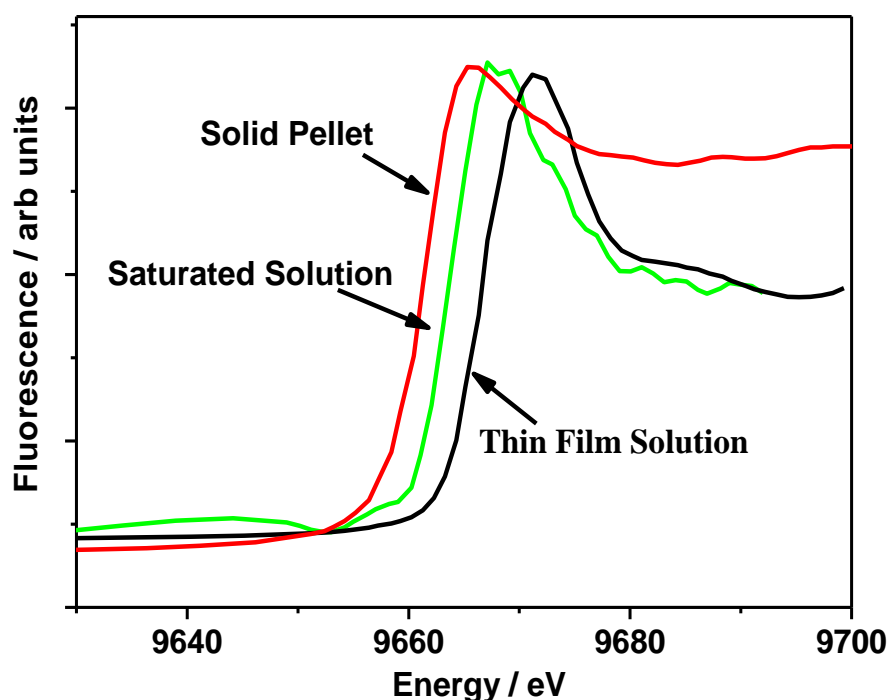


Figure 4.12 (color) XANES spectra of single levitated droplets (green) of supersaturated ZnBr_2 solutions with concentration of 2.0 M together with the XANES spectra of a thin film of a dilute solution (black) with concentration of 1.7 M and a solid pellet (red) recorded at the Zn K-edge.

4.3 Near-Edge Structure of Supersaturated KBr Droplets

Potassium bromide (KBr) is another sample solution which was studied by XANES spectra at the Br K-edge. Droplets of KBr solution were injected into the optical trap at a relative humidity around 60% which is close to its efflorescence point (55%-57%) at room temperature. Therefore, droplets containing KBr solution were used to study the internal structures of solutions immediately before and after crystallization. The phase transition from the liquid to the solid can be observed directly from the change of the scattering patterns of the levitated droplets.

Experimental curves recorded at the Br K-edge for single levitated KBr droplets are indicated by the red solid lines in Fig. 4.13. A prominent difference between the spectra of the pre- and post-crystallization is a spectral shoulder, which only occurs after crystallization. This feature occurs at 13463 eV. It is attributed to the $1s \rightarrow 4p$ transition, according to previous work [HEALD 1978, CHEN 2005]. It is suggested that this band can be assigned in solution to the formation of both direct contact and

solvent-shared ion pairs [FULTON 2003], as confirmed in present work. According to the present work on related solutions (NaBr, CaBr₂, and ZnBr₂), it demonstrated that Bjerrum pairs or even solute clusters are formed when aqueous droplets are trapped under humidity conditions which are close to the corresponding efflorescence point. Therefore, we assume that the occurrence of the spectral shoulder in Fig. 4.13 also results from the formation of KBr ion pairs in levitated droplets.

In order to demonstrate the validity of this assumption and to have more profound assignment for the formation of such a special feature, we performed model simulations using the Finite-Difference Method Near-Edge Structure (FDMNES) program. FDMNES [JOLY 2001] is a program that is used to calculate different kinds of spectra related to X-ray absorption. It also provides the absorption cross section of photons near the ionization edge, corresponding to XANES spectra. Within this code, it is applying the Finite-Difference Method (FDM) which solves the Schrödinger equation by using the local density approximation [KIMBALL 1934].

Three model structures are considered, as shown in Fig. 4.13: (i) the monomer ion-pair KBr surrounded by water, (ii) hydrated solute clusters, and (iii) anhydrous solute clusters in solution are considered (see Fig. 4.13 a-c). The calculated spectra are given as black solid curves in Fig. 4.13. We note that pure solid crystals have an irregular shape. Therefore, it is almost impossible to levitate such species in an optical trap. This implies that no XANES spectra of pure solid microparticles were recorded by the levitation approach. There is agreement between the modeled and the experimental results for the supersaturated liquids providing strong evidence that microdroplets containing highly concentrated KBr solutions are dominated by Bjerrum pairs before spontaneous crystallization occurs. The spectral shoulder clearly arises from the formation of hydrated KBr clusters. This means that this feature is considered to be an indication for the formation of hydrated KBr clusters. In contrast to the other solutions (NaBr, CaBr, and ZnBr₂) studied in this work, where cluster-rich but still single phase solutions occur, we demonstrate in the case of KBr solutions that the spectral features of the liquid and the solid phase can be distinguished. This means that similar as for calcium carbonate, stable hydrated clusters of KBr can be formed as an intermediate phase before crystallization occurs, even though no stable macroscopic hydrate phases have been reported for this solute [RADHA 2010]. It is noted that such hydrated

clusters are not a stable phase of KBr and can only temporally form in supersaturated microdroplets of KBr solutions.

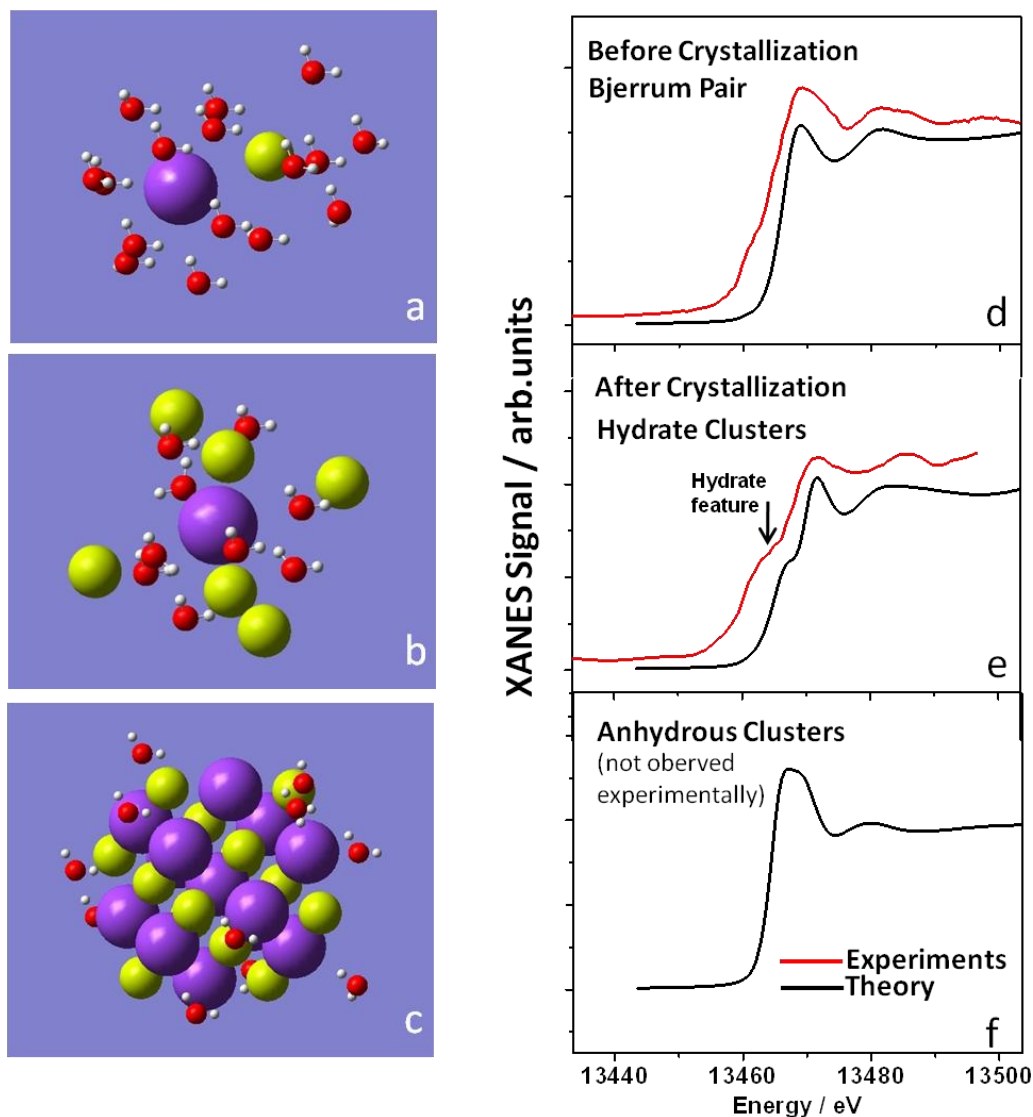


Figure 4.13. XANES spectra of KBr droplets are taken at energy of Br K-edge under humidity conditions close to the efflorescence point of KBr solution. Single droplets are injected into an optical trap with a relative humidity of about 60% at room temperature (298 K). The experimental results are shown as red solid lines and the calculated curves from model simulations are given in black solid lines (see text for further details). Three model structures are considered for theoretical simulations: (i) the monomer ion-pair surrounded by water ($d_{\text{K-Br}} = 3.85 \text{ \AA}$, $d_{\text{K-O}} = 3.95 \text{ \AA}$), (ii) hydrated solute clusters ($d_{\text{K-Br}} = 5 \text{ \AA}$, $d_{\text{K-O}} = 3.85 \text{ \AA}$), and (iii) anhydrous solute clusters in solution ($d_{\text{K-Br}} = 3.3 \text{ \AA}$, $d_{\text{K-O}} = 3.8 \text{ \AA}$). The purple and yellow spheres symbolize potassium and bromine atoms, respectively.

In this work, the “shoulder feature” was not only observed in the Br K-edge of a dilute KBr solutions with initial concentration of 0.9 M. Similar spectral features were, however, also observed in XANES spectra taken at Na K-edge of sodium fluoride (NaF), sodium chloride (NaCl), and sodium bromide (NaBr) solutions, as shown in Fig 4.14. The Na K-edge of these three solutions occurs at nearly the same energy position ($E = 1078$ eV) for all three systems presenting, according to a tentative assignment also “hydrate features”. It is noted that the Na K-edge is located in the soft X-ray regime. This requires changes of the experimental setup (see Section 3.3), implying that studied aqueous droplets are suspended under ambient conditions ($T = 300$ K) at 25% relative humidity. This means large amount of water evaporates from the surface, where the droplet has a higher concentration than the initial values of each sample solution which is given in Table. 3.2. Because soft X-ray can hardly penetrate any materials in the size regime of the millimeter droplets used in this specific experiment, where the attenuation length of the soft X-rays used for this work is about $3\text{ }\mu\text{m}$ at the Na K-edge considering a concentration of the sample solutions (see Section 3.8), the recorded XANES spectra (in Fig. 4.14) carry basically the information of the droplet-air interface.

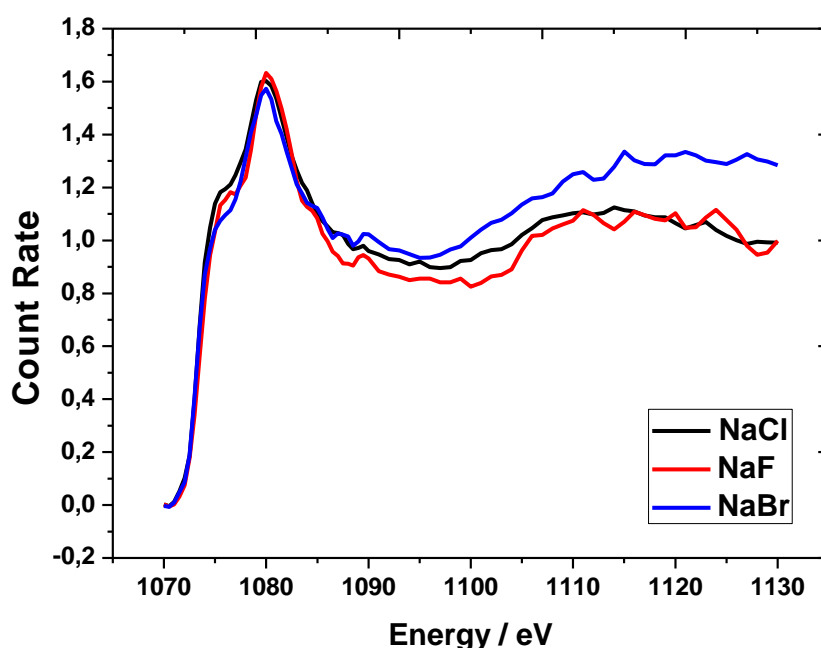


Figure 4.14. XANES spectra of NaF, NaCl, and NaBr taken in the energy regime of Na K-edge. Single microdroplets with a diameter of 1-2 mm were generated by a pipette. The experimental setup used for these measurements is introduced in Section 3.3.

Specifically, the droplets are relatively large ($d = 1\text{-}2\text{ mm}$) and they are not levitated, where they are connected to the tip of a pipette (see Section 3.3). This is unlike freely levitated microdroplets, since there is still a connection to the liquid reservoir inside the tip. Therefore, any increase in solute concentration, which results from evaporation of water, can be compensated by diffusive transport from the reservoir, so that the degree of supersaturation of such droplets is quite limited. As a result, it is almost impossible for such droplets connected to a pipette tip to become supersaturated, and the solute Na^+ ions are mostly surrounded by water. Aziz and coworkers performed model simulations on Na K-NEXAFS spectra for different model clusters [AZIZ 2006]. Comparing their calculated spectra with the present experimental curves, it is straightforward to assume that the Na^+ ions are coordinated by six water molecules forming $\text{Na}^+(\text{H}_2\text{O})_6$ clusters. This implies that different anions (F^- , Cl^- , Br^-) are not present in the first solvation shell of cations and have no significant influence on the electronic structure of Na^+ ions. However, as a result of water evaporation from the droplet surface, a concentration gradient may be formed near the liquid-air interface. Therefore, hydrated solute clusters may be formed near the droplet surface and result in hydrate features, occurring as shoulders in the near-edge regime, similar to the findings on supersaturated KBr droplets.

4.4 Charge Effects on the Nucleation Process of Single Levitated Droplets

4.4.1 Efflorescence Measurements of Single Neutral/Charged Droplets

The efflorescence points of neutral droplets and droplets with excess charges are measured according to the experimental procedures outlined in Section 3.6. The experimental setups used for these measurements are an optical levitation trap and an electrodynamic levitation trap (EDLT) for studying neutral and charged droplets, respectively. The experimental details of these two levitation methods have been described in Chapter 3 (Experimental Section). Sample solutions of potassium chloride (KCl) and sodium chloride (NaCl) with an initial concentration of 10% are used for sample preparation.

As shown in Fig. 4.15, the crystallization time of single levitated droplets of a KCl solution are plotted as a function of the relative humidity in the trap chamber. Each

data point is marked by a specific symbol. Black dots represent neutral droplets which are levitated in the optical levitation trap, and blue diamonds correspond to a charged droplet suspended in the EDLT. All levitated droplets in the EDLT were initially negatively charged, and the charge amplitude was experimentally determined (see Section 3.5) to be between $-(140 \pm 14)$ fC and $-(260 \pm 26)$ fC. It is important to point out that in order to compare the efflorescence points of neutral and charged droplets levitated in different levitation chambers that several experimental problems might arise. Firstly, there might be different humidity gradients in the setups used for such work. To overcome this problem, a setup was built, which combines both levitation methods, where the optical levitation option was built into the climate chamber of the EDLT. Detailed information on this experimental setup is described in Section 3.7. This also avoids artifacts caused by the use of different gauges for measuring the humidity. By comparing the efflorescence points measured by different setups of optical levitation (Section 3.1 and Section 3.7), one can calibrate the possible experimental errors caused by the use of different levitation chambers. The red triangles in Fig. 4.15 correspond to neutral droplets, which are optically trapped in the ELDT chamber. This result shows that droplets levitated in the EDLT chamber have the same efflorescence humidity as the optically trapped ones. This demonstrates that the two setups yield identical results, indicating that there are no humidity gradients influencing the efflorescence point. Another problem for optical levitation is that in large volume levitation chambers convection and turbulences of the atmosphere may occur, which makes optical levitation studies more difficult. Therefore, the ELDT setup was only used for a few droplets along with optical levitation, verifying that both setups yield identical results.

The determination of the efflorescence points relies on a large number of repeated measurements on droplets of well defined size with a diameter of $20\text{ }\mu\text{m}$, where more than 300 droplets were studied. More than ten droplets were measured at each relative humidity which was controlled to slowly decrease as a function of time. On the average, the relative humidity was decreased by 1% per 20 minutes. The experimental results shown in Fig. 4.15 suggest that, when relative humidity is lower than 60% (or 48%), the crystallization time for most of the charged (or neutral) droplets suddenly decreases to 1–2 seconds. This is because the water evaporates quickly from the droplet surface and spontaneous formation of critical clusters near the surface is

promoted. However, with an increase in humidity water evaporation is hindered, and the crystallization processes are prevented to occur in a short time period [HAMZA THESIS, HAMZA 2004].

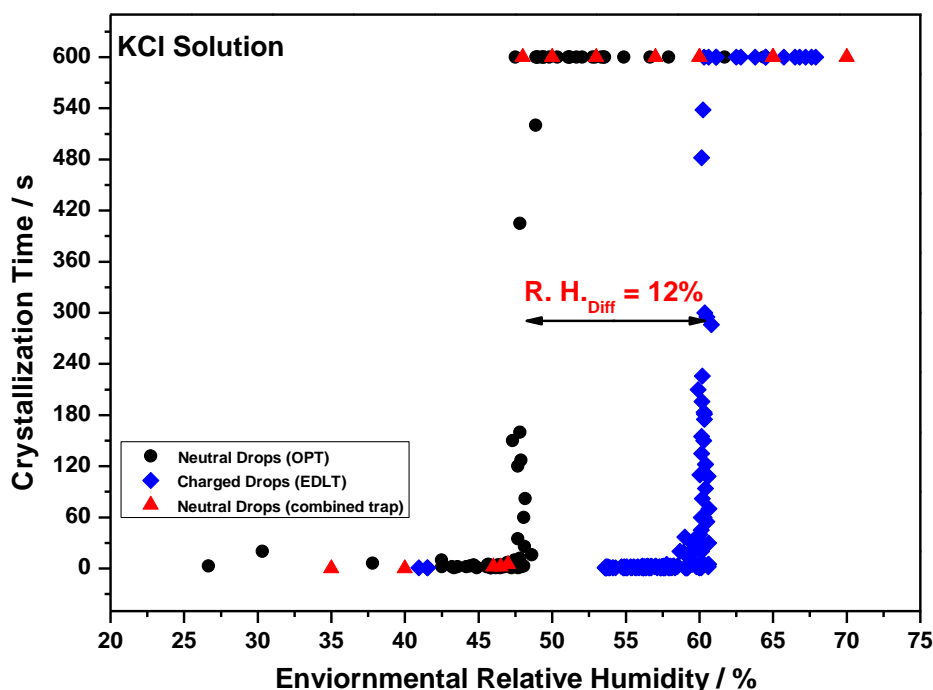


Figure 4.15. The efflorescence points of single neutral and charged KCl droplets. The black dots refer the neutral droplets levitated in an optical levitation cell and blue diamonds correspond to negatively charged droplets with electric charge of $-(240 \pm 24)$ fC levitated in the EDLT. The red triangles correspond to neutral droplets, which are optically levitated in the combined setup of an optical trap and EDLT.

By comparing neutral and charged droplets, it is noticed that the efflorescence point of the charged droplets is observed at higher humidity than that of the neutral ones. Specifically, the efflorescence point of an aqueous KCl solution is $48 \pm 1\%$ relative humidity for neutral droplets (black dots in Fig. 4.15) and $60 \pm 1\%$ for charged droplets (blue diamonds) which have an excess charge of $-(240 \pm 24)$ fC. Such a significant difference, which corresponds to $12 \pm 2\%$ of relative humidity, has been confirmed and reproduced for several times to exclude all possible artifacts that might occur. This result demonstrates that charged droplets are promoted to undergo efflorescence at higher water vapor pressure than the neutral ones. Therefore, it is

straightforward to assume that the efflorescence process is influenced by the electrical excess charges distributing preferentially on the droplet surface [TABAZADEH 2002].

Further experiments were also carried out using different solutes, such as sodium chloride (NaCl) with an initial concentration of 10%. However, there was no difference in efflorescence humidity observed between neutral droplets ($q = 0$ fC) and charged ones with an electric charge of $-(240 \pm 24)$ fC. According to the charging in the EDLT, droplets generated in the piezo injector are charged instantaneously during the injection. Thus, $-(240 \pm 24)$ fC is the maximal charge amplitude one can achieve in this way. Such low charge might explain that there is no difference in efflorescence humidity between neutral and slightly charged droplets. This hypothesis was further investigated by applying significantly higher charges on the levitated aqueous NaCl droplets. This is accomplished by using an electrode at which a high voltage on the order of 2-3 kV was applied so that the charge state of the droplets is significantly increased [TURKMEN THESIS]. With this method, the charge density on the aqueous droplets can be adjusted by varying the applied voltages on the electrode, resulting in a maximum charge of $-(2.2 \pm 0.3)$ pC. The efflorescence points of all the NaCl droplets were measured by using the optical levitation setup (see Section 3.1).

The efflorescence points of NaCl droplets containing various charge states are shown in Fig. 4.16. All droplets were negatively charged for these measurements. As shown, with an increase in absolute charge from zero (neutral droplet) to $-(2135 \pm 300)$ fC, the efflorescence point of the droplets gradually shifts to higher relative humidity. This result is fully consistent with the results observed for KCl solution droplets. The only difference between both systems is that NaCl droplets require a higher excess charge than KCl solutions to reach a noticeable promotion of efflorescence by electrical charges.

The efflorescence points are plotted as a function of the excess charge, as shown in the inset of Fig. 4.16. It shows that for NaCl solution droplets, there is only a small increase of the efflorescence point when the number of charges is increased from zero to $-(260 \pm 26)$ fC. However, for droplets with an excess charge of $-(400 \pm 40)$ fC to $-(550 \pm 55)$ fC, there is a steep increase in efflorescence point from $47 \pm 1\%$ to $59 \pm 1\%$ relative humidity at 25 ± 0.5 °C. This implies that an excess charge of $-(400 \pm 40)$ fC is sufficient to promote nucleation, where a small change in excess charge results in a significant influence on the crystallization process. When the charge state

of the droplets is increased to $-(2135 \pm 300)$ fC, the efflorescence point does not change further and remains almost constant at $59 \pm 1\%$ - $61 \pm 1\%$ relative humidity. This provides important information that the efflorescence process in aqueous solutions is promoted by a charge threshold, which is evidently a solute-dependent property.

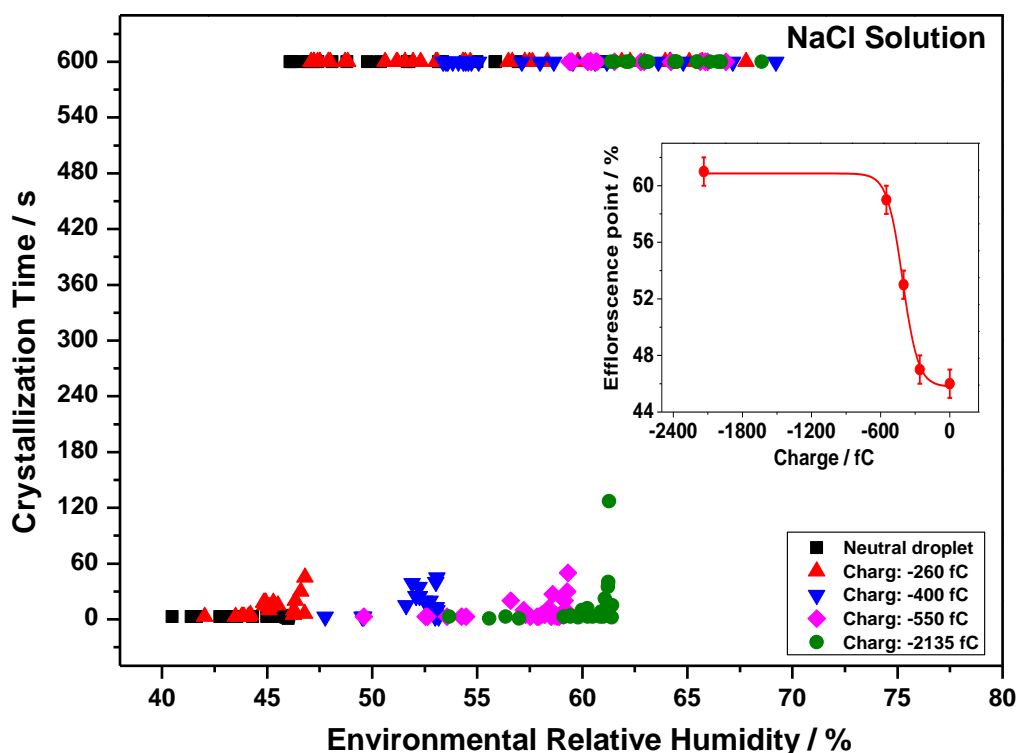


Figure 4.16. Efflorescence points of single neutral and charged NaCl droplets with a diameter of 20–25 μm . The initial concentration of NaCl in the droplets is 10%. The inset shows the dependence of the efflorescence point of NaCl droplets as a function of the number of electrical excess charges.

4.4.2 Charge Effects on the Efflorescence of Single Levitated Droplets

According to Fig. 4.15 and Fig. 4.16, under ambient conditions, the efflorescence points of charged droplets are up to more than 10% higher in relative humidity than those of neutral droplets. In order to assign the stimulating effects inducing nucleation as a function of excess charges, we performed molecular dynamics (MD) simulations on sodium chloride (NaCl) solutions using the CP2K package [INTE1, INTE2] together

with many-body-potentials in order to calculate classical molecular dynamic trajectories by means of pair potential interactions.

As shown in Fig 4.17 (a) and (c), two initial model structures are considered, in which a negative charge (OH⁻) is placed inside and outside of an *fcc* Na₄Cl₄ octahedron. In both models we consider a volume of 20 × 20 × 20 Å³ with periodic boundary conditions. The cutoff constant in the Ewald summations α was equal to 0.44 and the cutoff radius for short range interactions equals 11.0 Å.

In both model structures, NaCl clusters are embedded into an environment of 150 water molecules. The initial distance between OH⁻ and Na⁺ is equal to 4.6 Å and between two Na⁺ ions a distance of 6.7 Å determined. A standard Coulomb pair potential $V_{Coul} = Ze^2/r$ is used to describe the electrostatic interactions between hydrogen (q = 0.417 e) and oxygen (q = - 0.834 e). The long range interactions between water molecules, and between water and solute ions, are described by Lennard-Jones potentials [LENNARD-JONES 1924, INTE3]:

$$V_{L-J} = \varepsilon \left[\left(\frac{r_m}{r} \right)^{12} - 2 \left(\frac{r_m}{r} \right)^6 \right] \quad (4.8)$$

where ε is the depth of the potential well, r is the distance between two particles, and r_m is the distance at which the potential reaches its minimum. The potential parameters depending on the type of ions or molecules are given in Table 4.4.

Table 4.4 Lennard-Jones potential parameters

Interaction	ε (kJ / mol)	r_m (Å)
Cl ⁻ - H ₂ O	0.42	4.934
Na ⁺ - H ₂ O	0.012	3.736
H ₂ O - H ₂ O	0.64	3.537

Cl⁻ and Na⁺ ions have an electrical charge of -1.0 e and 1.0 e, respectively. The short range interactions between the solvated ions are treated in the framework of the Born-Mayer formalism [BORN 1932, BORN 1946]:

$$V_{B-M} = Ae^{-Br} \quad (4.9)$$

where A and B are constants for a given pair of the atoms and r is the internuclear separation between the atoms. Table 4.5 summarizes the values used for the calculations.

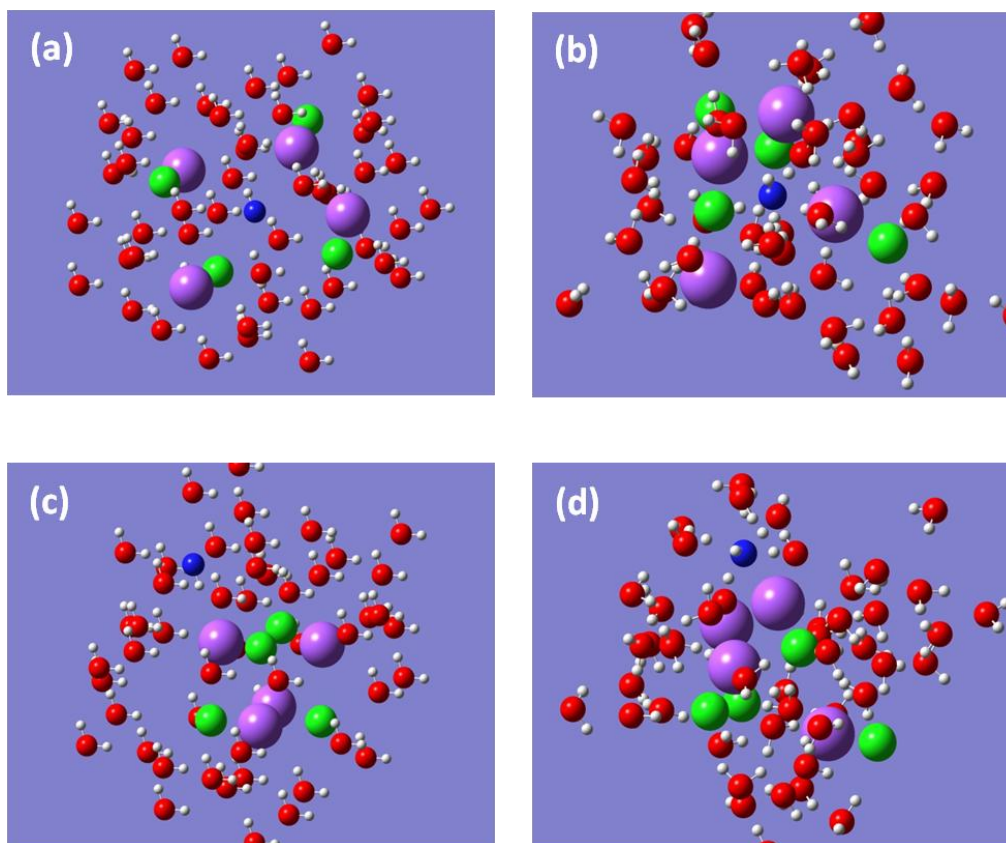


Figure 4.17. Molecular dynamics snapshots of negatively charged aqueous solutions of NaCl. Two models are considered with a single negative OH^- (marked in blue color) which is enclosed in a water solvation shell located either inside or outside an fcc octahedron of Na_4Cl_4 (Na^+ : purple spheres, Cl^- : green spheres). (a) and (c) are the starting configurations; the geometries after a simulation time of 5 ps are given in (b) and (d), respectively.

Table 4.5 Born-Mayer parameters [ABRAHAMSON 1969, SANGSTER 1976, FUMI 1964]

Interaction	A (eV)	B (\AA^{-1})
Cl – Cl ⁻	6411.8	3.636
Na – Na ⁺	3661.4	3.777
Na ⁺ - Cl ⁻	4845.2	3.706

The two initial geometries (Fig. 4.17 (a) and (c)) are relaxed within 5 ps simulation time and their corresponding final geometries are given in Fig. 4.17 (b) and (d), respectively. In the two final configurations, where due to electrostatic interactions between OH^- and Na^+ ions, the octahedron of Na_4Cl_4 clusters are strongly deformed and the anion OH^- links two neighboring Na^+ ions. Therefore, the resulting distances, either between Na^+ ions or between Na^+ and OH^- , become considerably shorter than the values in the initial configurations (as shown in Table 4.6). Furthermore, attractive forces between OH^- and Na^+ disintegrate the solvation shell initially surrounding the OH^- ions. This mechanism provides a clear picture of how electrical excess charges act as a linker introducing an indirect contact between solute ions. As a result, they clearly promote aggregation of solute clusters on short time scales. Even though mechanisms of nucleation process in electrolyte solutions have been proposed in both classical and non-classical approaches [ZETTLEMOYER 1969, GEORGALIS 2000], increasing evidence, including the present simulations, indicates that the nucleation process can be influenced by negative excess charges (see Section 1.1).

Table 4.6 Distance between sodium ions or sodium and hydroxyl ions in the initial and final configurations of molecular dynamics simulations shown in Fig. 4.17

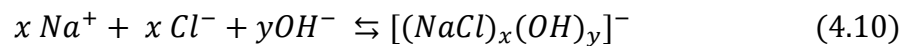
	$\text{Na}^+ - \text{Na}^+$ (distance Å)	$\text{Na}^+ - \text{OH}^-$ (distance Å)
In Fig. 4.19 (a)/(c) (Initial) (OH^- inside/outside Na_4Cl_4)	6.7	4.6
In Fig. 4.19 (b) (Final) (OH^- inside Na_4Cl_4)	4.8	2.45
In Fig. 4.19 (d) (Final) (OH^- outside Na_4Cl_4)	3.74	2.35

In classical nucleation theory, clusters in supersaturated solution evolve via single atom attachment and no interactions between solute clusters are taken into account [VOLMER 1939, BECKER 1935]. From this point of view, the present simulations provide a convincing proof that negative electrical excess charges, corresponding to OH^- in this work, in supersaturated NaCl solutions can be considered as preferential sites where the solute ions initially start to aggregate. The excess charge might eventually locate either inside or outside these growing clusters depending on the orientation of the solvated ions during solution. Due to the simplification of the

nucleation process, many drawbacks of the classical nucleation theory have been pointed out and discussed in previous works [ERDEMIR 2009]. One of the important thermodynamic points is that classical nucleation theory considers exclusively enthalpic effects, i.e. interaction potential of the system, whereas entropic solvent effects are neglected.

Recently, a non-classical view regarding solvent effects on the nucleation process was introduced by Gebauer et al. [GEBAUER 2008]. They proposed that during the nucleation process in aqueous solutions, thermodynamically stable clusters are formed at the *prenucleation stage* which is defined as the very early stage of crystallization. This means that the formation of clusters is based on a thermodynamic equilibrium, instead of a stochastic mechanism that is used in classical nucleation theory. The position of this equilibrium can be influenced by the properties of the solvent, such as the pH value of the solution [GEBAUER 2008]. The resulting small and stable clusters play an important role in the nucleation process [NAVROTSKY 2004, HORN 2001, GEBAUER 2008].

The significant difference between the efflorescence points of charged and neutral microdroplets (Fig. 4.15 and Fig. 4.16) is also partially attributed to solvent effects. In the MD simulations, interactions between the excess charge stabilized by OH^- and solvated ions were initially prevented by the solvation shell of OH^- . However, due to the electrostatic attractive forces between OH^- and Na^+ , there is a strong tendency for a loss of the solvation shell, and stable prenucleation clusters can be readily formed in charged droplets. Therefore, in comparison with neutral droplets, in which subcritical clusters are formed via local concentration fluctuations, charged clusters can evidently more efficiently grow in the presence of excess charges, which is a result of the negative excess charge. Therefore, a NaCl solution containing excess charges (OH^-) tends to form $(\text{NaCl})_x$ clusters according to,



where x is the number of ion pairs contained in thermodynamically stable clusters of NaCl, and y is the number of electrical charges involved in cluster formation.

Further, there is a distortion of the solvation shell, affecting the structure of water molecules, i.e. hydrogen-bond network, which is also modified. Model studies of

charged particles [MYLAND 2002] suggested that electrical charges localized on the droplet-air interface create an electrical potential, which further modifies the surface tension of aqueous droplets [ZHANG 2001, IAVARONE 2003, WHEELER 2008]. From the classical Lippmann equation [LIPPMANN 1873], which gives the relationship between the surface tension and the electrostatic potential, Weon and coworkers [WEON AND MARGARITONDO 2008] derived a physical model that correlates the reduction of the surface tension with the surface charge density and the Rayleigh limit of Coulomb explosion,

$$\frac{\gamma_{\omega}}{\gamma_{\omega i}} = [1 + 4(\sigma/\sigma_R)^2]^{-1/2} \quad (4.11)$$

where γ_{ω} and $\gamma_{\omega i}$ are the modified and initial surface tension, respectively; σ is the surface charge density of the droplet, and σ_R is the Rayleigh limit of Coulomb explosion [RAYLEIGH 1882]. It should be noted that this model is suitable for any liquid droplet size [WEON AND MARGARITONDO 2008].

According to Eq. (4.11), the surface tension of a charged droplet decreases with increasing surface charge density. Recently, it was found [WEON 2008] that even a low surface charge density could significantly decrease the surface tension of water droplets. This means that for charged droplets, the intermolecular forces, which attract liquid molecules to minimize their surface area, is decreased. As a result, water molecules can more easily escape from this net force by evaporation [SEINFELD 1988]. Obviously, this process has a promoting effect on the formation of critical clusters.

According to the experimental results and the model simulations, we demonstrated that negative electrical excess charges have a stimulating effect on the formation of solute clusters which aggregate to form critical clusters more readily at a given humidity. Consequently, the nucleation process in aqueous solutions is promoted. This result provides another effective method for controlling the phase transition process from liquid to solid. Furthermore, we found that the number of charges required for promoting nucleation in aqueous solutions is solute-dependent. For example, for droplets of KCl solution at room temperature, $-(240 \pm 24)$ fC of electrical charge is sufficient to increase the efflorescence point from $48 \pm 1\%$ to $60 \pm 1\%$. However, aqueous droplets of NaCl with a similar excess charge of about $-(260 \pm 26)$ fC have nearly the same efflorescence point ($47 \pm 1\%$) as the neutral ones ($46 \pm$

1%), i.e. no promoting effect is observed. In order to significantly change the efflorescence point of NaCl one needs to increase the excess charge up to -400 fC. We suggest that this phenomenon is related to the number size of critical clusters for initializing the nucleation process (see Section 2.3).

Therefore, in order to assign the different nucleation behaviors of KCl and NaCl droplets with nearly the same number of negative excess charges, we performed calculations regarding to the size of critical clusters which is required to grow in both solutions. It is noted that for this calculation, it is only possible to define an upper and a lower limit of the critical cluster size, instead of the exact values of constituents contained in such a critical cluster (Section 4.1.1). As shown in Fig. 4.18, the size of critical clusters is given as a function of solute concentration in the droplets, which can be determined according to the corresponding curves shown in the inset. For both KCl and NaCl solution droplets, the solute concentrations corresponding to their efflorescence points of the neutral and charged droplets are indicated in the insets of Fig. 4.18 by red and purple dashed lines, respectively. Subsequently, the resulting concentration values are used to determine their corresponding number of constituents in the critical clusters, which is based on calculated curves in Fig. 4.18. Note that the electrical excess charge loaded on both KCl and NaCl droplets has almost the same magnitude, corresponding to $-(250 \pm 25)$ fC.

For KCl solution, the upper and the lower limits of the critical number size are close to each other, which means that the number size of solute ions contained in the critical clusters of KCl is distributed in a narrow size range. As shown in Fig. 4.18, neutral droplets of KCl have at the efflorescence point a solute concentration which is 16 molal, the critical number size is on the average about 2.3 molecules/cluster. When the droplets carry about $-(250 \pm 25)$ fC of excess charges, the efflorescence humidity rises to 60%, which corresponds to an about 11 molal solution, and the number size of critical clusters is about 2.7 molecules/cluster, i.e. somewhat higher than without excess charges. This result indicates that in KCl solution a significant decrease in solution concentration, i.e. an increase of relative humidity occurs, whereas only a small change in critical number size of solute clusters is observed. Moreover, the experimental results have demonstrated that such a small increase in critical number size can be compensated by the promoting charge effects as discussed at the beginning of this Section.

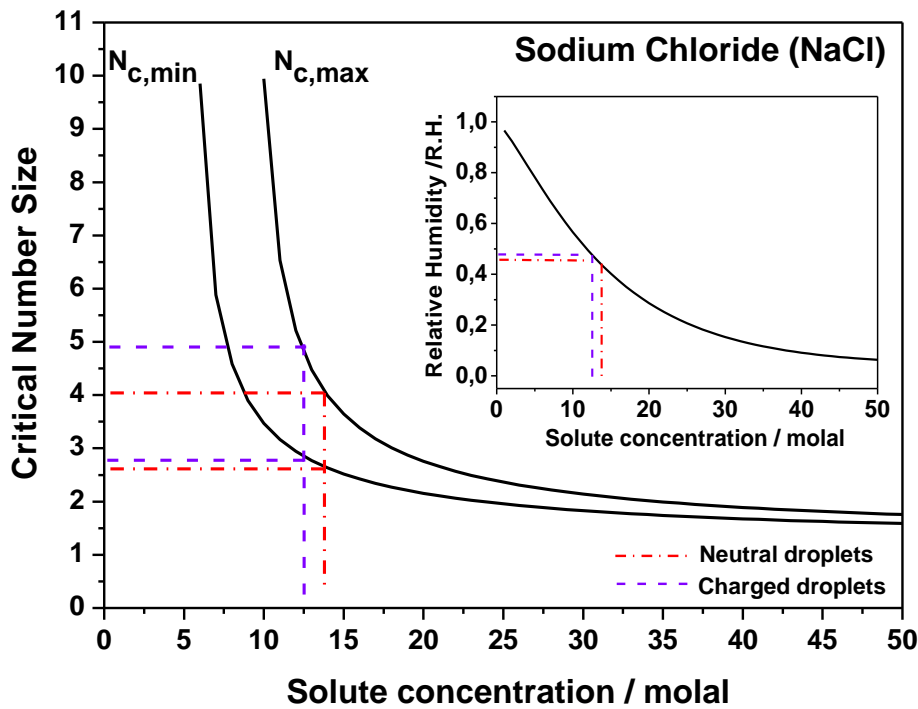
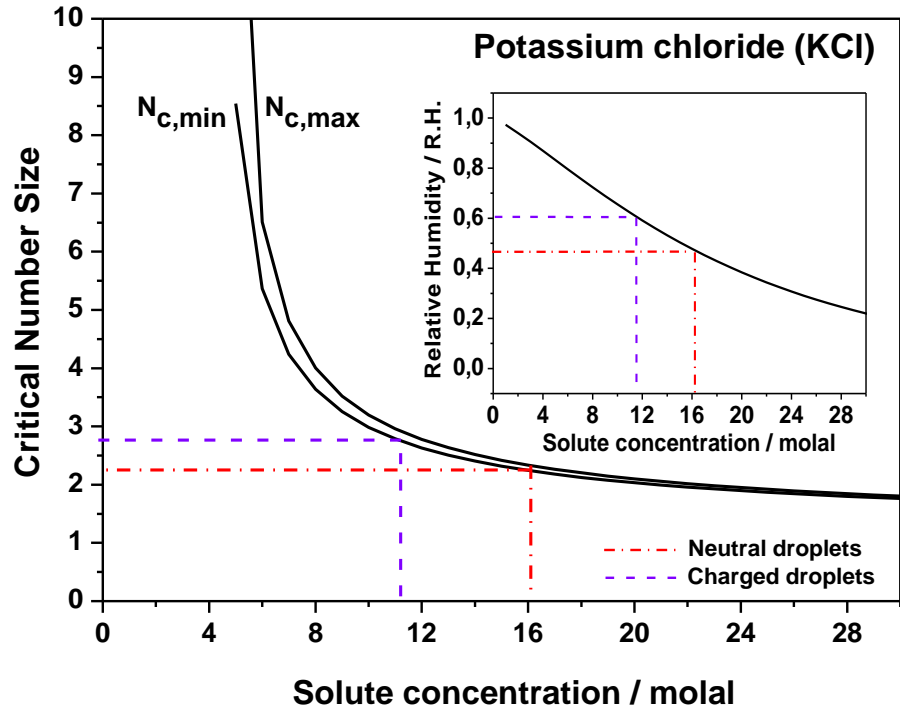


Figure 4.18. Calculated curves of the upper, $N_{c,max}(298\text{ K}, n_0)$, and the lower, $N_{c,min}(298\text{ K}, n_0)$, limits for the number size of critical clusters $N_c(298\text{ K}, n_0)$ in KCl and NaCl solutions as function of solute concentration at room temperature, $n_0(T)$. The solute concentrations corresponding to the efflorescence points of KCl and NaCl neutral droplets are indicated by red dash-dotted lines, whereas the purple dashed lines stand for the corresponding charged droplets. Note that the negative excess charge carried by KCl and NaCl droplets is similar, corresponding to $-(250 \pm 25)$ fC. Each value of solute concentration is obtained from the corresponding inset of the humidity-concentration curves.

However, the situation is different, when a solution of NaCl is considered. From the calculated curves of NaCl shown in Fig. 4.18, one can clearly see that the area between the curves defining the upper and the lower limits of the critical number size is considerably bigger than that of a KCl solution, i.e. the NaCl solution has a broader size distribution at the critical cluster size. This indicates a possible requirement for a larger critical cluster size. For example, the efflorescence point for neutral NaCl droplets is found at a relative humidity of $46 \pm 1 \%$, which corresponds to a 13.7 molal solute concentration, where the critical cluster sizes ranges between 2.6 to 4. For droplets with an excess charge of about $-(250 \pm 25)$ fC, efflorescence occurs at $47 \pm 1 \%$ relative humidity, where the solute concentration is about 12.5 molal. This value is quite close to that of the neutral droplets. However, such a small decrease in solute concentration results in a significant increase of the number size of the critical clusters. As shown in Fig. 4.18, the critical number size in charged NaCl droplets is in the range between 2.7 and 5 molecules per cluster, which is a considerably broader size range than is derived for neutral droplets. According to the similar efflorescence points between neutral and charged NaCl droplets, we experimentally demonstrated that the efflorescence promoting effects of the excess charges could compensate this, leading to an increase in the size distribution of critical clusters. However, efflorescence points of droplets with such small net charges are difficult to be promoted to higher humidity, i.e. significantly lower solute concentration and larger critical clusters. In order to reach this regime, one needs to apply higher excess charges to NaCl droplets (for example -400 fC), as shown in Fig. 4.16.

These results can be understood that there is a threshold of excess charge required for promoting efflorescence at higher relative humidity. We also observed that above this threshold, the efflorescence humidity starts to increase with the magnitude of the applied excess charge. However, above this threshold saturates at certain level of excess charge. This is because, once the excess charge reaches certain value, critical clusters can be easily formed near the surface, where the charge density is highest and cluster formation becomes almost independent from the charge density. As a result, the efflorescence point of charged droplets cannot be significantly changed any more.

4.5 Simulations of Scattering Patterns in Crystallizing Droplets

It is well known that when incident photons shine on particles of similar or larger size than the wavelength of the incident radiation, Mie scattering patterns occur. Scattering images are composed of dark and bright fringes [BOHREN 2010, MIE 1908]. However, for single levitated aqueous droplets, solid clusters are formed when solute concentrations of droplet solutions become supersaturated. As a consequence, Mie scattering patterns become slightly modified, or they even vanish upon the occurrence of irregular speckle patterns, as discussed in previous work of Berge et al. [BERGE1999].

In order to analyze the particle dependent information carried out in such scattering patterns, we used a high speed video camera (Motion Pro X4) to measure the scattering patterns of single levitated microdroplets during optical levitation. This CCD camera allows us to take 30000 frames/second. Therefore, this device is able to follow size dependent changes in scattering patterns, which occur upon evaporation of the solvent and phase transitions. These scattering patterns are assigned by performing model simulation with the “discrete dipole approximation” (DDA) [DRAINE 1994]. More information can also be found in Section 2.5.

Fig. 4.19 shows two images taken from the same NaCl droplet by the high speed camera. This droplet was generated with an initial solute concentration of 20%, and it is levitated at an ambient humidity of $60 \pm 1\%$. The image showing the bigger droplet ($d = 38 \pm 0.5\ \mu\text{m}$) was taken when the droplet was just injected into the optical trap by the piezo droplet generator. The other image ($d = 19 \pm 0.5\ \mu\text{m}$) was recorded after about 10 s of levitation time. The significant decrease in size from $38 \pm 0.5\ \mu\text{m}$ to $19 \pm 0.5\ \mu\text{m}$ indicates a substantial evaporation of water during the first seconds of levitation, which has been properly described by the Kelvin equation [STEINER 1999]. Similar findings have also been reported for KCl solution droplets [HAMZA THESIS, HAMZA 2004]. In that work, it was demonstrated that after injecting the droplets at a relative humidity of $56 \pm 1\%$, they underwent a substantial loss of water, so that the solute concentration was increased until a thermodynamic equilibrium was reached between the levitated droplet and its surrounding gas phase. This process takes typically about 10 to 15 seconds. Afterwards, no substantial change in the droplet

diameter is observed before spontaneous nucleation occurs upon further lowering of the ambient humidity [COHEN 1987].

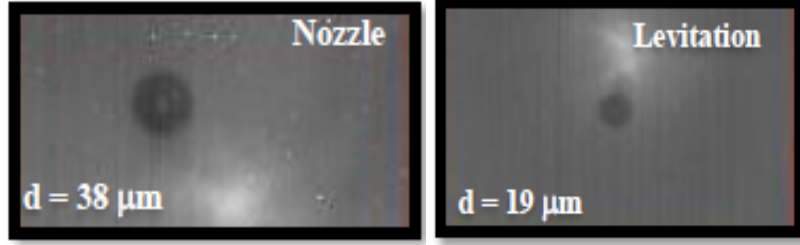


Figure 4.19 Images of aqueous microdroplets containing initially 20% NaCl. The initial droplet diameter is $38 \pm 0.5 \mu\text{m}$. The images are taken by a high speed camera at $60 \pm 1\%$ relative humidity and room temperature ($T = 298 \text{ K}$). Left: This image was taken immediately after droplet injection into the optical trap ($d = 38 \pm 0.5 \mu\text{m}$). Right: Image of the same droplet after 10 s levitation in the trap. The droplet diameter shrinks to $19 \pm 0.5 \mu\text{m}$.

After the most substantial loss of water during an “induction time”, the solute concentration of the droplet becomes saturated or even supersaturated. As the scattering patterns of dilute and saturated droplets are quite different from those of supersaturated solutions [BERGE, 1999], identification of solute structures within such optically levitated droplets is performed via a “fingerprint” comparison with theoretical simulations using discrete dipole approximation (DDA) [DRAINE 1994].

DDA is an approximation method which is used to calculate the scattering and the absorption of electromagnetic waves by targets of arbitrary geometry. In this approximation, a continuum target is replaced by a finite array of polarizable points, which acquire dipole moments in response to the local electric field [DRAINE 1994]. For a given target geometry, one can generate a certain dipole array, which is located within the volume V of the continuum target by using algorithm introduced by Draine [DRAINE 1994]. A more detailed description of this method is given in Chapter 2 (see Section 2.5) and in the literature [DRAINE 1994, DRAINE 2004].

DDSCAT is a software package to perform DDA calculations, in which the quantity of scattering efficiency factor is determined by:

$$Q_{sca} \equiv C_{sca}/\pi a_{eff}^2 \quad (4.12)$$

where the “effective radius” a_{eff} is defined as $a_{eff} \equiv (3V_{target}/4\pi)^{1/3}$. C_{sca} is the scattering cross section, which is described as:

$$C_{sca} = \frac{k^2 \exp(ikr)}{r} \sum_{j=1}^N \exp(-ik\hat{r} \cdot \mathbf{r}_j) (\hat{r}\hat{r} - \mathbf{1}_3) P_j \quad (4.13)$$

where $k=2\pi/\lambda$, λ is the wavelength of the radiation in vacuum. $E_{inc,j}$ is the electric field of the incident wave at \mathbf{r}_j . α_j and P_j are the polarizability and polarization of dipole j .

A typical Mie scattering pattern which is composed of bright and dark fringes or stripes is shown in Fig. 4.20(a). This experimental image containing 14 dark stripes was taken with the high speed camera when an aqueous droplet ($d = 25 \pm 1 \mu\text{m}$) containing 10% sodium chloride (NaCl) was levitated at room temperature ($T = 298 \text{ K}$). The environmental relative humidity was $65 \pm 1\%$. The geometry of the liquid microdroplets is assumed to be spherical. Simulations of such scattering pattern were carried out with the initial configuration given in the inset of Fig. 4.20(b). The red sphere symbolizes an aqueous droplet with a typical droplet diameter of $25 \pm 1 \mu\text{m}$. This target sphere was replaced by 10^7 scattering blocks. A sphere has the highest possible symmetry. Thus, the location and the orientation of the target in both laboratory and target systems (see Section 2.5) have no influence on the scattering pattern.

The simulated scattering image based on the assumed geometry is shown in Fig 4.20 (b). Since the refractive index of dilute aqueous solutions are nearly the same as that of water given by Segelstein. In the present simulations the real part of the refractive index was taken as 1.33 and the imaginary part was 0.01 [SEGELSTEIN 1981]. As a result, consistent scattering patterns are obtained from experiments and simulations (see Fig. 4.20). This means that for single levitated microdroplets, it is reasonable to consider them as spheres [DUFT 2003]. With decreasing relative humidity, the droplet becomes supersaturated and solute clusters form, which may modify the initial scattering pattern.

Note that due to the limitations of CPU capacity, for theoretical simulation one can only use 8 millions of scattering units, which result in the maximal droplet diameter of $8 \mu\text{m}$, corresponding to maximum of 10 stripes in the simulated scattering patterns. Thus, the theoretical simulations cannot fully reach the size regime of the experimental droplets. Nevertheless, the size of the microdroplets has an influence on

the scattering patterns, where smaller particles generate a smaller number of stripes per scattering angle.

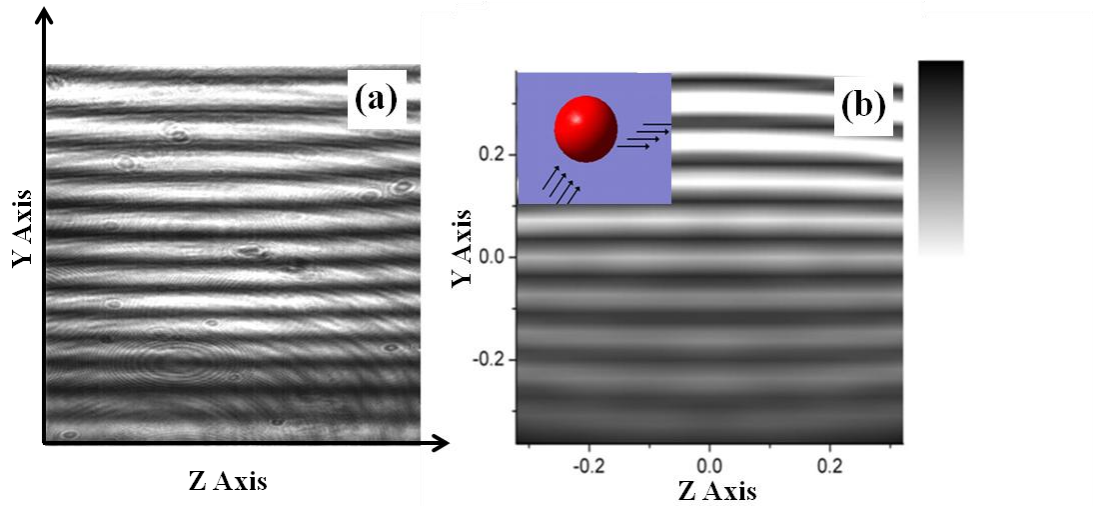


Figure 4.20. (a) Mie scattering pattern experimentally taken from a droplet ($d = 25 \pm 1 \text{ } \mu\text{m}$) of NaCl with an initial concentration of 10%. This image is a typical Mie scattering pattern of a single levitated droplet. (b) Simulation of Mie scattering pattern for single spherical droplet. The calculation is done with the scattering geometry given in the inset of (b). The red sphere representing for a single levitated droplet has diameter of $8 \text{ } \mu\text{m}$. The black arrows show the direction of the incident and the scattered light.

Solutions of levitated droplets could easily become supersaturated by evaporating large amounts of water during levitation. Additionally, the solute concentration of the aqueous droplets is fully controlled by adjusting the relative humidity of the droplet environment. Therefore, the solute concentration undergoes a further increase and reaches eventually supersaturation. As a result, phase separation occurs in the liquid droplet in order to stabilize the metastable supersaturated solution. As a consequence of the formation of solid clusters, the incident light waves are scattered from these clusters yielding significant changes in scattering patterns [BERGE, 1999]. When the clusters reach a critical size (see Section 2.3), subsequent crystallization eventually occurs throughout the entire volume. The resulting solid crystals provide specific scattering images.

Fig. 4.21 (a) and (d) are two different scattering images observed during experiments. Fig. 4.21 (a) was measured using droplets of 10% NaCl solution at $80 \pm 1\%$ relative humidity. The initial diameter of the droplet is $80 \pm 1 \text{ } \mu\text{m}$. This scattering image is similar to the typical Mie image of liquid solution (see Fig 4.20), but with only a few

stripes (stripe number: 6) confined in a narrow regime. Fig. 4.21 (d) shows a scattering pattern of a droplet of 10% NaCl solution. The initial diameter of the droplet is $50 \pm 1 \mu\text{m}$. In this feature, the regular stripes are distorted and a “mesh-like” structure is observed. Similar images were reported in previous results [BERGE 1999].

The occurrence of such speckle patterns indicates that the formerly aqueous droplets almost transformed into solids. Therefore, in order to assign the reasons for the formation of such irregular scattering patterns, the scattering properties of solid crystals of different geometries have been simulated, which goes beyond previous work by Berge [BERGE THESIS].

Solids which are formed via crystallization of solutions are optically transparent as the liquid, but their shapes are evidently non-spherical [BERGE 1999, KIRMACI 1979, MOTEGI 1978, ZOLC 1973]. It is assumed that solute crystals of aqueous droplets are cubic. As shown in Fig. 4.21 (c), a single cubic solid with $4 \mu\text{m}$ edge (8 millions scattering units) symbolizes a solid cube of NaCl crystal after phase transitions from the liquid. Similar to the spherical target, the cubic solid is also replaced by 10^8 scattering blocks, and due to the CPU capacity, this is the maximum of particle size that we can simulate. The orientation of the target in the coordinate system refer to the incident light is shown in Fig 4.21 (c). The laboratory frame is denoted by axes of X , Y , Z . The incident radiation propagates along X axis. The target orientation in the coordinate system is denoted by axes a_1 and a_2 , which are defined by angles Θ , Φ , and β (see Section 2.5). Θ is the angle between the X axis of the fixed laboratory coordinate system and the a_1 axis of the target system. When β equals to 0, the a_2 axis is located in the X, a_1 plane. Therefore, when all the three angles are defined as zero ($\Theta = 0^\circ$, $\Phi = 0^\circ$, $\beta = 0^\circ$), the laboratory frame and the target system overlap (as shown in Fig. 4.21 (c)). Model simulations are performed to generate a scattering pattern corresponding to such instant scattering geometry, as shown in Fig. 4.21 (b). The results indicate that the experimental and modeled results show evidence for the formation of a single cubic solid via crystallization.

It is experimentally demonstrated that for different levitation techniques solid particles are not at rest in levitation traps. For example, in EDLT, solid particles undergo a regular motion with certain frequency which is related to the ac frequency applied to the electrodes [BERGE 1999, BERGE, UNPUBLISHED WORK]. The motion of optically levitated particles along the laser beam is also experimentally observed in

present work. Superimposed to this motion is the convection of the atmosphere surrounding the levitated particle. As a result, the orientation of the crystal with respect to the laser beam may be different depending on the motion of the trapped particles.

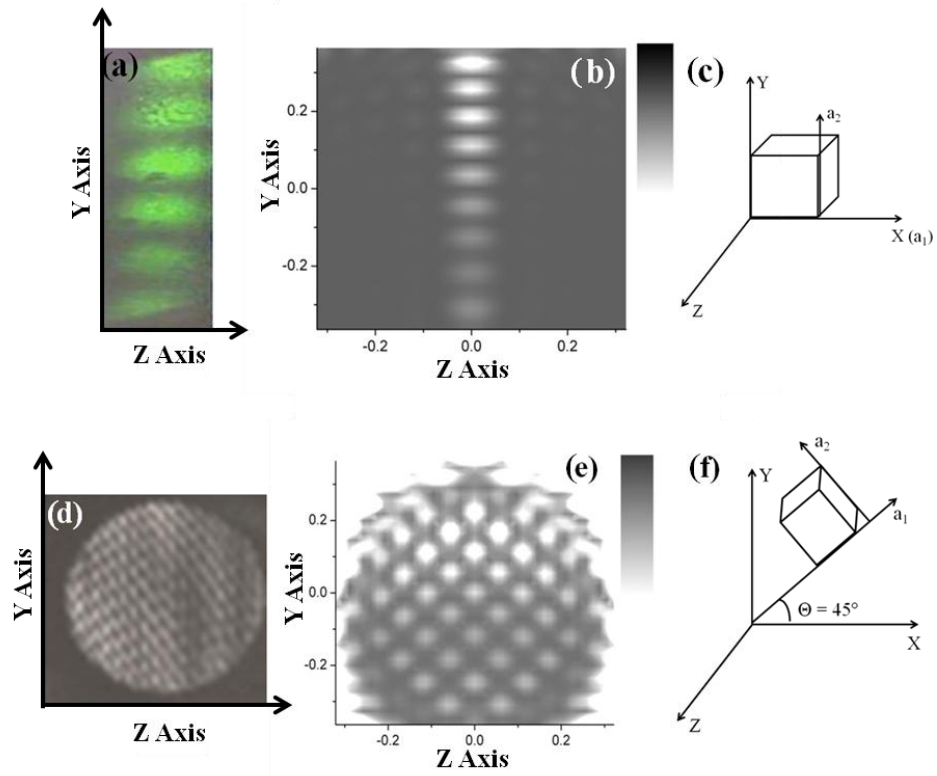


Figure 4.21. Two different scattering patterns measured with single levitated droplets of a 10% NaCl solution. (a) Scattering pattern taken from a droplet with an initial diameter of $80 \pm 1 \mu\text{m}$. The scattering pattern is similar to a typical Mie pattern, but the stripes are confined in a narrow regime. (b) Simulated scattering pattern of a solid cube with $4 \mu\text{m}$ edge length. The orientation of the cube in the coordinate systems is shown in (c). (d) A “mesh-like” scattering pattern which is experimentally taken from droplets of the same NaCl solution (initial diameter: $50 \pm 1 \mu\text{m}$). (e) Simulated scattering pattern when the cubic target shown in (c) is rotated by 45° in the laboratory frame. The resulting geometry is shown in (f).

An important difference between the geometries of a sphere and a cube is that a sphere has the highest possible symmetry, whereas a cube has octahedral symmetry. This implies that the orientation of a spherical particle with respect to the incident angle of the laser beam cannot affect the scattering image. In contrast, different orientation of cubic solids in the coordinate system could result in different scattering patterns [BERGE 1999, HEFFELS 1995]. Therefore, further simulations are carried out

with the angle Θ changing from $\Theta = 0^\circ$ to $\Theta = 45^\circ$, as shown in Fig. 4.21 (f). The simulated scattering pattern is shown in Fig. 4.21 (e) in which a squared mesh is likely being rotated by about 45° - 60° in the plane of the image. This result is in general agreement with the experimental pattern shown in Fig. 4.21 (d).

The agreement between the experimental and simulated scattering patterns demonstrates that single cubic crystals are formed via crystallization of liquid droplets, and the scattering pattern changes depending on the orientation of such solid cube in the laboratory frame. Thus, due to the instability of such levitated solids, the scattering patterns shown in Fig. 4.21 (a) and (d) can be alternatively observed. Similar to the typical Mie image, the scattering pattern of a cubic crystal also shows regularities, depending on the actual orientation in the laser beam.

It is also possible that solid and liquid phases occur simultaneously during nucleation. This is because metastable supersaturated solutions can be stabilized via phase separation, where microcrystals of solutes are formed (Section 2.4). Scattering patterns of microdroplets containing solid crystals are simulated by similar methods introduced above. As shown in the inset of Fig. 4.22 (b), the simulation contains 55 small spheres with a diameter of $0.16\ \mu\text{m}$, which are embedded in a spherical water environment with $4\ \mu\text{m}$ diameter. The target is again replaced by 8 millions scattering units due to the mentioned CPU memory limits. In principle, the microcrystals are randomly distributed over the entire droplet volume. Therefore, different orientations of such target in the coordinate systems result in the identical, averaged scattering patterns.

A simulated scattering pattern of this model is shown in Fig. 4.22 (b). The image is different from the ones observed above and no clear structure is shown in this Figure. Such irregular scattering pattern is often experimentally observed, as shown in Fig. 4.22 (a). This result reveals that microcrystals are often formed, and a solid and a liquid phase coexist simultaneously within the droplet. The irregular scattering pattern is formed because the incident light is scattered by both the liquid and solid phases, so that the scattering process is more complicated than that in a homogeneous liquid solution or a pure solid crystal. Consequently, the light wave is scattered randomly and the scattering pattern has no clear stripe structure.

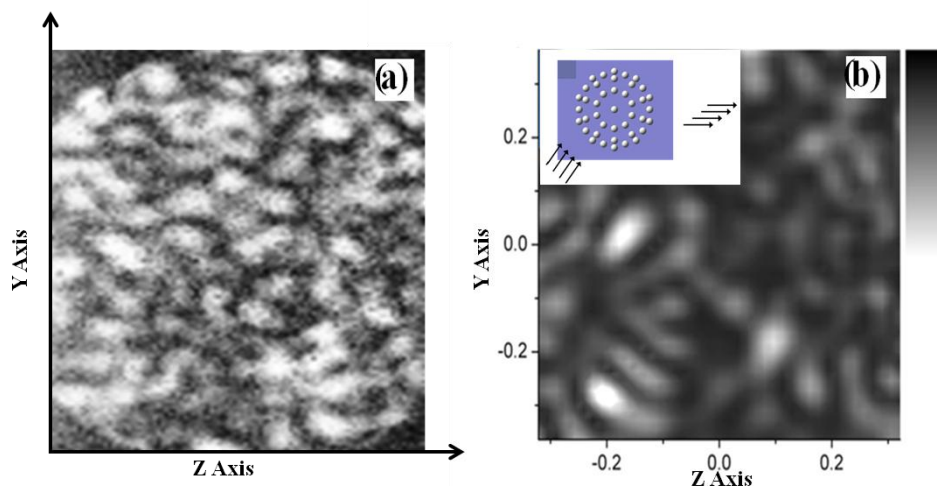


Figure 4.22. (a) Scattering pattern of single levitated droplets which are initially prepared from a 20% NaCl solution at 60% relative humidity; (b) Simulated scattering image from 55 small spheres (diameter: $0.16\ \mu\text{m}$) embedded in a spherical water environment (diameter: $4\ \mu\text{m}$), as shown in the inset of the Figure.

It is noted that simulations were also carried out when the small spherical crystals (Fig. 4.22 (b) inset) were substituted by small cubes of the same size. But the resulting patterns did not agree with any of the experimental results observed in this work. This demonstrates that solute microcrystals in droplet solutions are spherical, instead of cubic. However, these solute crystals are not necessary perfect spheres. In fact, the shape and the size of crystals formed in a solution droplet are influenced by several factors, such as the solute concentration or the electric charge on the droplet surface [DRAPER, 2007].

Chapter 5

Conclusions and Outlook

5.1 Conclusions

We investigated phase transitions from supersaturated microdroplets containing aqueous salt solutions, where solid crystals are formed via efflorescence. Contact-free storage of these droplets permits to reach a high degree of supersaturation by means of optical levitation for neutral droplets as well as electrodynamic levitation for electrically charged droplets. The diameter of the levitated droplets was determined by Mie scattering. The occurrence of the phase transitions was identified by characteristic changes in the angle resolved Mie patterns.

The transition process from the liquid to the solid was mainly studied by tracking the evolution of solute clusters in droplets containing no excess charges during homogeneous nucleation, and also by comparing the efflorescence points of neutral and charged droplets to explore charge effects on the nucleation process. The most important results of these experiments that are assigned by model simulations are summarized as follows:

Homogeneous nucleation in supersaturated solutions is studied by following changes in electronic structures of solvated ions or clusters in microdroplets. XANES spectra are recorded in the energy regime of the Br K-edge for aqueous solutions of NaBr and CaBr_2 , and in the Zn K-edge regime for ZnBr_2 solutions. The main results derived from these systems are:

For aqueous droplets of NaBr solutions, recorded in the Br K-edge regime, XANES spectra are taken in the humidity regime of 50-30%, corresponding to a supersaturated solution up to 10.6 M. The Br K-edge shows initially a blue-shift which is followed by a red-shift with decreasing humidity corresponding to increased concentration of the solution. The edge positions of thin films containing a dilute NaBr solution and the solid crystals occur nearly at the same energy (13459.9 eV) which is lower than those of supersaturated droplets.

The simulations of two sodium bromide model nanoclusters show that the energy shift of the Br K-edges is a result of the coordination of the Br site. The maximum coordination of a Br_{nc} site is 6 and therefore, unsaturated Br_{nc} sites ($n < 6$) can form a maximum of $6-n$ hydrogen bonds with solvating water molecules. Simulated XANES spectra show that the Br K-edge shifts to lower energies when increasing the coordination of a given Br_{nc} site. As a result, Br_{nc} sites either bind at high concentration directly to a Na site within a nanocluster or they are forming hydrogen bonds with solvating water molecules, contributing similarly to the magnitude of the computed spectral shifts in XANES spectra. Further, in droplet solutions under ambient conditions the averaged degree of solvation of NaBr clusters does not reach its maximum, i.e. the number of water molecules forming hydrogen bonds with a given Br_{nc} site is expected to be in average lower than $6-n$. However, in dilute solutions or the solid crystals, most Br_{nc} sites are fully coordinated by hydrogen bonds or Na atoms. Therefore, their Br K-edges occur at lower energy as compared to the supersaturated solution droplets.

Further measurements are performed using aqueous CaBr_2 solutions. Br K-edge XANES spectra are measured in the humidity regime of 64% - 45%. As a result of the significant decrease in the relative humidity (about 20%), the core level absorption edges of Br^- ions and clusters systematically shift to lower energy. As compared to the spectra of supersaturated microdroplets, the Br K-edge of the dilute CaBr_2 solution occurs at higher energy and that of the solid crystals at lower energy.

These results are evident for the formation of solute clusters which modify efficiently the local electronic structure of the absorbing ions or solute clusters, leading to a lowering of the absorption energy during spontaneous nucleation from the liquid to the solid. Spectral simulations of two model structures (single Br^- ion or CaBr_2 monomer surrounded by water molecules) verify that in dilute solution it is dominated by solvated ions, and ion pairs (Bjerrum pairs) and solute clusters are formed in supersaturated solutions.

Solutions of ZnBr_2 are studied in the energy regime of the Zn K-edge. Similar to the results observed for CaBr_2 solutions, the Zn K-edge gradually shifts to lower energy during the transition from dilute solution to dry solid crystals. These results also demonstrate that Bjerrum pairs of ZnBr_2 are formed in supersaturated solution

droplets, and XANES spectra of the cations (Zn^{2+}) show similar changes in XANES spectra as compared to the anions (Br^-).

Near-edge structures of KBr droplets are measured at relative humidity close to its efflorescence point. The prominent difference between the XANES spectra taken pre- and post-crystallization is a spectral shoulder which occurs only after crystallization. Theoretical modeling provides strong evidence that this spectral shoulder arises from the formation of hydrated KBr clusters.

Another main subject of this work is the study of charge effects on the homogeneous nucleation process. The efflorescence points of neutral and charged droplets of KCl and NaCl solutions are measured.

For KCl solution, the efflorescence point of neutral droplets is $48 \pm 1\%$ humidity, and for charged droplets ($- (240 \pm 24) \text{ fC}$) this quantity is increased to $60 \pm 1\%$. These results provide evidence that charged droplets of KCl solutions crystallize at lower solute concentration than the neutral ones, which implies that electrical excess charges have a promoting effect on the homogeneous nucleation process in supersaturated microdroplets.

For NaCl solutions, because of its characteristic broad size distribution of the critical clusters, significant enhancement of efflorescence by electrical excess charges is not observed unless the excess charge is increased to $- (400 \pm 40) \text{ fC}$. This implies that there is a threshold of excess charge for the charge stimulated nucleation process. Above this threshold, efflorescence increases as a function of charge state until the excess charges get saturated at a certain value, where the formation of critical clusters is independent from the charge density. Molecular dynamics simulations were performed on NaCl solutions demonstrating that negative excess charges are able to attract the surrounding Na^+ ions in solution. Consequently, prenucleation solute clusters are more readily formed in charged droplets than in the neutral ones. This is the main reason why the nucleation process is promoted in charged droplets and efflorescence occurs at higher humidity.

Scattering patterns are assigned to the geometries and orientations of clusters by comparing the experimental results to model simulations using the “discrete dipole approximation” (DDA). Spherical liquid droplets containing no solute clusters show typical Mie scattering patterns. Such images are likely to be confined in a narrow

humidity regime. They are distorted when single cubic crystals occur via crystallization, which are orientated differently in the laboratory frame. Entirely irregular scattering patterns are observed, when small solid crystals are formed in droplet solutions, which explains the features of experimental scattering patterns of highly supersaturated solution droplets.

5.2 Outlook

The work described in this thesis contributes to the fundamental understanding of the nucleation process from liquid to solid. To this end, two main research lines were considered: (i) XANES spectroscopy was used to follow the continuous changes in the electronic structure of different ionic salts during nucleation, and (ii) the promoting effects of negative charges on homogeneous nucleation were investigated based on the crystallization time of neutral and charged microdroplets. Nevertheless further challenges in experimental techniques and theoretical approaches still remain in the field. For example, in the cases of nucleus containing 100 – 1000 atoms, there are almost no experimental techniques capable to provide direct insight into the atomic arrangements of such particles. From a theoretical viewpoint, classical nucleation theory is the simplest and broadly used approach. However, in many situations, nucleation deviates significantly from the classical regime [GEBAUER 2008, KIRSCHHOCK 1999]. Therefore, improving modern techniques in the laboratory and theoretical models are mandatory requirements to see further progress in the field.

Summary

This work is devoted to gain fundamental understanding of homogeneous nucleation of salt solutions in supersaturated microdroplets. Essentially, two main aspects of the nucleation process are considered: (i) the progressive changes in local electronic structure of selected ions during nucleation, which are monitored by means of XANES spectroscopy combined with optical levitation; and (ii) the promoting effects of negative charges on the nucleation process of supersaturated solution, which is achieved by comparing the humidity-dependent crystallization time of neutral and charged microdroplets. Optical and electrodynamic levitation techniques are used to suspend neutral and charged droplets, respectively.

XANES spectra are recorded in the energy regime of Br K-edge (Zn K-edge) for supersaturated microdroplets of NaBr, CaBr₂ (ZnBr₂), and their corresponding dilute thin film solutions and solids. For supersaturated droplets, repeating XANES spectra are measured with decreasing humidity. Systematic changes in the energy positions of the absorption edges are experimentally observed for each sample solution and compared with theoretical simulations. For solutions of CaBr₂ (ZnBr₂), the Br K-edges (Zn K-edges) shift to lower electronic energy when the solvated Br⁻ (Zn²⁺) ions transfer from liquid to solid. Whereas, the Br K-edges of NaBr solution shift first to higher energy and then back to lower energy at certain relative humidity.

Charge effects on nucleation process are studied with sample solutions of KCl and NaCl. *Efflorescence point*, which is defined as the relative humidity where the crystallization time of levitated droplets suddenly decreases from more than 600 s to less than 2 s, is measured for both neutral and charge droplets of these model systems. For KCl solutions, the efflorescence point of charged droplets which has an excess charge of $-(240 \pm 24)$ fC is $12 \pm 2\%$ of relative humidity higher than that of neutral ones. Similar results are also observed for NaCl solutions. Nevertheless, NaCl solutions require a higher charge amplitude than KCl solutions to obtain a significant increase of the efflorescence point; this is due to the size difference of the critical clusters for both salts. Molecular dynamics simulations of NaCl solution demonstrate that a negative charge (OH⁻) acts as a linker between two neighbor Na⁺ ions in

solution, which means solute clusters are more ready to form in a charged solution, and therefore, initialize the nucleation process.

Overall, we have successfully recorded XANES spectra of single levitated droplets and studied charge effects, which allow us to probe the nucleation process on an unprecedented molecular level. This could provide the basics for further investigations of more complex systems and the development of improved homogeneous nucleation theories.

Zusammenfassung

Diese Arbeit ist dem fundamentalen Verstehen von homogener Nukleation von Salzlösungen in übersättigten Mikrotröpfchen gewidmet.

Im Wesentlichen werden zwei Hauptaspekte des Nukleationsprozesses betrachtet:

- (i) Die fortschreitenden Änderungen in der elektronischen Struktur von ausgewählten Ionen während der Nukleation. Diese werden mittels XANES Spektroskopie, die mit optischer Levitation kombiniert ist, überwacht;
- (ii) Die begünstigenden Effekte von negativen Ladungen auf den Nukleationsprozess von übersättigten Lösungen, welche durch den Vergleich der Abhängigkeit der Luftfeuchtigkeit auf die Kristallisationszeit von neutralen und geladenen Mikrotröpfchen erzielt werden.

Optische und elektrodynamische Levitationstechniken werden entsprechend verwendet um neutrale und geladene Tröpfchen einzufangen.

XANES Spektren werden im Energiebereich der Br K-Kante (Zn K-Kante) für übersättigte Mikrotröpfchen aus NaBr, CaBr₂ (ZnBr₂) und den entsprechend zugehörigen verdünnten dünnen Filmlösungen und Festkörpern aufgenommen.

Bei übersättigten Tröpfchen wurden wiederholende XANES-Spektren mit verringernder Luftfeuchtigkeit aufgenommen. Systematische Änderungen der Energiepositionen der Absorptionskanten, werden experimentell erhalten für jede Lösung und verglichen mit theoretischen Simulationen.

Für Lösungen aus CaBr₂ (ZnBr₂) verschieben sich die Br K-Kanten (Zn K-Kanten) zu niedrigeren elektronischen Energien, wenn die solvatisierten Br⁻ (Zn²⁺) Ionen von der Flüssigkeit zum Festkörper übergehen. Hingegen verschieben sich die Br K-Kanten der NaBr Lösung erst zu höheren Energien und dann zurück zu niedrigeren Energien bei einer bestimmten relativen Luftfeuchtigkeit.

Ladungseffekte auf den Nukleationsprozess werden studiert mit KCl- und NaCl-Lösungen. Der Effloreszenzpunkt, welcher als die relative Luftfeuchtigkeit, bei der die Kristallisationszeiten der levitierten Tröpfchen plötzlich um mehr als 600 s bis

hin zu 2 s weniger abnehmen, definiert ist, wird für neutrale und geladene Tröpfchen dieser Modellsysteme gemessen.

Für KCl Lösungen, ist der Effloreszenzpunkt von geladenen Tröpfchen, welche eine überschüssige Ladung von $-(240 \pm 24)$ fC hat, $12 \pm 2\%$ relativer Luftfeuchtigkeit höher als das von neutralen.

Ähnliche Ergebnisse wurden für NaCl-Lösungen erhalten. Dennoch fordern NaCl-Lösungen einen höheren Ladungsausschlag als KCl-Lösungen um eine signifikante Erhöhung des Effloreszenzpunktes zu erhalten. Dies beruht auf den Größenunterschieden der kritischen Cluster für beide Salze.

Simulationen der Molekuldynamik von NaCl-Lösungen demonstrieren, dass eine negative Ladung (OH^-) verhält sich wie eine Bindung zwischen zwei Nachbar- Na^+ -Ionen in Lösung, was bedeutet dass gelöste Cluster eher bereit sind sich in geladenen Lösungen zu formen und, daher den Nukleationsprozess initialisieren.

Zusammengefasst haben wir erfolgreich XANES-Spektren von levitierten Tröpfchen aufgenommen und die Ladungseffekte, welche uns erlauben den Nukleationsprozess in noch nie dagewesenen molekularen Level zu erforschen. Dies könnte die Basis für weitere Untersuchungen komplexerer Systeme and Entwicklung von verbesserten homogenen Nukleationstheorien liefern.

References

A

Abraham, Farid F., *Homogeneous nucleation theory: The pretransition theory of vapor condensation*, **Academic Press** (New York), **1974**.

Abrahamson, Adolf A., *PHYSICAL REVIEW*, **178**, 76, **1969**.

Accelrys **2008**, Materials Studio 4.4.

Aguiar, J. A.; Asta, M.; Grönbech-Jensen, N.; Perlov, A.; Milman, V.; Gao, S.-P.; Pickard, C. and Browning, N. D.; *J. Phys.: Conf. Ser.* **241**, 012062, **2010**.

Allen, A. T.; Mcdonald, M. P.; Nicol, W. M. and Wood, R. M., *Nature*, **235**, 36, **1972**.

Andres, R. P; and Boudart, M., *J. Chem. Phys.* **42**, 2057, **1965**.

Arnold, F., *Nature (London)*, **284**, 610, **1980**.

Ashkin, A., *Phys. Rev. Lett.*, **24**, 156, **1970**.

Ashkin, A., *science*, **210**, 1081, **1980**.

Aziz, E. F.; Zimina, A.; Freiwald, M.; Eisebitt, S; and Eberhardt, W., *J. Chem. Phys.*, **124**, 114502, **2006**.

B

Bakhoun, S. F. W. and Agnes, G. R., *Anal. Chem.*, **77**, 3189, **2005**.

Ball, P., *H₂O. A biography of water* (Phoenix, London, **1999**)

Bartlett, R. J. and Stanton, J., in *Reviews in computational chemistry*, edited by Lipkowitz K. B. and Boyd D. B., **Vol.V** (VCH Publishers, New York, **1994**).

Bathow, G.; Freytag, E. and Hänsel, R., *J. Appl. Phys.* **37**, 3449, **1966**.

Becke, A. D., *Phys. Rev.*, **A 38**, 3098, **1988**.

Becker, R. and Doering, W., *Annalen Der Physik*, **24**, 719, **1935**.

Berge, B.; Steiner, B; and Rühl, E, unpublished work.

Berge, B.; Sudholz, K.; Steiner, B.; Rohmann, J. and Rühl, E., *Phys. Chem. Chem. Phys.*, **1**, 5486, **1999**.

- Blomberg, M. R. A. and Seigbahn, P. E. M., *J. Phys. Chem. B.*, **105**, 9375, **2001**.
- Bogan, M. J.; Bakhoun, S. F. W. and Agnes, G. R., *J. Am. Soc. Mass. Spectrosc.*, **16**, 254, **2005**.
- Bohren, C. F. and Huffman, D. R., *Absorption and Scattering of Light by Small Particles*. John Wiley and Sons, INC., New York, **1998**.
- Bohren, C. F. and Singham, S. B., *J. Geophys. Res.* **96**, 5269, **1991**.
- Bohren, C. F. and Huffmann, D. R., *Absorption and scattering of light by small particles*, New York, Wiley-Interscience, **2010**.
- Born, M. and Mayer, J. E., *Z. Physik*, **75**, 1, **1932**.
- Born, M. and Oppenheimer, R., *Ann. d. Physik*, **84**, 457, **1927**.
- Born, M., *Atomic Physics* (Hafner Publishing Co., New York, **1946**), p. 262.

C

- Cahn, J. W. and Hilliard, J. E., *J. Chem. Phys.* **28**, 258, **1958**.
- Cahn, J. W. and Hilliard, J. E., *J. Chem. Phys.* **31**, 688, **1959**.
- Car, R. and Parrinello, M., *Phys. Rev. Lett.*, **55**, 2471, **1985**.
- Carlson, T. A. and Krause, M. O., *Phys. Rev. Lett.*, **17**, 1079, **1966**.
- Carlson, T. A. and Krause, M. O., *Phys. Rev. Lett.*, **14**, 390, **1965**.
- Cavalleri, M.; Odelius, M.; Nilsson, A. and Pettersson, L. G. M., *J. Chem. Phys.*, **19**, 121, **2004**.
- Cavalleri, M.; Odelius, M.; Nilsson, A. and Petersson, L. G. M., *J. Chem. Phys.*, **121**, 10065, **2004**.
- Cavalleri, M., *Local Structure of Hydrogen-Bond Liquids*, Stockholm University, **2004**.
- Chayen, N. E.; Saridakis, E.; El-Bahar, R. and Nemirovsky, Y., *J. Mol. Biol.*, **312**, 591, **2001**.
- Chayen, N. E.; Saridakis, E. and Sear, R. P., *Proc. Natl. Acad. Sci. U.S.A.* **103**, 597, **2006**.
- Chen, Y.; Fulton, J.L. and Partenheimer, W., *J. of Sol. Chem.* **34**, 903, **2005**.

Clark, S. J.; Segall, M. D.; Pickard, C. J.; Hasnip, P. J.; Probert, M. I. J.; Refson, K. and Payne, M. C., *Z. Kristallogr.*, **220**, 567, **2005**.

Cohen, M. D.; Flagen, R. C. and Seinfeld, J. H., *J. Phys. Chem.*, **91**, 4563, **1987**.

Cziczo, D. J.; Nowak, J. B.; Hu, J. H. and Abbatt, J. D. P., *J. Geophys. Res.* **102**, 18843, **1997**.

D

Gebauer, D.; Volkel, A. and Colfen, H., *Science*, **322**, 1819, **2008**.

Debenedetti, Pablo G., *Metastable Liquids: Concepts and Principles*, **Princeton University Press** (41 William Street, Princeton, New Jersey 08540), **1996**.

Demo, P. and Kožíšek, Z., *Physical Review B*, **48**, 3620, **1993**.

Diao, Y.; Helgeson, M. E.; Myerson, A. S.; Hatton, T. A.; Doyle, P. S. and Trout, B. L., *J. Am. Chem. Soc.*, **133**, 3756, **2011**.

Draine, B. T. and Flatau, P. J., *Opt. Soc. Am. A*, **11**, 1491, **1994**.

Draine, B. T., *Astrophys. J.*, **333**, 848, **1988**.

Draine, B.T., “The Discrete-Dipole Approximation for Light Scattering by Irregular Targets”, in *Light Scattering by Nonspherical Particles: Theory, Measurements, and Geophysical Applications*, ed. M.I. Mishchenko, J.W. Hovenier, and L.D. Travis (N.Y.: Academic Press), **311**, **2000**.

Draine, B.T. and Goodman, J. J., *Astrophysical J.*, **405**, 685, **1993**.

Draine, B. T. and Flatau, P. J., “User guide for the discrete dipole approximation code *DDSCAT 6.1*”, <http://arxiv.org/abs/astro-ph/0409262v2>, **2004**.

Draper, N.D.; Bakhoun, S. F.; Haddrell, A. E. and Agnes, G. R., *J. Am. Chem. Soc.*, **129**, 11377, **2007**.

Duft, D.; Achtzehn, T.; Müller, R.; Huber, B. A. and Leisner, T., *Nature*, **421**, 128, **2003**.

E

Egerton, R. F., *Electron Energy-Loss Spectroscopy in the Electron Microscope* **Plenum Press**, New York, **1996**.

Erdemir, D.; Lee, A. Y. and Myerson, A., *Acc. Chem. Res.*, **42**, 621, **2009**.

F

- Fermi, E., *Acc. Naz. Lincei*, **6**, 602, **1927**.
- Filippone, F. and Parrinello, M., *Chem. Phys. Lett.* **345**, 179, **2001**.
- Fock, V., *Z. Physik*, **61**, 209, **1930**.
- Fokin, V. M. and Zanotto, E. D., *J. Non-Cryst. Solids*, **265**, 105, **2000**.
- Follath, R.; Schmidt, J. S.; Siewert, F.; Holldack, K.; Zeschke, T.; Frentrup, W.; Schmitz, D. and Sawhney, K. J. S., *Vol. 705* (Eds: Tony W., Joachim S., Howard A. P., John A.), AIP, **2004**, pp.348.
- Frenkel, J., *Kinetic Theory of Liquid*, New York. Dover Publication Inc., **1955**.
- Friedlander, S. K., *Smoke, dust and haze, fundamentals of aerosol behavior*. New York: Wiley, **1977**.
- Fuchs, M. and Scheffler, M., *Comput. Phys. Commun.*, **119**, 67, **1999**.
- Fulton, J. L.; Chen, Y. S.; Heald, S. M. and Balasubramanian, M., *J. Chem. Phys.*, **125**, 094507, **2006**.
- Fulton, J. L.; Heald, S. M.; Badyal, Y. S. and Simonson, J. M., *J. Phys. Chem. A* **107**, 4688, **2003**.
- Fumi, G. and Tosi, M. P., *J. Phys. Chem. Solids*, **25**, 31, **1964**.

G

- Gamero-Castaño, M.; Juan Fernández de la Mora, *J. Chem. Phys.*, **117**, 3345, **2002**.
- Gao, S.-P.; Pickard, C. J.; Payne, M. C.; Zhu, J. and Yuan, J., *Phys. Rev. B*, **77**, 115122, **2008**.
- Gaspar, A. M.; Marques, M. Alves; Cabaco, M. I.; Marques, M. I. de Barros; Buslaps, T. and Honkimäki, V., *Journal of Molecular Liquids*, **110**, 15, **2004**.
- Gebauer, D.; Völkel, A. and Cölfen, H., *Science*, **322**, 1819, **2008**.
- Georgalis, Y.; Kierzek, A. M. and Saenger, W., *J. Phys. Chem. B*, **104**, 3405, **2000**.
- Ginde, R. M. and Myerson, A. S., *Journal of Crystal Growth*, **116**, 41 **1992**.
- Gmelins Handbuch der anorganischen Chemie. Begründet von Leopold Gmelin. Herausgegeben von Gmelin – Institut für anorganische Chemie und Grenzgebiete in

der Max – Plank – Gesellschaft zu Förderung der Wissenschaften in Verbindung mit der Gesellschaft Deutscher Chemiker.

Grebennikov, V. I.; Babanov, Y. A. and Sokolov, O. B., *Phys. Stat. Sol.*, **79**, 1773, **1997**.

Guggenheim, E. A., *Thermodynamics*. An Advanced Treatment for Chemists and Physicists (North-Holland, Amsterdam, **1967**).

Gunton, J. D.; San, Miguel M. and Sahni, P. S., in *Phase Transitions and Critical Phenomena*, edited by Domb C. and Lebowitz J., **Vol.VIII** (Academic, New York, **1983**).

H

Haddrell, A. E. and Agnes, G. R., *Anal. Chem.*, **76**, 53, **2004**.

Halling, P. J., *Biotechnol. Tech.* **6**, 271; P.J. Halling Private Communication, **1992**.

Hamza, M. A.; Berge, B.; Mikosch, W. and Rühl E., *Phys. Chem. Chem. Phys.*, **6**, 3484, **2004**.

Hamza, M. A., *Laboratory study on the physical properties of sea salt aerosol particles and model systems* (Ph. D thesis), **2004**.

Handy, N. C., in *European summerschool in quantum chemistry*, edited by Roos B. O. and Widmark P.O., **Vol.II**, Chap. X, pp. 505 (Lund University, Lund, **2000**).

Hartree, D. R., *Proc. Cam. Phil. Soc.* **24**, 89, **1928**.

Hassan, S. A., *J. Chem. Phys.*, **134**, 114508, **2011**.

Hawlicka, E. and Swiatla-Wojcik, *J. Chem. Phys.*, **119**, 2206, **2003**.

Heald, S.M. and Stern, E.A., *Phys. Rev. B*. **17**, 4069, **1978**.

Heffels, C.; Heizmann, D.; Hirleman, E. D. and Scarlett, B., *Appl.Opt.*, **34**, 6552, **1995**.

Hermann, K.; Pettersson, L. G. M.; Casida, M. E.; Daul, C.; Goursot, A.; Koester, A.; Proynov, E.; St-Amant, A.; Salahub, D. R.; Contributors: Carravetta, V.; Duarte, A.; Godbout, N.; Guan, J.; Jamorski, C.; Leboeuf, M.; Malkin, V.; Malkina, O.; Nyberg, M.; Pedocchi, L.; Sim, F.; Triguero, L. and Vela, A., **STOBE-DEMON** version 1.0 (Stockholm-Berlin-Montreal, **2002**).

Hess, B.; Kutzner, C.; D. van der Spoel, and Lindahl, E., *J. Chem. Theory Comput.*, **4**, 435, **2008**.

Hetényi, B.; Angelis, F. D.; Giannozzi, P. and Car, R., *J. Chem. Phys.*, **120**, 8632, **2004**.

Himo, F. and Siegbahn, P. E. M., *Chem. Rev.* **103**, 2421, **2003**.

Hitchcock, A. P.; Pocock, M., and Brion, C. E., *Chem. Phys. Lett.* **49**, 125, **1977**.

Hohenberg, P. and Kohn, W., *Phys. Rev. B*, **136**, 864, **1964**.

Horn, D. and Rieger, J., *Angew. Chem. Int. Ed.* **40**, 4330, **2001**.

Horst, R. and Sauerborn, M., *Informationsbroschüre der BESSY GmbH*, Druckhaus Panzig, Greifswald, **2004**.

Huang, F.; Zhang, H. and Banfield, J. F., *J. Phys. Chem. B* **107**, 10470, **2003**.

Hubbell, J. H. and Seltzer, S. M., *"Tables of X-Ray Mass Attenuation Coefficients and Mass Energy-Absorption Coefficients"*. National Institute of Standards and Technology (NIST). Retrieved September **2007**.

Hughes, C. E.; Hamad, S.; Harris, K. D. M.; Catlow, R. A. and Griffiths, P. C., *Faraday Discuss.* **136**, 71, **2007**.

Huthwelker, T.; Zelenay, V.; Birrer, M.; Krepelova, A.; Raabe, J.; Tzvetkov, G.; Vernooij, M. G. C. and Ammann, M., *Rev. Sci. Instrum.*, **81**, 113706, **2010**.

Hutter, J., CPMD V3.3 Copyright IBM Corp 1990-2001, Copyright MPI für Festkörperforschung Stuttgart 1997-2001 (**2001**).

Hutter, J.; Luthi, H. P., and Parrinello, M., *Comput. Mat. Sci.*, **2**, 244, **1994**.

I

Iavarone, A. T. and Williams, E. R., *J. Am. Chem. Soc.*, **125**, 2319, **2003**.

IUPAC, *Compendium of Chemical Terminology*, 2nd ed. (the "Gold Book") (**1997**).
Online corrected version: "Auger electron" (**2006**).

Izmailov, A. F.; Myerson, A. S. and Han-Soo, Na, *Physical Review E*, **52**, 3923, **1995**.

J

Jiang, H. and Liu, X. Y., *J. Biol. Chem.*, **279**, 41286, **2004**.

Joly, Y., *Phys. Rev. B*, **63**, 125120-1, **2001**.

Jorgensen, W. L.; Chandrasekhar, J.; Madura, J. D.; Impey, R. W. and Klein, M. L., *J. Chem. Phys.*, **79**, 926, **1983**.

Jorgensen, W. L.; Maxwell, D. S. and Tirado-Rives, J., *J. Am. Chem. Soc.*, **118**, 11225, **1996**.

Jorissen, K. and Rehr, J. J., *PHYSICAL REVIEW B*, **81**, 245124, **2010**.

K

Kaminski, G. A.; Friesner, R. A.; Tirado-Rives, J. and Jorgensen, W. L., *J. Phys. Chem. B* **105**, 6474, **2001**.

Kashchiev, D., *Nucleation: Basic Theory with Applications*, Butterworth-Heinemann, Oxford, **2000**.

Khamskii, E. V., *Crystalization from Solution* (Consultants Bureau, New York, **1969**).

Kimball, G. E. and Shortley, G. H., *Phys. Rev.*, **45**, 815, **1934**.

Kirmaci, I. and Ward, G., *Appl. Opt.*, **18**, 3329, **1979**.

Kirschhock, C.E.A.; Ravishankar, R.; van Looveren, L.; Jacobs, P.A. and Martens, J. A., *J. Phys. Chem. B* **103**, 4972, **1999**.

Kohn, W. and Sham, L. J., *Phys. Rev. A*, **140**, 1133, **1965**.

Kozlovskii, M. I., *Kristallografiya*, **7**, 157, **1962**.

Krämer, B.; Schwell, M.; Hübner, O.; Vortisch, H.; Rühl, E.; Baumgärtel, H.; Wöste, L and Leisner, T., *J. Chem. Phys.*, **111**, 6521, **1999**.

Kulkarni, A. M. and Zukoski, C. F., *Langmuir*, **18**, 3090, **2002**.

L

Laaksonen, A.; Talanquer, V. and Oxtoby, D. W., *Annu. Rev. Phys. Chem.* **46**, 489, **1995**.

Landau, L. D. and Lifshitz, E. M., *Statistical Physics*, **Vol. 5**, (Pergamon, London, **1986**).

Larson, M. A. and Garside, J., *J. Crystal Growth*, **76**, 88, **1986**.

Lee, C.; Yang, W. and Parr, R. G., *Phys. Rev.*, **B 37**, 785, **1988**.

Lennard-Jones, J. E., *Proc. R. Soc. Lond. A* **106** (738), 463, **1924**.

- Lippmann, G., *Ann. Phys.*, **225**, 546, **1873**.
- Liu, X. Y. and Du, N., *J. Biol. Chem.*, **279**, 6124, **2004**.
- Lo, P. Y., *PhD Dissertation*, Polytechnic University, Brooklyn, NY, **1989**.
- Lorena, Miñambres; Mar á, N. Sánchez; Fernando, Castaño; and Francisco, J. Basterretxea, *J. Phys. Chem. A*, **112**, 6601, **2008**.

M

- Maksimov, I. L., *Crystallography Reports*, **47**, Suppl. 1. S 105. **2002**.
- Marcus, Y., *Chem. Rev.*, **109**, 1346, **2009**.
- Martin, S. T., *Chem. Rev.* **100**, 3403, **2000**.
- Matsumoto, M., *Nature*, **416**, 409, **2002**.
- McDonald, J. E., *Am. J. Phys.*, **30**, 870, **1962**.
- McDonald, J. E., *Am. J. Phys.*, **31**, 31, **1963**.
- Metiu, H.; Kitahara, K. and Ross, J., in *Studies in Statistical Mechanics*, edited by Montroll E. W. and Lebowitz J. L., Vol. **VII**, (North-Holland, Amsterdam, **1979**).
- Micheletto, R.; Matsur, J.; Oyama, M.; El-Hami, K.; Matsushige, K. and Kawakami, Y., *Appl. Surf. Sci.*, **242**, 129, **2005**.
- Mie, G., *Beiträge zur Optik trüber Medien, speziell kolloidaler Metallösungen*, Leipzig, *Ann. Phys.*, **330**, 377, **1908**.
- Milman, V.; Refson, K.; Clark, S. J.; Pickard, C. J.; Yates, J. R.; Gao, S.-P.; Hasnip, P. J.; Probert, M. J.; Perlov, A. and Segall, M. D., *J. Mol. Struct. THEOCHEM*, **22**, 954, **2010**.
- Miyata, K. and Kanno, H., *J. Mol Liq*, **119**, 189, **2005**.
- Monkhorst, H. J. and Pack, J. D., *Phys. Rev. B*, **13**, 5188, **1976**.
- Motegi, H.; Emoto, T.; Ozaki, T. and Nakamura, E., *Jpn. J. Appl. Phys.*, **17**, 717, **1978**.
- Mullin, J. W. and Leci, C. L., *Phil. Mag.* **19**, 1075, **1969**.
- Mund, C. and Zellner, R., *ChemPhysChem*, **4**, 630, **2003**.
- Myerson, A. S. and Izmailov, A. F., in *Handbook of Crystal Growth*, edited by Hurlle D. T. J., Vol. 1a (Elsevier, Amsterdam, **1993**).

Myland, J. C. and Oldham, K. B., *J. Electroanal. Chem.*, **522**, 115, **2002**.

N

Na, H.-S.; Arnold, S. and Myerson, A. S., *J. Cryst. Growth*, **139**, 104, **1994**.

Navrotsky, A., *Proc. Natl. Acad. Sci. U.S.A.* **101**, 12096, **2004**.

Niederberger, M. and Colfen, H., *Phys. Chem. Chem. Phys.* **8**, 3271, **2006**.

Nilsson, A. and Martensson, N., *Physica B*, **208-209**, 19, **1995**.

Nilsson, A. and Pettersson, L. G. M., *Surf. Sci. Reports.*, **55**, 49, **2004**.

Nyberg, M.; Luo, Y.; Triguero, L.; Pettersson, L. G. M. and Agren, H., *Phys. Rev. B*, **60**, 7956, **1999**.

P

Paul, W. and Reinhard, H. P., *Z. Phys.*, **152**, 143, **1958**.

Perdew, J. P. and Wang, Y., *Phys. Rev. B*, **33**, 8800, **1986**.

Perdew, J. P.; Burke, K. and Ernzerhoff, M., *Phys. Rev. Lett.* **77**, 3865, **1996**.

Perdew, J. P.; Burke, K. and Ernzerhoff, M., *Phys. Rev. Lett.* **78**, 1396, **1997**.

Piana, S.; Reyhani, M. and Gale, J. D., *Nature*, **438**, 70, **2005**.

Piancastelli, M. N., *J. Electron Spectrosc. Relat. Phenom.*, **100**, 167, **1999**.

Pickard, C. J. and Payne, M. C., *Electron Microsc. Anal.* **153**, 179, **1997**.

Pickard, C. J., *Ph.D. Thesis*, University of Cambridge, **1997**.

Pillai, K. M.; Vaidyan, V. K. and Ittyachan, M. A., *Cryst. Res. Technol.*, **16**, K-82, **1981**.

Purcell, E. M. and Pennypacker, C. R., *Astrophys. J.* **186**, 705, **1973**.

R

Radha, A. V.; Forbes, Tori Z.; Killian, Christopher E.; Gilbert, P. U. P. A. and Navrotsky, Alexandra, *PNAS*, **107**, 16438, **2010**.

- Rayleigh, L., *Philos. Mag.*, **14**, 184, **1882**.
- Rez, P.; Alvarez, J. R. and Pickard, C. J., *Ultramicroscopy*, **78**, 175, **1999**.
- Rigby, M., *Nature (London)*, **319**, 820, **1986**.
- Ruckenstein, E. and Djikaev, Y. S., *Adv. Colloid Interface Sci.*, **118**, 51, **2005**.
- Rusli, I. T.; Schrader, G. L. and Larson, M. A., *J. Cryst. Growth*, **97**, 345, **1989**.

S

- Saban, K. V. and Varghese, G., *Indian J. Pure Ap. Phy.*, **40**, 552, **2002**.
- Saban, K. V., Jini T. and Varghese, G., *Cryst. Res. Technol.*, **40**, 748, **2005**.
- Saloman, E. B. and Hubbell, J. H., *Atomic Data and Nuclear Data Tables*, **38**, 1, **1988**.
- Sangster, M. J. L. and Dixon, M., *Ado. Phys.*, **25**, 247, **1976**.
- Schuth, F.; Bussian, P.; Agren, P.; Schunk, S. and Linden, M., *Solid State Sci.* **3**, 801, **2001**.
- Schwarz, W. H. E., *Chem. Phys.*, **11**, 217, **1975**.
- Seabourne, C. R.; Scott, A. J. and Brydson, R., *EELS modeling using a pseudopotential DFT code*, in: EMC 2008 14th European Microscopy Congress 1-5 September 2008, Aachen, Germany, **2008**, pp. 437-438.
- Segelstein, D., The Complex Refractive Index of Water, M.S. Thesis, University of Missouri, Kansas City. <http://www.philiplaven.com/Segelstein.txt>, (**1981**).
- Siegbahn, P. E. M., *Quar. Rev. Biophys.* **36**, 91, **2003**.
- Seinfeld, J. H. and Pandis, S. N., *Atmospheric Chemistry and Physics: From Air Pollution to Climate*, Wiley, New York, **1988**.
- Seinfeld, J. H., *Atmospheric Chemistry and Physics of Air Pollution*, Wiley, New York, **1986**.
- Shubnikov, A. V. and Parvov, V. F., *Kristallografiya*, **6**, 443, **1961**.
- Singh, K.; Kaur, G; Kumar, V.; Dhami, A. K. and Lark, B. S., *Radiation Physics and Chemistry*, **53**, 123, **1998**.
- Singham, S. B. and Bohren, C. F., *Opt. Lett.* **12**, 10, **1987**.

- Singham, S. B. and Salzman, G. C., *J. Chem. Phys.* **84**, 2658, **1986**.
- Skripov, V. P., *Metastable liquids*, John Wiley & Sons, New York, **1974**.
- Springer, G. S., *Advances in Heat Transfer*, Academic Press, New York, pp. 281, **1978**.
- Stavitski, Eli 1; Frank, M.F.deGroot; Stavitski, E., de Groot, F.M.F., The CTM4XAS program for EELS and XAS spectral shape analysis of transition metal L edges. *Micron* (**2010**), doi:10.1016/j.micron.2010.06.005
- Steiner, B.; Berge, B.; Gausmann, R.; Rohmann, J. and Rühl, E., *Appl. Opt.*, **38**, 1523, **1999**.
- Stöhr, J., *NEXAFS spectroscopy* (Spring-Verlag, Berlin, **1992**)
- Stöhr, J.; Sette, F. and Johnson, A. L., *Phys. Rev. Lett.*, **53**, 1684, **1984**.
- Sudholz, K., *Examensarbeiten: Aufbau eines Experimentes zur Untersuchung von levitierten Seesalz-Modellaerosolen unter troposphärischen Bedingungen*, University Osnabrück, Osnabrück, **1999**.

T

- Tabazadeh, A.; Djikaev, Y. S. and Reiss, H., *Proc. Natl. Acad. Sci. U.S.A.*, **99**, 15873, **2002**.
- Taillefumier, M.; Cabaret, D.; Flank, A. M. and Mauri, F., *Phys. Rev. B* **66**, 195107, **2002**.
- Tanaka, I.; Araki, H.; Yoshiya, M.; Mizoguchi, T.; Ogasawara, K. and Adachi, H., *Phys. Rev. B* **60**, 4944, **1999**.
- Tang, I. N. and Munkelwitz, H. R., *Aerosol. Sci. Technol.*, **15**, 201, **1991**.
- Tang, I. N. and Munkelwitz, H., R., *J. Colloid Interface Sci.*, **98**, 430, **1984**.
- Tang, J. C.; Li, S. D.; Mao, X. Y. and Du, Y. W., *J. Phys. D: Appl. Phys.*, **38**, 729, **2005**.
- Thomas, H., *Proc. Cam. Phil. Soc.*, **23**, 542, **1927**.
- Triguero, L.; Pettersson, L. G. M. and Agren, H., *Phys. Rev. B*, **58**, 8097, **1998**.
- Turkmen, I. R., Ph. D. thesis, *Homogeneous Nucleation Rates of Ice in Supercooled Binary Liquid Mixtures of Water + Non-electrolytes: A Combined Theoretical and Experimental Study*, **2007**.

U

U. von Barth and Grossmann G., *Phys. Rev. B* **25**, 5150, **1982**.

Unger, C. and Klein, W., *Phys. Rev. B*, **29**, 2698, **1984**.

V

Vanderbilt, D., *Phys. Rev. B*, **41**, 7892, **1990**.

Volmer, M., *Kinetik der Phasenbildung* (Steinkopff, Dresden, **1939**).

W

Weon, B. M. and Je, J. H., *Appl. Phys. Lett.*, **93**, 244105, **2008**.

Weon, B. M.; Je, J. H.; Hwu, Y. and Margaritondo, G., *Phys. Rev. Lett.*, **100**, 217403, **2008**.

Wexler, A., in *CRC Handbook of Chemistry and Physics*, **Vol. 90**. edited by Haynes W. M. CRC/Taylor and Francis, Boca Raton, FL, **2010**.

Wheeler, A. R., *Science*, **322**, 539, **2008**.

Wilson, C. T. R. and Philos, T. R., *Soc. Lond. A*, **192**, 403, **1899**.

Wise, M. E.; Biskos, G.; Martin, S. T.; Russell, L. M. and Buseck, P. R., *Aerosol Sci. Technol.*, **39**, 849, **2005**.

Z

Zeldovich, J., *Cavitation, Zh. Eksp. Theor. Fiz.*, **12**, 525, **1942**.

Zettlemoyer, A. C., *Nucleation* (Marcel Dekker, New York, **1969**).

Zettlemoyer, A. C., *Nucleation Phenomena*, edited by Zettlemoyer A. C. (Elsevier, Amsterdam, **1977**).

Zhang, D. S.; Gonzalez-Mozuelos, Pedro; Monica, Olvera de la Cruz, *J. Phys. Chem. C*, **114**, 3754, **2010**.

Zhang, P. C.; Keleshian, A. M. and Sachs, F., *Nature (London)*, **413**, 428, **2001**.

Zhang, T. H. and Liu, X. Y., *Angew. Chem. Int. Ed.*, **48**, 1308, **2009**.

Zheng, H.; Smith, R. K.; Jun, Y.-W.; Kisielowski, C.; Dahmen, U. and Alivisatos, A. P., *Science* **324**, 1309, **2009**.

Zolc, Z. and Sönnel, O., *Krist. Tech.*, **8**, 811, **1973**.

Others:

[C1] We assumed here that a water molecule forms a hydrogen bond with a Br atom if the distance between water H and Br atoms is equal or lower than 2.8 Å.

[C2] Zhang Y. and Wassermann B., unpublished work of Physikalische und Theoretische Chemie Institut für Chemie und Biochemie, Freie Universität Berlin, **2011**.

[C3] Measured as the energy difference between the first maxima of the XANES intensity of the first derivative.

[Inte1] Official CP2K Website: <http://www.cp2k.org/>

[Inte2] <http://www.cecam.org/workshop-273.html>

[Inte3] http://en.wikipedia.org/wiki/Lennard-Jones_potential

[Inte4] www.bessy.de

[Inte5] http://henke.lbl.gov/optical_constants/filter2.html